MATERIALS CHEMISTRY
FRONTIERS

REVIEW

View Article Online
View Journal | View Issue

Cite this: *Mater. Chem. Front.*, 2026, **10**, 21

A review of perovskite/Si tandem solar cells: internal and external components toward high efficiency, long-term durability, and commercialization

Yeonji Son,†[a] Jeongin Lim,†[b] Anh Khoa Le,[a] Beom-Soo Kim,*[c] Seulki Song *[b] and Hobeom Kim *[a]

Received 27th August 2025,
Accepted 20th October 2025

DOI: 10.1039/d5qm00637f

rsc.li/frontiers-materials

The rapid evolution of photovoltaic (PV) technology has made solar modules a key solution to meet growing global energy demands. In this context, achieving higher PV efficiency and reducing energy costs have become paramount objectives. Tandem solar cells, in which perovskite subcells are integrated with silicon (Si) subcells, represent a viable solution to surpass the Shockley–Queisser (S–Q) limit that constrains the efficiency of single-junction solar cells. These tandem configurations have demonstrated remarkable efficiency, reaching up to 34.85%, and are at the forefront of current PV research. This review focuses on recent studies aimed at enhancing the efficiency, stability, and scalability of tandem solar cells, including categorizing key areas of development in tandem solar cells into internal components (*e.g.*, Si and perovskite subcells and interconnecting layers) and external components (*e.g.*, encapsulation and busbars). Additionally, we address the fabrication process and levelized cost of energy (LCOE) of perovskite/Si tandem solar cells for cost-effective mass production. Moreover, we provide an outlook on the technological advancements required for the successful commercialization of tandem solar cells.

Introduction

Photovoltaic (PV) technology stands at the forefront of addressing the increasing global energy demand. Since the first Si solar cell was reported in 1954,[1] with a power conversion efficiency (PCE) of 6.0%, significant advances in materials development, device architecture, and fabrication processes have pushed Si solar cells to efficiencies exceeding 26.0%.[2] Meanwhile, metal halide perovskites (MHPs) have emerged as highly promising materials not only for photovoltaics but also for a wide range of optoelectronic applications including light-emitting diodes, photodetectors, and lasers.[3–7] Their outstanding optoelectronic properties such as high absorption coefficients, long carrier diffusion lengths, tunable bandgaps, together with compatibility with low-temperature solution processing have enabled remarkable efficiency improvements in perovskite solar cells (PSCs). Recent progress in composition engineering, defect passivation, and interface control has further enhanced device performance and stability, underscoring the potential of MHPs as next-generation semiconductors. Consequently, PSC efficiencies have risen from 3.8% in 2009 to a certified efficiency of 26.95% today.[2,8]

Despite significant advancements in both Si and perovskite PVs, their PCEs remain inherently constrained by the Shockley–Queisser (S–Q) limit. For Si PVs where the Si has a bandgap (E_g) of 1.12 eV, the maximum achievable PCE is approximately 32%.[9,10] Similarly, PSCs face a PCE limit of around 30% using perovskite with a E_g of 1.6 eV.[11] The efficiency limit of single-junction solar cells arises from transmission of low-energy photons and thermalization of high-energy photons.

Tandem solar cells which consist of multiple cells with light absorbers having different bandgaps can overcome the S–Q limit by ensuring effective coverage across the wide solar spectrum.[12–14] Perovskite (wide E_g)/Si (narrow E_g) tandem solar cells are a notable example that recently achieved a certified PCE of 34.85% that surpasses the theoretical limit of single junction solar cells.[2] Fig. 2 shows the certified efficiency evolution of perovskite/Si tandem solar cells, highlighting continuous improvements from 2016 to 2025.[2] To realize commercialization of the perovskite/Si tandem solar cells, nevertheless, further improvement in both efficiency and stability is required. Thus, we categorize key factors into

[a] *Department of Materials Sciences and Engineering, Gwangju Institute of Science and Technology (GIST), Gwangju, 61005, Republic of Korea. E-mail: hobkim@gist.ac.kr*
[b] *Department of Chemical Engineering and Applied Chemistry, Chungnam National University (CNU), Daejeon, 34134, Republic of Korea. E-mail: sksong@cnu.ac.kr*
[c] *Advanced Materials Division, Korea Research Institute of Chemical Technology (KRICT), Daejeon 34114, Korea. E-mail: bkim@krict.re.kr*
† These authors contributed equally to this work.

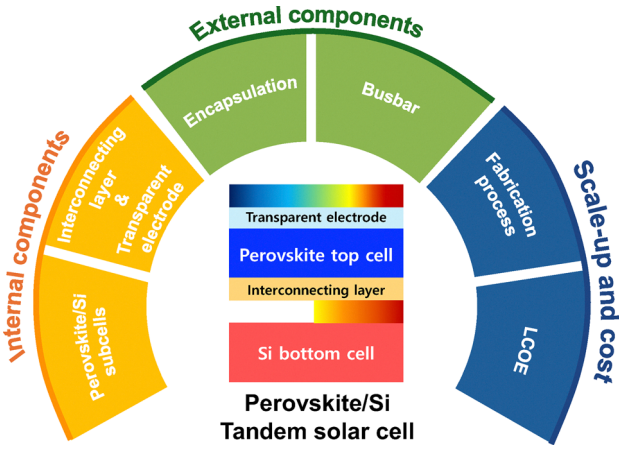

Fig. 1 Schematic overview of the review addressing internal components and external components of perovskite/Si tandem solar cells.

internal and external components, which mutually connect and contribute to the structural and functional characteristics of the cells (Fig. 1), to understand and analyze the current state of perovskite/Si tandem solar cells, gaining insights essential for their further development in the industrial scale.

Internal components of tandem solar cells refer to the elements and materials (*e.g.*, Si and perovskite subcells, and interconnecting layers) that are directly involved in the photoconversion process within the cell. On the other hand, external components act as the supportive and protective elements around the photovoltaic device (*e.g.*, encapsulation and busbars), crucial for enhancing its overall performance and lifetime.

Among the internal components, the Si bottom cell is typically configured into three types: passivated emitter and rear cell (PERC), tunnel oxide passed contact (TOPCon), and Si heterojunction (SHJ). PERC cells are the most widely adopted due to their compatibility with traditional cell designs and the efficiency boost by the addition of a rear passivation layer. TOPCon cells, regarded as the next generation of PERC technology, also integrate into the conventional cell structure while being further enhanced by a tunnel-oxide layer of SiO_2, which

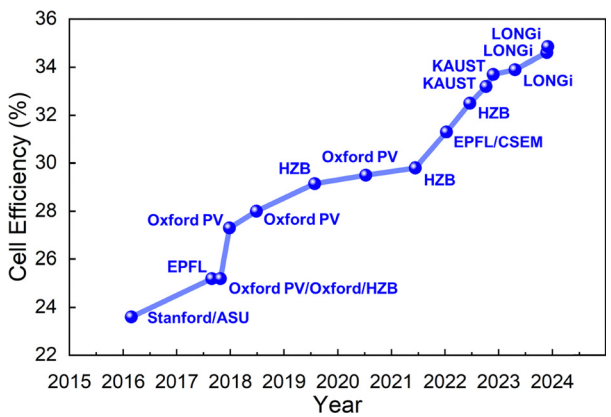

Fig. 2 Certified efficiency evolution of perovskite/Si tandem solar cells (2016–2025).[2]

improves surface passivation and facilitates selective charge transport. SHJ cells use a hydrogenated amorphous Si (a-Si:H) layer on both sides of the crystalline Si (c-Si) substrate, which provides surface passivation of the c-Si surfaces, thereby improving cell efficiency. Given the unique structures and characteristics of each Si subcell type, further evaluation of their compatibility with perovskite top cells is essential for developing optimal Si/perovskite tandem solar cells.

As a top cell in a tandem configuration, PSCs offer advantages due to their tunable E_g, which allows spectral complementarity with Si bottom cells.[15,16] However, despite these promising features, PSCs face critical challenges such as open-circuit voltage (V_{OC}) losses and poor stability, which are associated with the presence of defects and their migration.[17–19]

The interconnecting layer (ICL) is also an essential component for establishing perovskite/Si tandem solar cells as it connects the individual subcells, enabling their operation as a tandem unit. An ideal ICL should possess optimal electrical properties to minimize charge carrier losses between the subcells and maintain high optical transparency, particularly in the near-infrared (NIR) region, to reduce light absorption losses in the narrow bandgap subcell.[20]

For the external components, encapsulation serves as a protective barrier against environmental factors such as moisture, thermal stress and dust, extending durability and operational lifetime of the cells. In addition, busbars play a critical role in ensuring efficient current collection across the large area of the cells.

Lastly, we address the fabrication processes of perovskite/Si tandem solar cells and examine their levelized cost of electricity (LCOE) to assess economic viability—a critical aspect for market adoption.[21] Here, we compare reported tandem LCOE values of perovskite/Si tandem solar cells with those of conventional c-Si PV technologies. By covering these topics, our review provides a comprehensive analysis of the current state of perovskite/Si tandem solar cells, suggesting pathways to further their enhancement and commercialization.

Part I: internal components of perovskite/Si tandem solar cells

Si bottom cells for perovskite/Si tandem solar cells

Over the past 30 years, Si solar cells have made significant progress, largely driven by advancements in the device structure (Fig. 3(a)).[22] A key breakthrough has been the development and optimization of passivating contacts at the metal contact interface, which greatly enhances the PCEs by reducing surface and interfacial recombination losses as well as optical losses (Fig. 3(c)–(e)).[23] In perovskite/Si tandem solar cells where the top perovskite and bottom Si cells are integrated, optimizing the Si bottom cell design is crucial. This includes considerations such as cell structure, surface morphology or texture, and fabrication process.

Below, we introduce the most common types of Si solar cells used in perovskite/Si tandem solar cells —PERC, TOPCon, and

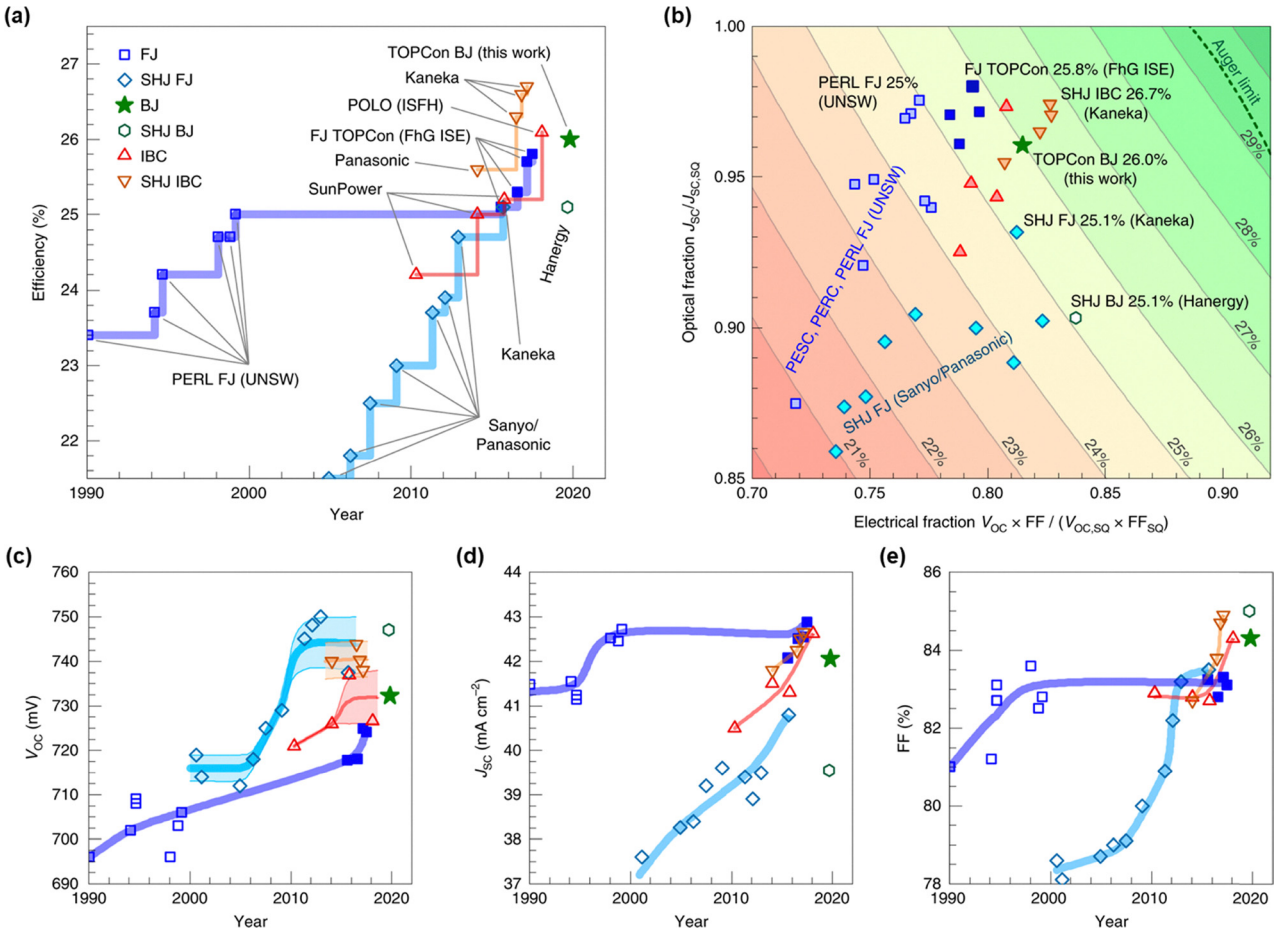

Fig. 3 (a) Efficiency advancement of Si solar cells through cell structure development. (b) Electrical and optical fraction of the various solar cells, parameter change (c) V_{OC}, (d) J_{SC} and (e) FF of various types of Si solar cells for the past 30 years. FJ: front junction, BJ: back junction, IBC: interdigitated back contact, POLO: poly-Si on oxide. Reproduced with permission.[23] Copyright 2021, Springer Nature.

SHJ—and address potential challenges associated with their integration with perovskite top cells.

PERC (passivated emitter rear contact) cells

PERC cells typically employ p-type Si (p-Si) as an absorber layer. The front side consists of an n^+ emitter, a SiN_x:H layer, and a metal grid (Fig. 4(a)). The n^+ emitter is a doped Si layer that collects charges, while the SiN_x layer reduces light reflection. On the rear side, PERC cells have a local back rear field (BSF), a rear passivation layer, and another metal grid.[24] The AlO_x/SiN_x stack is a key component of the rear passivation layer to reduce dangling bonds, electrical losses, and carrier recombination, which improves V_{OC}.[25,26] A high negative fixed charge density of the AlO_x layer ($\sim 10^{13}$ cm^{-2}) generates an electric field that repels negative charge carriers, reducing recombination at the

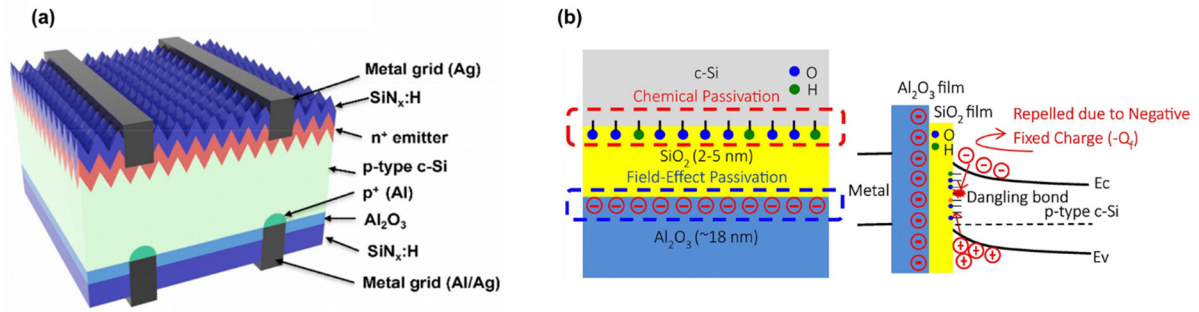

Fig. 4 (a) Structure of PERC cell. Reproduced with permission.[25] Copyright 2023, Elsevier Inc., (b) schematic energy band diagram of AlO_x/SiN_x interface. Reproduced with permission.[30] Copyright 2019, Elsevier B.V.

p-Si surface.[27,28] On the other hand, SiN_x helps terminate dangling bonds, providing chemical passivation and reducing surface recombination velocity as shown in Fig. 4(b).[29,30]

TOPCon (tunnel oxide passivated contact) cell

A standard TOPCon cell uses n-type Si (n-Si) as an absorber. The front side consists of a doped p-Si layer, which serves as an emitter, along with a SiN_x layer, and front metal contact (Fig. 5(a) and (b)). On the rear side, an ultrathin tunnel oxide layer, typically made of SiO_2, is paired with a doped n-Si rear contact layer and back metal contact. The SiO_2 layer facilitates the quantum tunneling of electrons while blocking holes, thereby providing surface passivation and enhancing carrier selectivity.[31–33] The doped p-Si layer exhibits high charge transport properties, facilitating efficient carrier collection.[34,35] This combination of SiO_2 and p-Si stack mitigates the dangling bonds, suppresses metal contact recombination, promotes charge transport, and increases V_{OC}.[35]

To achieve a high-performing TOPCon cell, controlling the thickness of the tunnel oxide layer is important.[34] For instance, an ultrathin SiO_2 layer allows for high tunneling probability for charge carriers, but pinholes can easily form during fabrication with heat treatment. While the formation of the pinholes may enable efficient charge transport leading to an increase in FF, excessive pinholes can compromise the passivation effect of the SiO_2 layer, creating pathways for leakage currents and increasing recombination at the interface.[34] Conversely, a thicker SiO_2 layer limits the transport channels for charge carriers, reducing tunneling efficiency because the probability of quantum tunneling decreases exponentially with increasing thickness.[37] Therefore, achieving optimal TOPCon cell performance requires precise control of both thickness and pinhole density of the SiO_2 layer.

In addition to advancements in rear passivation, improvements to the absorber have also contributed to the development of TOPCon solar cells.[35,38] To date, most research has focused on n-type c-Si wafers, while p-type c-Si wafers have been less explored due to their lower bulk carrier lifetime—primarily caused by boron–oxygen complex formation—and their inferior interface passivation, which stems from greater sensitivity to surface defect states.[39] However, from a mass production perspective, p-type c-Si wafers may be more suitable for TOPCon solar cells, as well-established fabrication processes for p-type wafers align with PERC production lines, potentially reducing production costs.[40] This compatibility may enable a cost-effective transition from PERC to TOPCon technology with minimal modifications, leveraging the current infrastructure and reducing the need for additional investment.

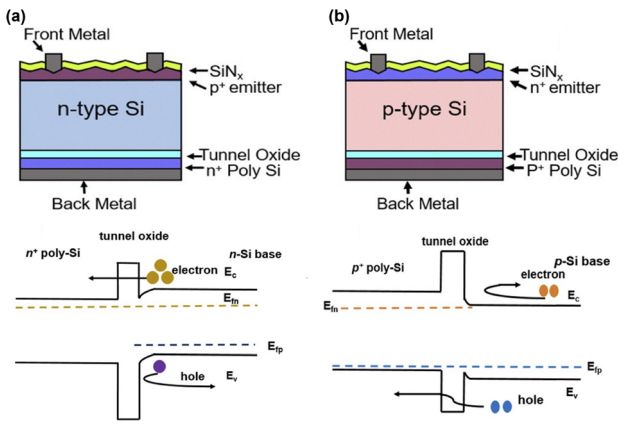

Fig. 5 (a) Structure of n-type TOPCon cell and band diagram, (b) structure of p-type TOPCon cell and band diagram. Reproduced with permission.[36] Copyright 2024, The Royal Society of Chemistry.

SHJ (Si heterojunction) cells

The structure of SHJ cells is symmetric with a c-Si layer as an absorber, positioned between intrinsic hydrogenated amorphous Si (a-Si:H(i))/doped a-Si:H(n or p) layers/transparent conducting oxide (TCO) electrodes (Fig. 6(a)).[36] The intrinsic a-Si:H layers serve as a passivation layer on c-Si surfaces while the doped a-Si:H layers form p-type or n-type regions, creating a surface potential that promotes charge separation, injection, and collection. The TCO layers, typically deposited *via* sputtering, enhance lateral charge transport and reduce parasitic absorption by a-Si:H layers, especially in the NIR region.[41] Additionally, the TCO layer induces band bending at the a-Si:H/c-Si interface, generating an electric field at the junction. This field enhances carrier selectivity by reducing electron–hole recombination and facilitates efficient extraction of photogenerated carriers.[42] However, integrating a-Si:H and TCO into the cell reduce light absorption in the range of 300–400 nm and at wavelengths beyond 750 nm. Reducing the thickness of the TCO layer can enhance the passing of more light, minimizing parasitic absorption.

Texturing Si bottom cells for perovskite/Si tandem solar cells

Textured Si bottom cells with micro-sized pyramids improve photon absorption by increasing light trapping and reducing reflection.[44–46] The surface geometry scatters incident light efficiently, inducing multiple internal reflections that extend the optical path length within the absorber layer. This effect is particularly beneficial in the NIR region where absorption of Si is inherently weaker. The most common texturing method involves anisotropic etching with alkaline solutions such as KOH, NaOH, or TMAH, which selectively etch the Si surface

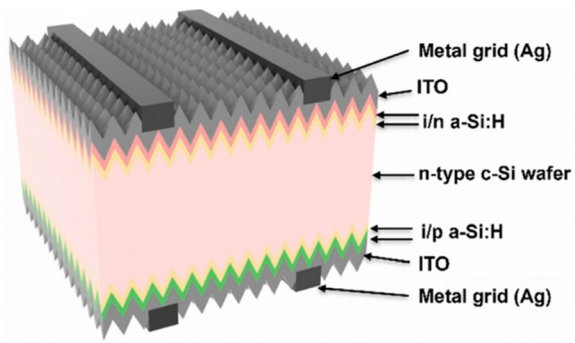

Fig. 6 (a) Structure of SHJ cell. Reproduced with permission[43] Copyright 2023, Elsevier Inc.

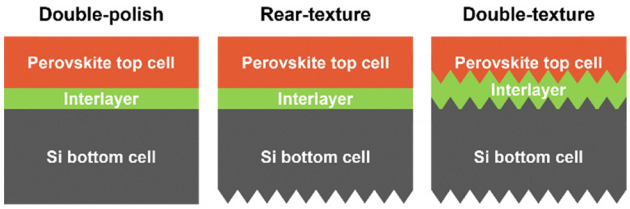

Fig. 7 Types of texturing for Si bottom cells in perovskite/Si tandem solar cells.

along its crystallographic planes to form well-defined pyramid arrays.[47,48]

In perovskite/Si tandem solar cells, the textured structures are typically classified as double-polish, rear-texture, or double-texture (Fig. 7). The double-polish and rear-texture structures, characterized by a flat top surface of Si were initially developed to simplify thin-film deposition including interlayers and perovskites by providing smoother surfaces for uniform coverage. However, these configurations often increase optical losses due to higher surface reflection and reduced light trapping, resulting in lower J_{SC} values. In contrast, double-textured structures enhance light absorption by light scattering and trapping within the device and have become the standard for high-performance solar cells. Kanda *et al.* investigated the effect of Si surface texturing on the performance of perovskite/Si tandem cells by comparing planar (polished) and textured Si surfaces on the top side (Fig. 8(a)).[49] Their results showed that texturing the Si top surface significantly reduced reflectance, which increased light absorption and contributed to an improvement in the current density from 13.7 mA cm^{-2} for planar surfaces to 14.8 mA cm^{-2} for textured surfaces (Fig. 8(b) and (c)). Achieving a uniform coverage of the perovskite layer on textured Si requires the deposition of a sufficiently thick layer, particularly to cover pyramidal tips. Solution-based methods, such as spin coating and blade coating, often involve challenges in achieving uniformity due to the micro-pyramidal surface features.[50,51] In contrast, vacuum deposition techniques offer a viable alternative by enabling more uniform film formation on textured surfaces.[52] However, vapor deposition methods have limitations, including weaker adhesion to textured substrates, which can induce mechanical stress and the formation of defects in the perovskite layer. Therefore, hybrid approaches that combine the scalability of solution-based methods with the precision of vacuum processes are needed to optimize perovskite deposition on textured Si.

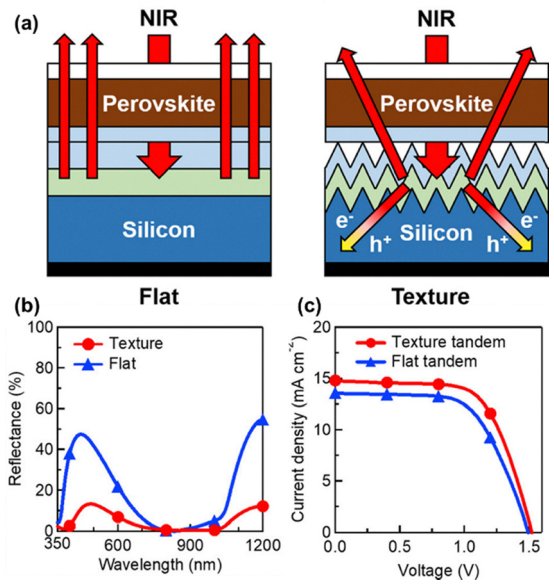

Fig. 8 (a) Structure of perovskite/polished Si (left) and perovskite/textured Si tandem solar cell (right). (b) Reflectance comparison of planner and textured Si solar cells. (c) *I*–*V* curves of perovskite/planner and textured Si tandem solar cells. Reproduced with permission.[45] Copyright 2018, American Chemical Society.

PERC cells in perovskite/Si tandem solar cells

PERC cells, widely adopted in commercial single-junction Si solar cells due to their low cost and manufacturing maturity, have also been considered as bottom cells in perovskite/Si tandem configurations. However, their passivation structure, typically composed of Al_2O_3/SiN_x presents challenges for electrical integration. While these layers provide effective surface passivation, their insulating nature prevents the direct formation of a recombination junction between the perovskite and Si subcells. To address this limitation, Wu *et al.* introduced a thin metal stack (Cr/Pd/Ag) as an interfacial contact between the Si emitter and the ITO layer (Fig. 9(a) and (b)).[53] By locally penetrating the passivation layers, the metal stack established a low-resistance contact pathway, thereby facilitating efficient carrier transport and resulting in a PCE of 22.5%. Although the metal stack improved carrier transport, PERC cells fundamentally rely on heavy doping at the metal–Si interface to reduce contact resistance.[54,55] Thus, while effective in single-junction cells, the use of PERC cells in tandem configurations may lead to increased carrier recombination and reduced V_{OC}.

TOPCon cells in perovskite/Si tandem solar cells

With their tunnel oxide and poly-Si passivating contacts, TOPCon cells offer effective surface passivation and compatibility with existing manufacturing processes, making them suitable as bottom cells in perovskite/Si tandem configurations. However, their performance is limited by optical losses arising from the poly-Si layer, which induces parasitic absorption in the near-infrared (NIR) region primarily due to its high free carrier concentration and a refractive index ($n \approx 3.8$) significantly higher than that of c-Si ($n \approx 3.4$). The optical mismatch reduces photon transmission to the Si absorber, disrupting current matching between the subcells.[57] To mitigate this issue, Ding *et al.* replaced poly-Si with poly-SiO_x ($n \approx 3.2$), which is better matched to that of the Si bottom cell (Fig. 9(c)).[56] As a result, photon transmission to the Si bottom cell increased, yielding a PCE of 25.12% (Fig. 9(d)). In addition to the optical issue associated with the presence of poly-Si, its interface with the underlying SiO_x layer often suffers from a high defect density, particularly on textured surfaces.[58] Jiang *et al.* introduced an AlO_x:H capping layer on top of the SiO_x to reduce recombination

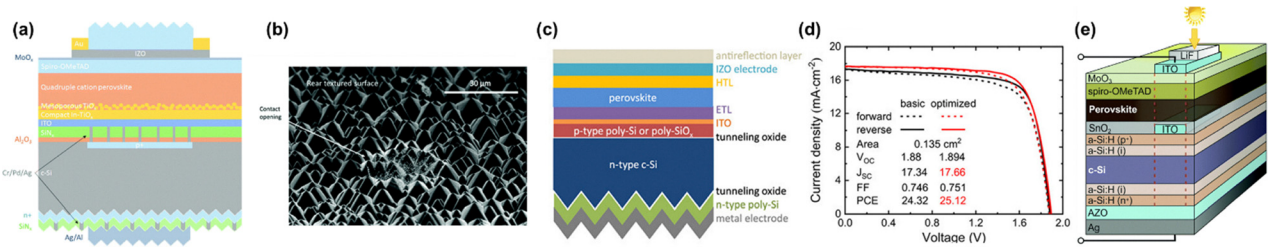

Fig. 9 (a) Structure of perovskite/PERC tandem solar cell with an intermediate contact of a Cr/Pd/Ag metal stack, and (b) SEM image of textured Si surface with local openings using the metal stack. Reproduced with permission.[53] Copyright 2017, The Royal Society of Chemistry. (c) Structure of a perovskite/TOPCon tandem solar cell incorporating a poly-SiO_x layer, and (d) *J*–*V* characteristics comparing basic (using poly-Si) and optimized (using poly-SiO_x) configurations of the perovskite/TOPCon tandem solar cell. Reproduced with permission.[56] Copyright 2024, John Wiley and Sons. (e) Structure of perovskite/SHJ tandem solar cell with SnO_2 layer deposited using ALD. Reproduced with permission.[41] Copyright 2016, The Royal Society of Chemistry.

at the SiO_x/poly-Si interface.[59] The fixed negative charge in AlO_x:H induces a field-effect that repels minority carriers from the interface, while incorporated hydrogen passivates dangling bonds and reduces the trap density. The combination of field-effect and chemical passivation effectively suppressed recombination at the SiO_x/poly-Si interface, leading to a PCE of 28.67%.

SHJ cells in perovskite/Si tandem solar cells

SHJ cells, consisting of a-Si:H(i) and a-Si:H(n or p) layers, also offer effective surface passivation, having achieved record efficiencies of 27.3% for single junction Si cells and 34.6% for perovskite/Si tandem cells.[60,61] Nevertheless, their integration into the tandem architecture is limited by the thermal instability of a-Si:H as its exposure to temperatures above 200 °C leads to hydrogen effusion, breaking Si–H bonds and degrading surface passivation.[62] This issue becomes particularly critical during the fabrication of the perovskite subcell, which involves high-temperature processes such as mesoporous TiO_2 annealing at or above 500 °C.[63] Accordingly, low-temperature processing methods have been developed to preserve the integrity of the a-Si:H passivation layers. Albrecht *et al.* employed SnO_2 which can be deposited below 120 °C by atomic layer deposition (ALD) (Fig. 9(e)). Given its high electron mobility and broad optical transparency, SnO_2 served as an efficient electron-selective contact without degrading the a-Si:H interface and thereby enabled integration of the SHJ bottom cell with a thermally compatible perovskite top cell, resulting in a PCE of 19.9%.[41,64]

Wide-bandgap perovskite top cells for perovskite/Si tandems

Wide-bandgap perovskites have gained considerable attention due to their potential in tandem solar cells, where they can be integrated with lower-bandgap Si cells. These materials typically have a bandgap greater than 1.65 eV and optimization at 1.67–1.75 eV is commonly performed for use with 1.1–1.2 eV Si bottom cells (Fig. 10(a)).[65] The bandgap can be adjusted through composition engineering of the iodide (I)/bromide (Br) ratio often combined with A-site engineering such as the incorporation of Cs^+. In this section, key challenges in the development of wide bandgap perovskites are examined, along with strategies to address them.

One of the most critical issues in wide bandgap perovskite is that V_{OC} does not increase with an increased bandgap, while current density decreases. This phenomenon can be explained by halide segregation as reported by Hoke *et al.*[68] The study found that the photoluminescence of I/Br mixed perovskite shows a red-shift with time under constant light soaking, which does not appear in pure halides (*e.g.*, $MAFACsPbI_3$ and $MAPbI_3$). Halide segregation is observed only in a mixed halide composition-based wide bandgap perovskite with V_{OC} pinning as the Br/I ratio increases (Fig. 10(b)).[66] Therefore, halide segregation was considered the major cause of V_{OC} loss in wide bandgap perovskite solar cells. However, recent studies suggest that non-radiative recombination especially at the interface of the wide bandgap perovskite could be more critical than halide segregations.[69–71] This was evidenced by the extraordinarily low initial electroluminescence external quantum efficiency (EL-EQE) of mixed halide perovskite devices (10^{-6} to 10^{-8}) prior to the halide segregation as the EL-EQE is directly related to V_{OC} as shown in eqn (1).[72] For example, in a study on a 1.77 eV perovskite, the authors found that a V_{OC} loss by trap-assisted non-radiative recombination was 385 mV, which is approximately 5 times larger than a V_{OC} loss (75 mV) by halide segregation. Additionally, the top contact of the perovskite layer, such as the electron transporting layer (ETL, *e.g.*, PCBM) is a critical factor for V_{OC} loss. The photoluminescence quantum yield (PLQY) of the isolated perovskite film is 10^{-3}, but this reduces below the detection limit with an ETL, indicating significant V_{OC} loss at the perovskite interface.

$$V_{OC} = V_{OC,rad} + \left(\frac{k_B T}{q}\right) \cdot \ln(EQE_{EL}) \quad (1)$$

The origin of initial traps that cause non-radiative recombination in wide bandgap perovskites was suggested by Huang *et al.*, in the context of the crystallization process (Fig. 10(c)).[67] According to their findings, the Br-containing precursors have lower solubility than the I-based precursors, resulting in the formation of Br-perovskite nuclei prior to I-perovskite during the spin coating process. Therefore, the I–Br mixed perovskite is not directly formed from a solution state but instead involves solid-state diffusion of I from I-based perovskite into Br-based perovskite species. This halide migration between I and Br during film formation occurs *via* a "vacancy-assisted diffusion

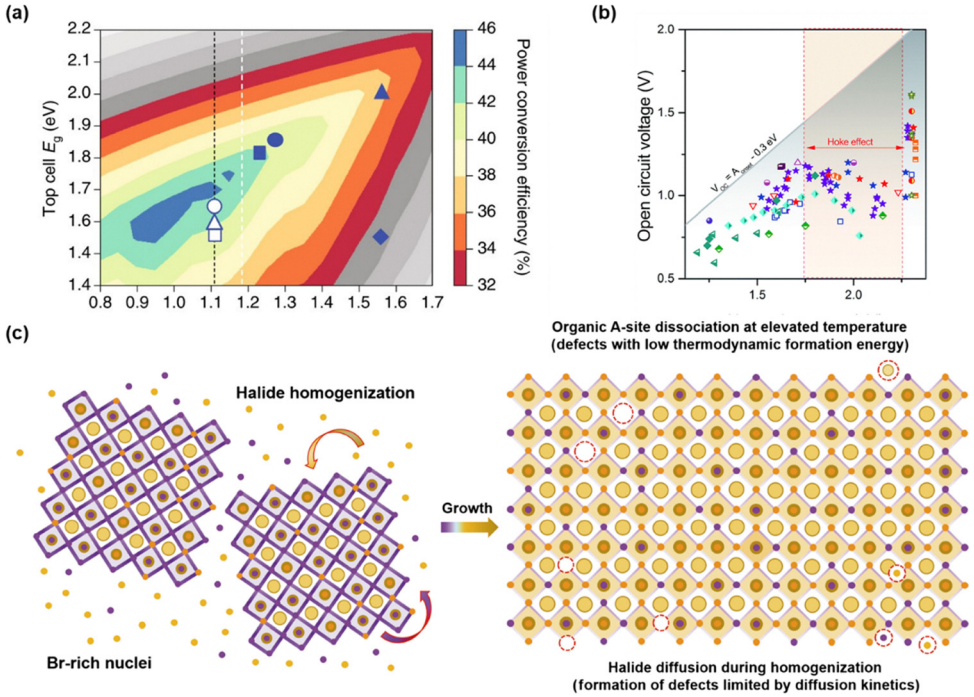

Fig. 10 (a) Theoretical power conversion efficiencies with different bandgaps for 2-terminal tandem solar cells. The black dashed line indicates the 1.12 eV bandgap of Si. Reproduced with permission.[65] Copyright 2018, Springer Nature, (b) Reported V_{OC} as function of bandgap showing onset of the Hoke effect. Reproduced with permission.[66] Copyright 2017, The Royal Society of Chemistry, (c) the defect generation model of I–Br mixed perovskite during film growth *via* halide homogenization. Reproduced with permission.[67] Copyright 2021, American Association for the Advancement of Science.

process'', forming point defects. Recent studies have shown that the positive iodide interstitial defects (I_i^+) generate deep traps in the I–Br mixed wide-bandgap perovskite.[73] This defect generation process occurs not only during the growth process, but also during halide segregation, which involves ion migration *via* solid-state diffusion. Hence, the halide segregation may accelerate the defect generation in the I–Br mixed perovskite. Moreover, this segregated film results in the energetic loss due to the different energy levels at the interface between perovskite and charge transport layers (CTLs), since the defects formed during the film growth and segregation could be particularly abundant at the interface.[73,74] In a recent study by J. Warby *et al.*, it was demonstrated that not only mixed halide, but also cations impact on interface non-radiative recombination at the perovskite interface, such as perovskite/electron transport layer (ETL) interface in a p–i–n structure.[75] Specifically, the cations were found to affect the broadening of the density of states of C_{60}, resulting in the formation of additional trap states. This finding is consistent with another important aspect of voltage loss, which is the energetic misalignment between the wide bandgap perovskite and CTLs. Typically, CTLs such as SnO_2, spiro-OMeTAD, nickel oxide (NiO_x), PTAA, and C_{60} are optimized for use with narrow or middle bandgap perovskites ($E_G \leq 1.6$ eV) and have demonstrated record high performances.[65,76] Therefore, using these same CTLs for wide bandgap perovskites could involve in energetic losses as the energy bands differ from those of lower bandgap perovskites.

In order to minimize V_{OC} loss in wide bandgap perovskite, various solutions have been extensively reported. Compositional engineering such as replacing A site and X sites with using Cs^+, K^+, Rb^+, and SCN^-,[77–80] employing alkylammonium halide additives such as phenformin hydrochloride (PhenHCl), trimethylphenylammonium tribromide ($TPABr_3$), *n*-butylammonium bromide (BABr), and acetated based molecules lead acetates ($Pb(Ac)_2$), bimolecular (co-incorporation) of PEAI/$Pb(SCN)_2$.[73,81–87] To suppress the trap formation during the film growth from rapid crystallization of Br based perovskite, alternative methods for antisolvent dripping such as the gas quenching method is also successfully reported.[88] In addition, to alleviate halide segregation, which accounts for a partial V_{OC} loss as discussed above, cation engineering using cations such as FA^+, MA^+ and Cs^+ is widely reported, and the various effects of the ions on the crystal structure and dipole effects are reported.[89,90] In all of the reported approaches, improvements in V_{OC} were shown, and it is suggested that process changes such as composition engineering, additive engineering, and solvent extraction are needed. On the other hand, this also means that a technique for universally maximizing the V_{OC} of wide bandgap perovskites has not yet been firmly established, as these are necessary to minimize V_{OC} loss.

The stability of perovskite solar cells is a crucial and frequently discussed topic in the perovskite optoelectronics community. This challenge is not limited to wide bandgap perovskites but is relevant to most optoelectronic devices based on perovskite.

One of the main concerns with wide bandgap perovskites is their integration with Si tandem solar cells. To achieve this integration, the top perovskite solar cell's lifetime must be compatible with that of the Si solar cells, which is around

20 years. If the perovskite top cell's lifetime is shorter, it could compromise the performance of the tandem cell.[91,92] The halide segregation is commonly indicated as the limiting factor for the stable perovskite.[68,93] While recent studies have reported stable perovskite solar cells containing MA^+, this compound is generally considered to be responsible for low thermal and moisture stability. Hence, despite these recent developments, the challenge of achieving stable perovskite remains a critical issue within the perovskite optoelectronics community.[94,95]

Various approaches have been employed to address the stability issues of perovskite solar cells. These include compositional engineering, which is similar to the methods used to minimize V_{OC} loss, and cation engineering that involves the incorporation of Cs^+, K^+, and organic cations.[77–79] In addition, PEA^+ and DMA^+ are examples of large organic cations that have been reported to be effective inhibitors of halide segregation (Fig. 11).[96,97] Furthermore, the use of triple-halides (I, Br, and Cl) has been suggested to suppress halide segregation. Studies have shown almost no segregation up to 100 sun intensity for 1.67 eV perovskite films when a triple-halide is used.[98]

An alternative approach to obtaining wide bandgap perovskites that are fundamentally free from the halide segregation is $CsPbI_3$, possessing bandgaps depending on the phases 1.74 eV, 1.73 eV, and 1.64 eV for γ-, α- and β-phases, respectively.[99,100] Recent studies using $CsPbI_3$ have shown that it achieves PCEs exceeding 20%, suggesting that this approach holds promise as a solution for wide bandgap perovskite solar cells free from halide segregation.[101–103] However, both the thermodynamically unstable phase and the need for further improvements in the material's stability against moisture, light, and heat pose significant challenges that still require attention and ongoing efforts for the use of $CsPbI_3$ perovskite.

Interconnecting layer (ICL) of perovskite/Si tandem solar cells

The interconnecting layer (ICL) plays a vital role in perovskite/Si tandem solar cells by establishing electrical connection between the two subcells. It should also allow efficient transmission of sub-bandgap photons to the Si bottom cell through high optical transparency to ensure efficient light use. The ICL is expected to have sufficiently high optical transparency while minimizing parasitic absorption and interfacial reflection. Electrically, it should exhibit high vertical conductivity to limit voltage and series resistance losses.

ICLs typically adopt either recombination junctions (RJs) or tunnel junctions (TJs) (Fig. 12 and Table 1). RJs, which are often based on TCO layers, offer high transparency and are relatively easy to fabricate. However, their limited conductivity can cause carrier accumulation, voltage loss, and potential shunting.

TJs, by contrast, consist of heavily doped p^{++}/n^{++} layers that form a narrow depletion region, allowing efficient quantum tunneling. While TJs exhibit superior electrical performance, they may also suffer from optical losses caused by free carrier absorption in the doped regions. Mitigating these losses requires precise control over doping concentration and interface passivation. The choice between RJs and TJs involves trade-offs in

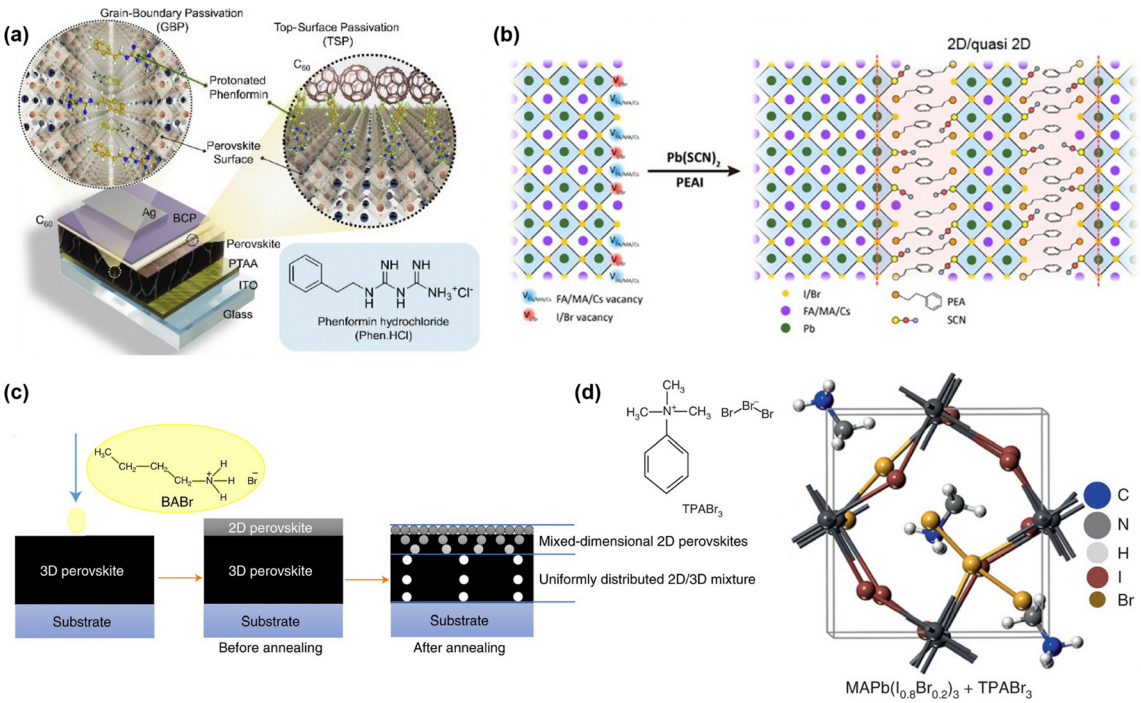

Fig. 11 Various alkylammonium halide additives strategies to reduce V_{OC} loss such as (a) phenformin hydrochloride (PhenHCl). Reproduced with permission.[73] Copyright 2021 Elsevier Inc., (b) $Pb(SCN)_2$ + PEAI. Reproduced with permission.[87] Copyright 2019, Elsevier Inc., (c) *n*-butylammonium bromide (BABr). Reproduced with permission.[78] Copyright 2021 Springer Nature, (d) trimethylphenylammonium tribromide ($TPABr_3$). Reproduced with permission.[77] Copyright 2022 Springer Nature.

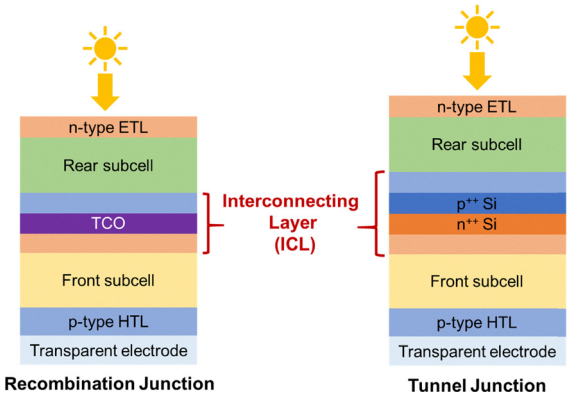

Fig. 12 Structure of perovskite/Si tandem solar cells using recombination junction and tunnel junction.

optical transmission, electrical conductivity, and fabrication complexity, making ICL optimization a key design challenge in perovskite/Si tandem solar cells.

Recombination junctions (RJs)

RJs, most commonly based on TCOs, are widely employed in perovskite/Si tandem solar cells to facilitate carrier recombination between the subcells. In addition to providing electrical connection, they are expected to minimize optical losses through high transmittance in the visible spectrum (>80%) and maintain low resistivity ($\sim 2.0 \times 10^{-4}$ Ω cm at room temperature).[104,105] Recent efforts have focused on optimizing the junction to reduce parasitic absorption and enhance recombination efficiency, both of which directly impact tandem device performance (Table 2). Among the various TCO-based materials, ITO remains the most widely adopted due to its excellent conductivity and transparency. In a pioneering work, Albrecht *et al.* utilized ITO as the RJ layer, achieving a PCE of 18.1%.[41] However, the large refractive index mismatch between ITO ($n \approx 2.0$) and c-Si ($n \approx 3.4$) led to significant interfacial reflection losses, limiting light transmission to the bottom cell.[106,107] To address this issue, Mazzarella *et al.* introduced a hydrogenated nanocrystalline SiO_x (nc-SiO_x:H) interlayer with an intermediate refractive index ($n \approx 2.5$), which improved optical matching, boosting PCE to 25.2%.[108] Another challenge in ITO-based RJs is excessive in-plane conductivity, which can cause lateral leakage and device shunting.[109,110] In terms of electrical performance, the sheet resistance of ITO layers used in RJs typically ranges from 10 to 20 Ω sq^{-1}, which is necessary to ensure sufficient lateral conductivity for current collection in standard Si-based devices.[111] However, in tandem structures, this high lateral conductivity ($\sim 10^{-4}$ Ω cm) can promote parasitic current pathways, especially in regions of non-uniform perovskite coverage or pinholes, leading to lateral leakage currents and localized shunting.[112] Furthermore, the absence of a built-in junction field across the RJ layer necessitates high vertical conductivity to support efficient carrier recombination while minimizing voltage losses. To address these challenges, recent designs increasingly focus on decoupling vertical and lateral conduction paths, for example by incorporating low-conductivity HTLs (*e.g.*, NiO_x), which can suppress lateral leakage while maintaining sufficient vertical recombination efficiency. Xu *et al.* introduced a sputtered NiO_x layer as an HTL, which reduced lateral conductivity while improving interface passivation and energy-level alignment at the NiO_x/perovskite interface (Fig. 13(a)).[113] To further improve interfacial quality and charge extraction, a spiro-TTB buffer layer was introduced at the NiO_x/perovskite interface. The additional buffer layer promoted uniform perovskite nucleation, suppressed pinhole formation, and facilitated efficient charge extraction, collectively contributing to a PCE of 27.43%.

Recent studies have demonstrated the effectiveness of self-assembled monolayers (SAMs) as an interfacial layer in RJs for perovskite/Si tandem solar cells.[149,152] The molecular-scale thickness of SAMs ensures high optical transparency while allowing dipole-induced energy level alignment to facilitate charge extraction. In addition, SAMs contribute to reducing interfacial recombination by chemically passivating surface charge extraction. In addition, SAMs contribute to reducing interfacial recombination by chemically passivating surface defects. Al-Ashouri *et al.* employed Me-4PACz as a SAM at the RJ, achieving a PCE of 29.05% along with facilitated hole extraction indicated by reduced transient PL lifetime (~300 ns).[122] Despite these advantages, conventional SAMs such as Me-4PACz typically exhibit poor wettability and non-uniform coverage, potentially causing device shunting and reduced reproducibility. To address these challenges, Li *et al.* introduced a mixed SAM composed of Me-4PACz and MeO-PhPACz (Fig. 13(b) and (c)).[151] The mixed SAM significantly enhanced wettability due to the incorporation of MeO-PhPACz, which contains polar functional

Table 1 Comparison of recombination junction (RJ) and tunnel junction (TJ) interconnecting layers

Feature	Recombination junction (RJ)	Tunnel junction (TJ)
Definition	Interface enabling carrier recombination and electrical connection.	Quantum tunneling through highly doped junction.
Typical materials	ITO, IZO, TCO/NiO_x, TCO/SAMs.	a-Si:H(p^+/n^+), nc-Si:H, poly-Si, TiO_2/ITO.
Optical property	High transparency, depending on TCO quality.	High transparency if thin; free-carrier absorption increases with heavy doping.
Electrical property	Moderate resistance, affected by interface defects.	Very low resistance with optimized doping.
Advantages	Simple fabrication, wide material choice.	High conductivity, efficient carrier recombination, low voltage loss.
Disadvantages	Interface traps and long-term stability issues.	Doping control challenges and process complexity.

Table 2 Efficiency of perovskite/Si tandem solar cells with various RJs

Year	Perovskite composition	Perovskite bandgap (eV)	Si type	Recombination junction (RJ)	J_{SC} (mA cm^{-2})	V_{OC} (V)	FF (%)	PCE (%)	Ref.
2015	$FA_{0.83}Cs_{0.17}Pb(I_{0.83}Br_{0.17})_3$	—	SHJ	ITO/SnO_2	14.00	1.79	79.50	19.90	41
2015	$MAPbI_3$	—	SHJ	IZO/PCBM[a]/PEIE[b]	15.80	1.69	79.90	21.40	114
2016	$MAPbI_3$	—	PERC	ZTO/c-TiO_2/m-TiO_2	15.30	1.68	68.00	17.40	115
2017	$Cs_{0.17}FA_{0.83}Pb(Br_{0.17}I_{0.83})_3$	1.63	SHJ	ITO/NiO	18.10	1.65	79.00	23.60	116
2017	$Cs_{0.07}Rb_{0.03}FA_{0.765}MA_{0.135}PbI_{2.55}Br_{0.45}$	1.62	SHJ	ITO/TiO_2	17.60	1.75	73.80	22.80	53
2018	$Cs_{0.17}FA_{0.83}Pb(Br_{0.17}I_{0.83})_3$	—	PERC	ITO/NiO_x	15.30	1.43	75.00	16.20	117
2018	$FA_{0.75}Cs_{0.25}Pb(I_{0.8}Br_{0.2})_3$	1.68	SHJ	ITO/PTAA[c]	18.40	1.77	77.00	25.00	106
2019	$Cs_{0.15}(FA_{0.83}MA_{0.17})_{0.85}Pb(I_{0.7}Br_{0.3})_3$	1.70	SHJ	ITO/PTAA	16.40	1.83	74.50	22.40	118
	$Cs_{0.15}(FA_{0.83}MA_{0.17})_{0.85}Pb(I_{0.75}Br_{0.25})_3$	1.68			17.10	1.81	79.00	24.50	
	$Cs_{0.15}(FA_{0.83}MA_{0.17})_{0.85}Pb(I_{0.8}Br_{0.2})_3$	1.64			17.80	1.80	79.40	25.40	
	$Cs_{0.15}(FA_{0.83}MA_{0.17})_{0.85}Pb(I_{0.85}Br_{0.15})_3$	1.62			17.40	1.77	78.10	24.10	
2019	$FA_{0.8}MA_{0.2}PbBr_{0.6}I_{2.4}$	1.64	PERC	ITO/PTAA	16.12	1.65	79.92	21.19	119
2019	$FA_{0.75}Cs_{0.25}Pb(I_{0.8}Br_{0.2})_3$	1.70	SHJ	ITO/c-TiO_2/m-TiO_2	15.20	1.84	77.30	21.60	120
2019	$MAPbI_3$	—	SHJ	ITO/AgNW[d]/TCA[e]/ZnO/PEI[f]/PCBM	14.70	1.78	80.40	21.00	121
2020	$(FA_{0.65}MA_{0.2}Cs_{0.15})Pb(I_{0.8}Br_{0.2})_3$	1.70	SHJ	ITO/PTAA	19.20	1.76	79.20	26.70	84
2020	$CsPbBr_xCl_{3-x}$ + $Cs_mFA_nMA_{1-m-n}PbI_xBr_{3-x}$	1.67	SHJ	ITO/NiO_x/PolyTPD/PFN[g]	19.12	1.89	75.30	27.13	98
2020	$Cs_{0.05}(FA_{0.77}MA_{0.23})_{0.95}Pb(I_{0.77}Br_{0.23})$	1.68	SHJ	ITO/Me-4PACz[h]	19.26	1.90	79.52	29.05	122
2020	$FA_{0.75}Cs_{0.25}Pb(I_{0.8}Br_{0.2})_3$	1.68	SHJ	ITO/PTAA/PFN	17.70	1.77	80.30	25.10	123
2022	$Cs_{0.05}FA_{0.8}MA_{0.15}Pb(I_{0.75}Br_{0.25})_3$	—	SHJ	IZO/2PACz[i]	18.60	1.86	76.00	26.20	124
2022	$Cs_{0.05}(FA_{0.83}MA_{0.17})_{0.95}Pb(I_{0.83}Br_{0.17})_3$	1.63	TOPCon	IZO/MeO-2PACz[j]	19.40	1.80	81.64	28.49	125
2022	$Cs_{0.05}(FA_{0.74}MA_{0.26})_{0.95}Pb(I_{0.74}Br_{0.26})_3$	—	SHJ	ITO/2PACz + MeO-2PACz	19.40	1.86	79.58	28.80	126
2022	$FA_{1-x}MA_xPbI_{3-y}Br_y$	1.59	PERC	ITO/NiO_x	16.50	1.75	81.80	23.70	127
2022	$Cs_{0.22}FA_{0.78}Pb(Cl_{0.03}Br_{0.15}I_{0.85})_3$	1.68	TOPCon	ITO/NiO_x/PolyTPD[k]	19.68	1.79	78.27	27.63	128
2023	$Cs_{0.05}(FA_{0.83}MA_{0.17})_{0.95}Pb(I_{0.83}Br_{0.17})_3$	1.64	SHJ	ITO/PTAA/PFN	19.90	1.73	73.00	25.60	107
2023	MASCN:$CsPb_4I_7Br$	1.68	SHJ	ITO/NiO/2PACz + MeO-2PACz	19.80	1.85	78.90	28.90	129
2023	$Cs_{0.22}FA_{0.78}Pb(I_{0.85}Br_{0.15})_3$	1.63	TOPCon	IZO/MeO-2PACz	19.3	1.80	81.9	28.50	130
2023	$MASnI_{3-x}Br_x$	1.3–2.15	SHJ	ITO/spiro-OMeTAD[l]	16.89	2.14	84.55	30.70	131
2023	$Cs_{0.05}FA_{0.79}MA_{0.16}Pb(I_{0.75}Br_{0.25})_3$	—	PERC	ITO/2PACz	18.60	1.69	76.9	24.20	132
2023	$Cs_{0.22}FA_{0.78}Pb(I_{0.85}Br)_3$ + 5% $MAPbCl_3$	1.68	SHJ	ITO/Me-4PACz	20.24	1.98	81.18	32.50	133
2023	$Cs_{0.15}FA_{0.65}MA_{0.20}Pb(I_{0.80}Br_{0.20})_3$	1.68	TOPCon	IZO/MoO_x/sprio-OMeTAD	18.80	1.78	81.80	27.40	134
2023	$Cs_{0.15}FA_{0.65}MA_{0.20}Pb(I_{0.80}Br_{0.20})_3$	1.68	TOPCon	IZO/Me-4PACz	20.70	1.78	82.00	30.26	135
2023	$Cs_{0.05}(FA_{0.75}MA_{0.25})_{0.95}Pb(I_{0.75}Br_{0.25})_3$	1.55	SHJ	ITO/P3CT-N[m]	20.39	1.83	77.57	28.89	136
2023	$Cs_xFA_yMA_{1-(x+y)}Pb(I,Br)_3$ $(x+y \leq 1)$	1.65	SHJ	ITO/NiO_x/2PACz	19.56	1.77	79.40	27.51	137
2024	$Cs_{0.05}FA_{0.80}MA_{0.15}Pb(I_{0.75}Br_{0.25})_3$	1.67	SHJ	ITO/NiO/2PACz + MeO-2PACz	20.10	1.94	76.70	29.80	138
2024	$Cs_{0.05}(FA_{0.84}MA_{0.16})_{0.95}Pb(I_{0.75}Br_{0.25})_3$	1.67	TOPCon	ITO/NiO	19.58	1.93	81.54	30.09	139
2024	$Cs_{0.05}FA_{0.80}MA_{0.15}Pb(I_{0.8}Br_{0.2})_3$	1.55	SHJ	ITO/MeO-2PACz	20.64	1.82	75.92	28.50	140
2024	$Cs_{0.05}FA_{0.80}MA_{0.15}Pb(I_{0.75}Br_{0.25})_3$	1.68	SHJ	ITO/Me-4PACz	20.09	1.93	78.43	30.43	141
2024	$Cs_{0.05}(FA_{0.90}MA_{0.1})_{0.95}PI_{0.8}Br_{0.203}$	1.65	SHJ	ITO/Me-4PACz/SiO_2-NP[n]	19.81	1.95	79.90	30.93	142
2024	$Cs_{0.05}FA_{0.80}MA_{0.15}Pb(I_{0.755}Br_{0.255})_3$	1.68	SHJ	IZO/Me-4PACz	20.96	1.95	80.50	34.00	143
2024	$FA_{0.78}Cs_{0.22}Pb(I_{0.82}Br_{0.18})_3$ and excess 3% $MAPbCl_3$	1.65	SHJ	ITO/PolyTPD	20.40	1.96	81.00	32.50	144
2024	$FA_{0.8}MA_{0.15}Cs_{0.05}Pb(I_{0.76}Br_{0.24})_3$ and 5% excess PbX_2 (X = I, Br)	1.69	SHJ	IZO/MeO-4PACz	20.76	1.97	83.00	33.89	145
2025	$Cs_{0.05}MA_{0.15}FA_{0.8}Pb(I_{0.76}Br_{0.24})_3$	1.66	SHJ	ITO/NiO_x/Me-4PACz	20.23	1.98	80.76	30.98	146
2025	$Cs_{0.17}FA_{0.83}Pb(I_{0.80}Br_{0.20})_3$	1.67	SHJ	ITO/4-PhCz[o]	19.92	1.96	81.00	31.26	147
2025	$Cs_{0.15}FA_{0.85}Pb(I_{0.77}Br_{0.23})_3$	1.66	TOPCon	ITO/4PADCB[p]	20.00	1.88	82.60	31.10	148
2025	$Cs_{0.05}FA_{0.80}MA_{0.15}Pb(I_{0.75}Br_{0.25})_3$	1.68	SHJ	ITO/2PhPA-CzH[q]	19.92	1.91	84.51	32.19	149
2025	$Cs_{0.22}FA_{0.63}MA_{0.15})Pb(I_{0.83}Br_{0.14}Cl_{0.03}$	1.66	SHJ	IZO	20.70	1.92	80.90	32.10	150

[a] PCBM: [6,6]-phenyl-C_{61}-butyric acid methyl ester. [b] PEIE: polyethylenimine ethoxylated. [c] PTAA: poly[bis(4-phenyl)(2,4,6-trimethylphenyl)amine]. [d] AgNW: silver nanowire. [e] TCA: trichloroacetic acid. [f] PEI: polyethylenimine. [g] PFN: poly[(9,9-bis(3′-(*N*,*N*-dimethylamino)propyl)-2,7-fluorene)-*alt*-2,7-(9,9-dioctylfluorene)]. [h] Me-4PACz: [2-(9*H*-carbazol-9-yl)ethyl]phosphonic acid methyl ester. [i] 2PACz: [2-(9*H*-carbazol-9-yl)ethyl]phosphonic acid. [j] MeO-2PACz: [2-(3,6-dimethoxy-9*H*-carbazol-9-yl)ethyl]phosphonic acid. [k] PolyTPD: poly[*N*,*N*′-bis(4-butylphenyl)-*N*,*N*′-bis(phenyl)benzidine]. [l] Spiro-OMeTAD: 2,2′,7,7′-tetrakis(*N*,*N*-di-*p*-methoxyphenylamine)-9,9′-spirobifluorene. [m] P3CT-N: poly[3-(4-carboxylate butyl)thiophene-2,5-diyl] (sodium salt). [n] SiO_2-NP: silicon dioxide nanoparticle. [o] 4-PhCz: 4-phenylcarbazole. [p] 4PADCB: N_4,N_4,N_4′,N_4′-tetra([1,1′-biphenyl]-4-yl)-[1,1′-biphenyl]-4,4′-diamine. [q] 2PhPA-CzH: 2-(9*H*-carbazol-9-yl)ethyl diphenylphosphinic acid.

groups that increase the surface energy, reducing the contact angle from 97° to 76°, and enabling uniform perovskite film formation. It also increased hole conductivity from 5.89×10^{-4} mS cm^{-1} to 7.44×10^{-4} mS cm^{-1}, which can be attributed to the improved molecular packing density and optimized energy-level alignment at the interface while maintaining the high optical transparency (average transmittance >90% in the visible region). Owing to the improved coverage, device reproducibility increased to ~95% yield, significantly higher than the reproducibility (<50%) obtained with a single SAM. As a result, tandem solar cells using the mixed SAM achieved a PCE of 28.07%. While enhanced coverage improves morphological uniformity, molecular dipole engineering provides an additional pathway for optimizing interfacial energetics in SAM-based RJs. Luo *et al.* developed a series of pyridine-annulated anthracene (PyAA) SAMs with inductive substituents (PyAA, PyAA-Br, PyAA-Me, and PyAA-MeO) on ITO for perovskite/Si tandem solar cells.[153] By tuning the electron-donating or withdrawing nature

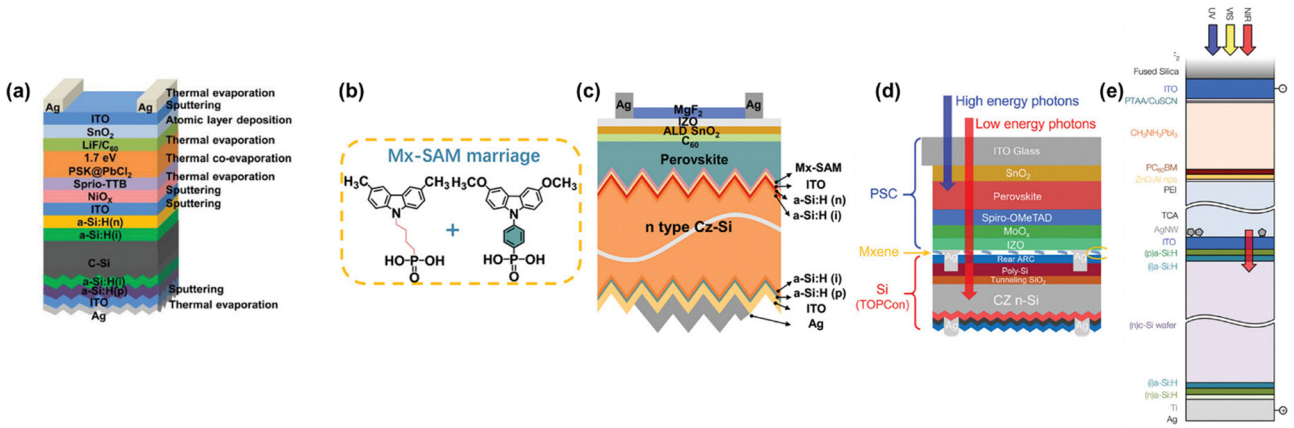

Fig. 13 (a) Structure of a perovskite/Si tandem solar cell using NiO_x interlayers. Reproduced with permission.[113] Copyright 2023, Wiley-VCH GmbH. (b) Mx-SAM configurations, combining Me-4PACz and MeO-PhPACz molecules, and (c) structure of a perovskite/Si tandem solar cell using an Mx-SAM interlayer. Reproduced with permission.[151] Copyright 2024, Wiley-VCH GmbH. (d) Structure of an RJ-incorporated MXene. Reproduced with permission.[135] Copyright 2019, Wiley-VCH GmbH. (e) Structure of perovskite/Si tandem solar cells using a D-PEDOT:PSS RJ Reproduced with permission.[121] Copyright 2019, Wiley-VCH GmbH.

of the substituents, they modulated the dipole moment of the SAMs, which in turn shifted the vacuum level at the ITO/perovskite interface, improving energy-level alignment and facilitating hole extraction while reducing recombination losses. Among the SAMs, PyAA-MeO featuring a moderately electron-donating methoxy group exhibited an optimal balance between dipole strength and molecular packing, leading to substantial increase in device efficiency with a certified PCE of 30.9%. Despite the remarkable progress achieved with conventional carbazole-based SAMs, their symmetric molecular structure still causes steric hindrance near the anchoring sites, which prevents close molecular packing, thereby limiting both interfacial uniformity and defect passivation. To overcome the structural limitation of SAMs, Jia *et al.* designed an asymmetric carbazole-based SAM in which a spacer and a phosphonic-acid anchoring group flank the phenyl ring of the carbazole core.[154] The asymmetry reduces steric hindrance and enables denser molecular packing and more uniform surface coverage on TCO substrates. Moreover, the modified configuration strengthens coordination with undercoordinated Pb^{2+} ions and induces a larger interfacial dipole, which together enhances charge extraction and suppresses non-radiative recombination. As a result, perovskite/Si tandem solar cells employing the asymmetric SAM achieved a certified PCE of 34.58%, outperforming devices using symmetric Me-4PACz (32.77%) and MeO-4PACz (33.88%).

MXenes are also promising RJ materials due to their high electrical conductivity ($\sim$15 100 S cm^{-1}), broadband optical transmittance (>90% in the visible spectrum), and tunable work functions, which enable favorable energy-level alignment at the recombination interface.[155] Han *et al.* demonstrated that incorporating MXene interlayer reduced the recombination resistance from $\sim$77.1 Ω cm^2 to $\sim$29.5 Ω cm^2 and extended the TPV carrier lifetime from $\sim$1.8 µs to $\sim$3.5 µs, indicating suppressed recombination and improved interfacial transport (Fig. 13(d)).[135] As a result, the tandem device achieved a stabilized PCE of 29.65%. However, MXenes are susceptible to ambient oxidation and hydrolysis, which can compromise long-term operational stability. Another class of candidate RJ materials is that of conductive polymers, which offer solution processability alongside desirable optical and electrical characteristics. PEDOT:PSS, with its high optical transmittance ($\sim$85–90%) and intrinsically high in-plane resistivity ($\sim 10^0$–10^{-1} Ω cm), can suppress lateral leakage currents and has thus been investigated as an RJ material.[155] Ramírez Quiroz *et al.* used a D-sorbitol-doped PEDOT:PSS (d-PEDOT:PSS) that simultaneously served as a transparent conductive adhesive (TCA) (Fig. 13(e)).[121] The layer exhibited high vertical conductivity ($\sim$1000 S cm^{-1}), enabling efficient carrier recombination while suppressing lateral leakage. Sorbitol-induced polymer ordering also enhanced interfacial adhesion, improving mechanical stability. The resulting tandem solar cells achieved a PCE of 21.0%. However, the hygroscopic and acidic nature of PEDOT:PSS raises concerns over long-term stability, necessitating additional encapsulation or material modification for practical use.

Tunnel junction (TJ)

Despite substantial advances in RJ design, the use of TCOs often results in optical reflection losses and lateral leakage currents, which limit tandem performance. As an alternative, tunnel junctions (TJs) offer a fundamentally different approach, enabling efficient carrier recombination without relying on TCOs. A typical TJ consists of heavily doped n^{++} and p^{++} layers, with carrier concentrations typically approaching or exceeding 10^{19} to 10^{20} cm^{-3}. The high doping level significantly narrows he depletion region to a few nanometers, enabling quantum-mechanical tunneling of carriers across the junction.[156] Under forward bias, the energy alignment between filled states in the n^{++} layer and empty states in the p^{++} layer enables interband tunneling, either directly or *via* intermediate defect states.

The depletion width W, which critically influences tunneling probability, is given by eqn (2).

$$W = \sqrt{\frac{2\varepsilon(\varphi_0 - V)}{q}\frac{N_A + N_D}{N_A N_D}} \quad (2)$$

where ε is the dielectric permittivity, q is the elementary charge, N_A and N_D are the acceptor and donor doping concentrations, respectively, ϕ_0 is the built-in potential, and V is the applied voltage. As the depletion width W decreases with increasing doping concentration and forward bias, tunneling efficiency is enhanced by enabling carriers to tunnel across the junction. However, excessive doping may increase free carrier absorption and induce defect states that lead to trap-assisted non-radiative recombination. To mitigate the trade-offs associated with excessive doping, precise doping control and effective interface passivation are required to preserve electrical conductivity without incurring optical or recombination-related losses. Mailoa *et al.* implemented highly doped n^{++} a-Si:H deposited *via* plasma-enhanced chemical vapor deposition (PECVD) to demonstrate TJ integration in perovskite/Si tandem solar cells (Fig. 14(a) and (b)).[157] The highly doped amorphous Si layer resulted in a depletion width narrow enough to allow carrier tunneling, achieving a PCE of 13.7%. The TJ structure exhibited high optical transparency, exceeding 90% in the 700–1200 nm range, thereby facilitating the transmission of sub-bandgap photons to the Si bottom cell.[156] However, the electrical conductivity of a-Si:H is inherently constrained by its disordered atomic structure, and the presence of localized defect states can lead to trap-assisted recombination.[33,34]

To overcome the limited conductivity and recombination losses induced by structural disorder in amorphous Si tunnel layers, Sahli *et al.* introduced nanocrystalline Si (nc-Si:H) as the TJ material (Fig. 14(c)).[44] The partial crystallinity of nc-Si:H improved bulk conductivity and carrier mobility by reducing structural disorder. In addition, as nc-Si:H formed conformal contact with textured Si surfaces, it can minimize interfacial voids and defect generation, thereby facilitating efficient vertical charge extraction. The nc-Si:H maintained high near-infrared optical transparency with average transmittance exceeding 85% in the 700–1200 nm range which is comparable to that of a-Si:H. The combined improvements in electrical conductivity and optical transparency enabled a certified PCE of 25.2%. In addition, nc-Si:H exhibited enhanced thermal and chemical stability. STEM–EDX analysis revealed that conventional ITO/spiro-TTB/perovskite stacks underwent elemental redistribution upon annealing, whereas the nc-Si:H interface retained its compositional integrity, supporting stable long-term operation (Fig. 14(d)).

Shen *et al.* employed an interlayer-free TJ formed directly between ALD-deposited TiO_2 and p^+-Si to reduce optical losses and simplify processing.[158] At the TJ, carrier recombination occurred *via* defect-assisted tunneling through interfacial trap states, eliminating the need for heavily doped n^{++} layers. The resulting TiO_2/p^+-Si interface exhibited ohmic behavior after annealing with a low contact resistance of $\sim$30 mΩ cm^2, enabling effective tunneling across the interface. Compared to conventional TJs, due to the absence of interlayer in the TiO_2/p^+-Si structure reduced parasitic optical absorption, improving photocurrent density by $\sim$1–1.5 mA cm^{-2}. Also, the process avoided PECVD deposition, improving compatibility with perovskite fabrication steps that are sensitive to plasma or high-temperature exposure. As a result, the tandem device achieved a PCE of 24.1%, validating the effectiveness of defect-mediated tunneling as a simplified and optically transparent TJ strategy. Both conventional heavily doped TJs and alternative designs based on defect-assisted tunneling have demonstrated high vertical conductivity and optical transparency, while preserving interfacial stability and process compatibility. Nonetheless, challenges related to doping-induced absorption, interfacial trap density, and long-term stability remain critical considerations in the design of TJ-based tandem solar cells.

Transparent electrodes

Transparent conductive oxides (TCOs), such as ITO or IZO, are the most used as top electrodes in perovskite/Si tandem cells due to their excellent transparency, conductivity, stability, fast deposition rate, and scalability. In this section, we will provide a brief overview of the challenges associated with using TCOs, with a particular focus on ITO and IZO, as top electrodes in perovskite/Si tandem cells. TCO films can be deposited by various methods, including sol–gel methods, chemical vapor deposition (CVD), e-beam evaporation, and sputtering. Among these, sputtering is the predominant choice for industrial applications due to its high deposition rate and scalability.[159–163] Pulsed direct current (DC, 40–200 kHz), or radiofrequency

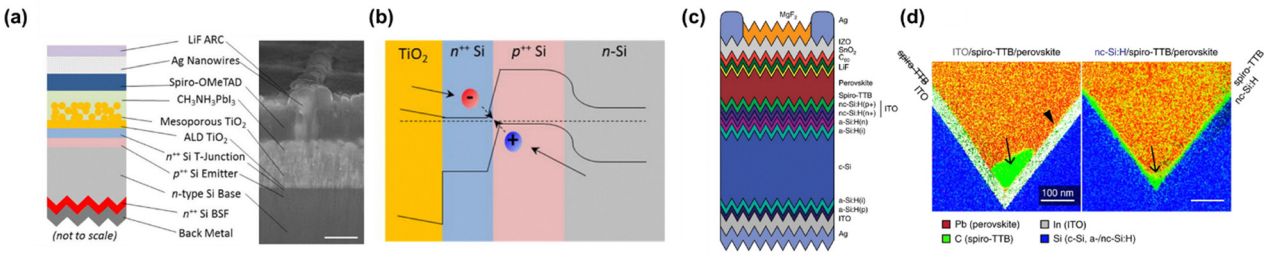

Fig. 14 (a) Structure of the tandem structure with TJ and (b) energy band diagram of tandem solar cells. Reproduced with permission.[157] Copyright 2015, AIP Publishing. (c) Structure of the perovskite/Si tandem solar cells with nc-Si:H TJ and (d) cross-sectional EDX mapping of the different layer stack. Reproduced with permission.[44] Copyright 2018, Springer Nature.

(RF, ~13 MHz) sputtering is commonly adopted for TCO deposition. Pulsed DC sputtering requires high voltage, typically a few hundred volts, to sustain the discharge through secondary electron emission, resulting in fast sputter rates and its widespread adoption in industrial fields. On the other hand, RF sputtering employs oscillating bulk plasma, resulting in a lower discharge voltage. This leads to lower-energy ion bombardment, enabling denser film growth but with reduced sputter rates.[164] Both DC and RF sputtering involve ionized inert gas, usually argon ions (Ar^+), transferring energy to the target material through collisions, which eject target atoms into the vacuum chamber and deposit them onto the substrate (Fig. 15(a)).[165] One of the common challenges associated with the sputter process is the damage inflicted on the underlying layer during the deposition. This is primarily due to the high energy of sputtered atoms, which can reach up to ~10 eV depending on the binding energy of the target material, as well as the positive ions formed in the plasma (~15 eV), neutralized ions from the target surface (~20 eV), and the luminescence of the plasma.[165] The impact of such damage on optoelectronic devices, including light-emitting diodes and solar cells, has been extensively investigated, including perovskite solar cells. The problems most reported in this regard include the formation of an energetic barrier at the TCO/underlying layer interface due to degradation of the underlying layer during the sputter process, as well as an increase in leakage current, resulting in reduced shut resistance. Kanda *et al.* reported on the effects of sputter damage on the *J–V* characteristics of perovskite solar cells, whereby the sputtered TCO on the widely used hole-transporting material (spiro-OMeTAD) led to an increase in energetic barrier and the formation of an additional diode path, resulting in an s-shaped *J–V* curve (Fig. 15(b)).[166] Similar issues were observed in the p–i–n configuration of perovskite solar cells, where the TCO was sputtered on a commonly used ETL buffer layer, bathocuproine (BCP).[167] Hence, to avoid these problem, the most widely adopted method is to introduce a buffer layer on the organic charge transporting layer to prevent the damage from the sputtering process where a few certain characteristics are required such as material durability against the sputter damage and appropriate energy level for charge extraction. The buffer layer for TCO will be discussed in detail in the buffer layer section. To minimize sputter damage, various modifications and improvements have been reported for sputter systems. For example, the face target sputter (FTS) system has been widely employed, where the two targets face each other, confining the plasma to the vicinity of the target and reducing damage. Additionally, a metal and mesh shield can be inserted between the target and substrate to capture high-energy secondary electrons, resulting in improved OLED performance and reduced sputter damage (Fig. 15(c)).[168] The top TCO layer is the first layer that incident light passes through in the device stack, making it crucial for determining the overall amount of light inside the device. To minimize reflection at this layer, an anti-reflection (AR) layer is typically coated onto the TCO, which adjusts the refractive index between air and TCO. Low-refractive index materials such as LiF and MgF_2 are typically used for this purpose. E. Yang *et al.* recently reported that a meso–microporous SiO2 AR coating prepared *via* sol–gel phase separation can reduce reflectance to below 1% and increase transmittance up to ~99%, thereby improving light harvesting in perovskite/Si tandem solar cells.[169] A thinner TCO layer is optically beneficial; however, there is a trade-off between optical transparency and electrical conductivity, as excessively thin TCO layers may not provide sufficient lateral charge transport. To balance these trade-offs, the appropriate thickness of the TCO layer must be carefully determined through a trade-off analysis. Optical calculations, usually using the transfer matrix method, can readily optimize the thickness of both the AR layer and TCO layer (Fig. 16(a)). As previously mentioned, ITO and IZO are commonly used as the top electrode for the perovskite/Si tandem cell. However, Whal *et al.* reported that IZO could have potential benefits for the tandem application.[170] This is due to the fact that IZO does not require high-temperature annealing

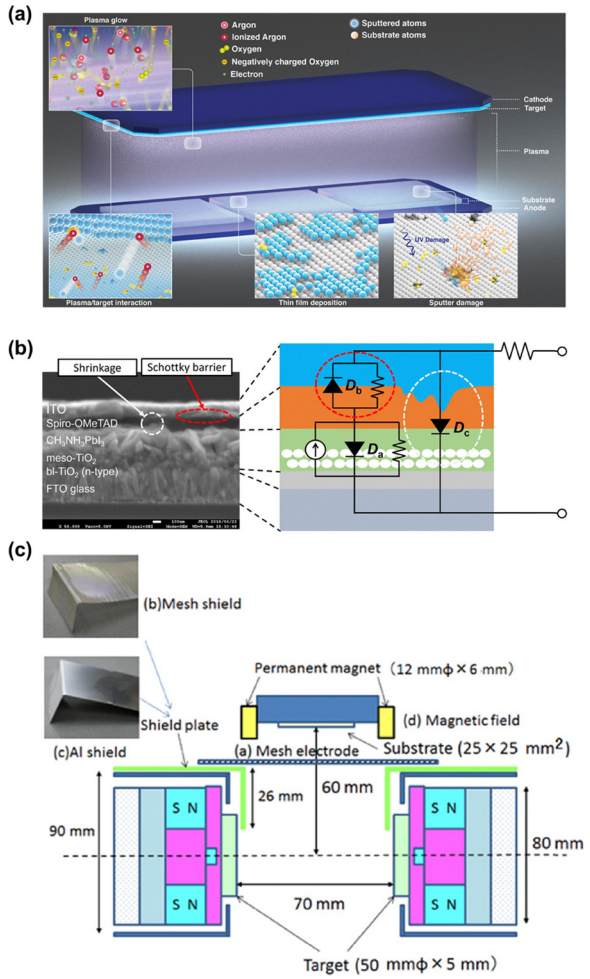

Fig. 15 (a) Schematic illustration describing sputter process. Reproduced with permission.[165] Copyright 2006, Elsevier Inc., (b) cross-sectional SEM image of the perovskite device and its circuit analysis causing additional path due to TCO sputter. Reproduced with permission.[166] Copyright 2016, American Chemical Society shield and shield plates. (c) Low damage sputter system by using face target, mesh shield and shield plates. Reproduced with permission.[168] Copyright 2016 The Japan Society of Applied Physics.

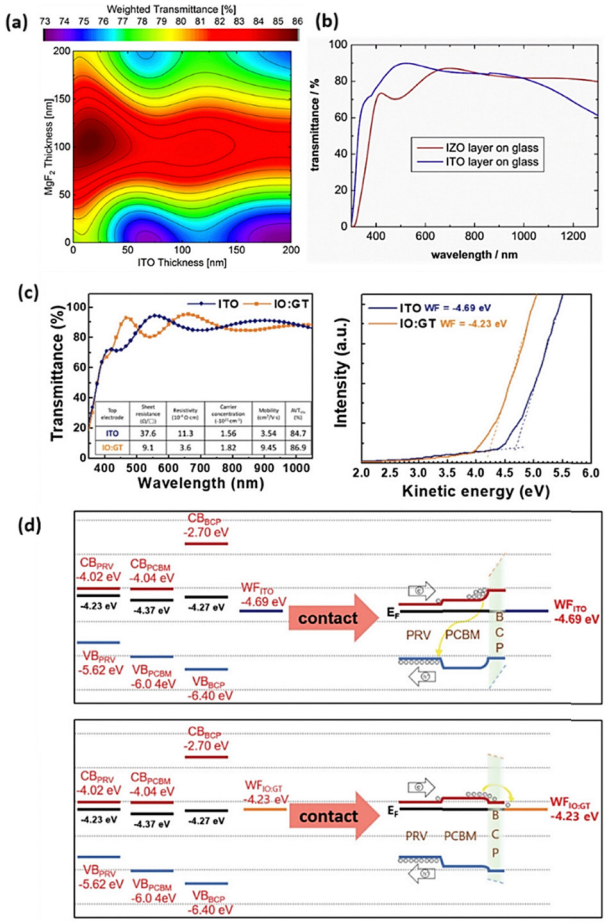

Fig. 16 (a) Simulated transmittance depending on thicknesses of IZO and MgF_2 using the transfer-matrix method. Reproduced with permission.[169] Copyright 2019 American Chemical Society. (b) Transmittance spectra of IZO and ITO. Reproduced with permission.[170] Copyright 2017 Elsevier. (c) Transmittance spectra (inset table: optical and electrical properties) and UPS spectra of ITO and gallium- and titanium-doped indium oxide (IO:GT) thin films. (d) Energy diagram of the perovskite device using ITO and (IO:GT). Reproduced with permission.[171] Copyright 2022 Wiley-VCH GmbH.

like ITO does, and it also exhibits higher transmittance at longer wavelengths (above 1000 nm) compared to ITO (Fig. 16(b)). In addition to the use of IZO instead of ITO, a method of applying titanium and tantalum-doped ITO to increase transparency in perovskite solar cells has also been reported (Fig. 16(c) and (d)).[171] Therefore, diversifying the materials used can be a good approach to increase the transparency of TCO.

The generated photocarriers are collected *via* lateral current of the TCO, hence the sheet resistance directly affects the performance of the solar cell. This becomes particularly important as the active area increases, as the loss from the TCO is proportional to sheet resistance and active area.[172] To overcome the sheet resistance of the TCO, a variety of alternative materials have been suggested such as carbon-based transparent conducting electrodes (TCE)s, metal nanowires and ultrathin metal.[173] However, due to suboptimal optoelectronic characteristics of these alternative materials, TCOs are widely being used as main components in high-efficiency perovskite/Si tandem.[122,174] Thus, to achieve high-performing top-perovskite cells in tandem, a practical approach could be to use TCOs in combination with a well-designed metal-mesh or metal busbar to improve the charge collection and alleviate the sheet resistance of the TCOs, particularly for large-area devices. In the following section, a detailed review of the metal-mesh or metal busbar will be provided.

The energy level of TCOs should be carefully considered, for example, a lower work function for the TCO on top of the ETL and a deeper work function for the top of the HTM. One typical method to adjust the energy level of TCOs is by varying the oxygen level, with a higher oxygen flow rate typically resulting in a deeper work function. ITO and IZO have different work functions, with ITO having a slightly shallower work function (4.6–4.7 eV) than IZO (~5.1 eV).[175,176] Additionally, doping other elements into the indium-based oxide target also affects the energy level. For instance, Yoon *et al.* reported that gallium and titanium-doped indium oxide (IO:GT) showed a work function of −4.23 eV, which is shallower than that of ITO (−4.69 eV).[171] Due to the favourable energy level for electron extraction, the modified TCO (IO:GT) allows for sputtering of the TCO on top of the PCBM/BCP layer, where typical ETLs are used in opaque cell structures with much higher PCE (17.9%) than when using ITO (PCE of 8.59%) and comparable PCE when using Ag (19.86%) (Fig. 16(c) and (d)). This study suggests that the additional process, such as ALD for TCO buffer layer, can be replaced by thermal vacuum evaporation *via* TCO engineering, which could be beneficial for mass production in terms of takt time. Recent developments have also explored alternative TCO compositions to enhance transparency and optical management. In particular, indium–gallium–tin oxide (IGTO) has been reported to exhibit improved near-infrared transparency while maintaining sufficient electrical conductivity, offering an effective route to minimize optical losses in perovskite/Si tandem configurations.[177]

Part II: external components of perovskite/Si tandem solar cells

Encapsulation

The hygroscopic and volatile nature of organic components in perovskite layers compromises moisture resistance and thermal stability, as exposure to humidity and heat leads to material decomposition. Effective encapsulation is therefore essential for ensuring long-term device performance and requires materials and processes tailored to the sensitivity of perovskite/Si tandem structures. Conventional encapsulation methods, such as heat lamination of polymer sheets, utilize high temperatures to melt and crosslink the encapsulant.[178] Ethylene-vinyl acetate (EVA), widely used in Si photovoltaics for its transparency and mechanical durability (Fig. 17(a)), exhibits a high processing temperature (>140 °C) that can degrade heat-sensitive perovskite layers.[179,180] Additionally, EVA generates acidic by-products during operation, accelerating perovskite decomposition. Surlyn, another common encapsulant for

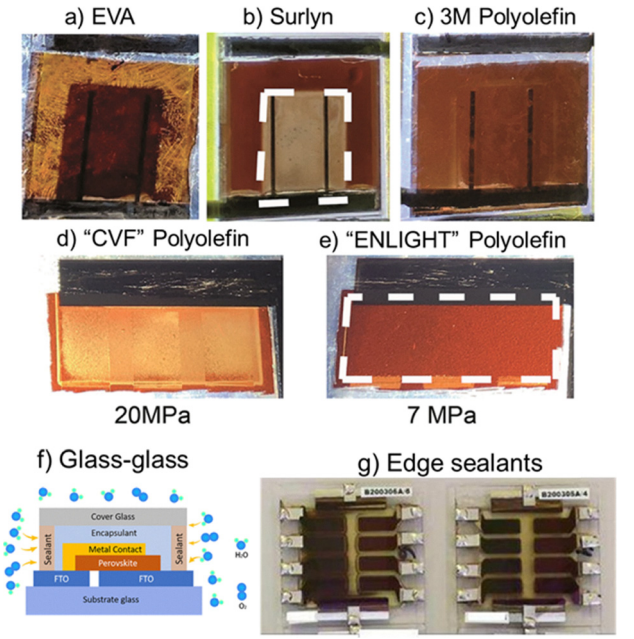

Fig. 17 Example of encapsulation (a)–(e) various polymers. Reproduced with permission.[181] Copyright 2018, The Royal Society of Chemistry. (f) Glass–glass, [186] Copyright 2022, American Chemical Society. Licensed under CC BY-NC-ND 4.0. (g) Edge sealants. Reproduced with permission.[184] Copyright 2024 International Solar Energy Society.

Si cells, suffers from poor adhesion to perovskite surfaces and thermal expansion mismatch, which can lead to delamination and moisture ingress (Fig. 17(b)).[181–183] In contrast, polyolefin has emerged as a promising low-temperature alternative (Fig. 17(c)). Checharoent *et al.* demonstrated that polyolefin, processed at 120 °C, offers improved compatibility with perovskite layers and can effectively replace EVA in perovskite/Si tandem solar cell encapsulation.[167]

Mechanical properties are also crucial for maintaining structural integrity during thermal cycling. Encapsulants with higher elastic moduli, such as CVF (20 MPa) and ENLIGHT (7 MPa), are more susceptible to cracking and delamination, leading to discoloration and device degradation after prolonged aging (*e.g.*, 1000 hours at 85 °C) (Fig. 17(d) and (e)). Encapsulants with a lower modulus have shown better mechanical compliance, preserving device integrity under stress. Promising alternatives to EVA include thermoplastic polyurethane (TPU) and polytetrafluoroethylene (PTFE), which offer low-temperature processability and better thermal expansion matching with perovskite layers, reducing the risk of mechanical and thermal failure.[185]

Beyond polymer-sheet encapsulants, glass-based packaging has been investigated to further improve durability (Fig. 17(f)).[186,187] Glass–glass encapsulation provides superior resistance to moisture and oxygen ingress together with high mechanical stiffness, ensuring excellent outdoor stability, although its weight and rigidity limit applications in lightweight or flexible modules.[188,189] Recent work has suggested low-temperature and low-stress glass–glass lamination schemes tailored for perovskite tandems to reduce thermal stress on the top absorber.[189] In comparison glass–polymer configurations, which replace the rear glass with a polymeric backsheet, offer reduced weight and greater flexibility.[186] However, their barrier performance strongly depends on edge sealing, as lateral diffusion pathways dominate moisture ingress. To this end, edge sealants play a decisive role. Butyl rubber (PIB) exhibits exceptionally low WVTR and strong adhesion, making it the most effective choice,[190] while epoxy-based sealants offer elasticity and thermal shock resistance at the cost of higher permeability (Fig. 17(g)).[184]

Hybrid encapsulation techniques further improve stability by combining the flexibility of organic polymers with the barrier properties of inorganic materials. Multilayer designs incorporating polymers with thin oxide layers (*e.g.*, Al_2O_3 or SiO_2) provide enhanced moisture protection and structural robustness.[191,192] Ionogel-based encapsulants offer additional tunability in mechanical, optical, and chemical properties through their liquid-phase matrix. Incorporating lead-absorbing monomers into ionogels mitigates lead leakage while enhancing chemical durability and mechanical cohesion.[193] In summary, these attempts highlight the need for encapsulation strategies that simultaneously account for thermal stress, humidity exposure, and mechanical durability. Polymer-based materials such as TPU, PTFE provide low temperature compatibility, glass–glass structures deliver the most robust environmental protection, and hybrid approaches including inorganic barriers promise to combine durability with additional safety functions. The optimal encapsulant must therefore be selected in close relation to device stack sensitivity and target module applications.

Busbar

Scalability of large-area perovskite/Si tandem modules is constrained by the relatively low current density of perovskite top cells (~20 mA cm^{-2}), which is approximately half that of conventional Si bottom cells (~40 mA cm^{-2}). This mismatch complicates current balancing and reduces tandem efficiency, particularly as device area increases. In addition to electrical constraints, the migration of mobile ions and volatile components in perovskite materials can lead to interfacial degradation and layer delamination, further compromising long-term operational stability.[94,194] To address these issues, optimizing busbar design is essential for efficient current collection, mechanical reliability, and compatibility with thermally sensitive perovskite layers. Metal grids, the primary component of busbar architecture, must provide low-resistance electrical pathways while remaining compatible with the TCO layer and scalable to large-area fabrication.[195] Although thermal evaporation is commonly used to fabricate metal grids in small-area tandem cells, its low throughput limits its suitability for commercial-scale production. In contrast, screen printing and roll-to-roll processing offer higher throughput and scalability but may suffer from increased contact resistance when interfaced with TCO layers. Kamino *et al.* reported that printed grids exhibited elevated series resistance, necessitating further refinement to maintain charge collection efficiency in scaled devices.[196]

Additionally, shingled cell interconnection has been adapted to perovskite/Si tandems, reducing optical shading and enabling higher packing density at the module level.[197]

Silver paste-based grids are widely adopted due to their high conductivity and proven reliability in current collection. However, their high sintering temperatures (>800 °C) are incompatible with perovskite materials. As a cost-effective alternative, copper offers lower raw material costs and potential for scalable processing. Yet, its susceptibility to oxidation can degrade electrical properties, requiring protective coatings or encapsulation layers. Although such strategies improve stability, they increase process complexity and may limit manufacturability. In addition, copper's higher intrinsic resistivity relative to silver may reduce overall conductivity, though this limitation can be mitigated through grid optimization—such as increasing line thickness or reducing spacing. The fabrication process for Si solar cells employing copper-based busbars typically involves screen-printing silver paste on the front side to form fine fingers and busbars, while a low-temperature Cu paste is applied to the rear side. The Cu rear contact is then co-fired and cured in a nitrogen atmosphere to complete the metallization. A comparison of Ag- and Cu-based tabbing structures reveals that the metal–semiconductor interface presents a critical region for carrier recombination. This area is particularly sensitive to interface passivation quality and doping gradients, which can exacerbate recombination losses. These considerations underscore the importance of careful junction engineering when integrating Cu metallization into perovskite/Si tandem cells (Fig. 18).[198–200] Recent tandem-oriented metallization studies further emphasize co-optimizing busbar geometry and low-thermal-budget processing to suppress series/contact-resistance growth during scale-up.[201]

Scalability of large-area perovskite/Si tandem modules is constrained by the relatively low current density of perovskite top cells (~20 mA cm^{-2}), which is approximately half that of conventional Si bottom cells (~40 mA cm^{-2}). This mismatch complicates current balancing and reduces tandem efficiency, particularly as device area increases. In addition to electrical constraints, the migration of mobile ions and volatile components in perovskite materials can lead to interfacial degradation and layer delamination, further compromising long-term operational stability.[194,202] To address these issues, optimizing busbar design is essential for efficient current collection, mechanical reliability, and compatibility with thermally sensitive perovskite layers.

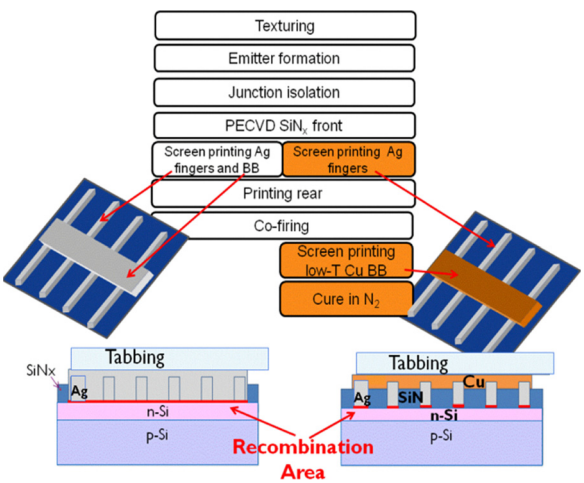

Fig. 18 Example of a Si solar cell using Cu busbar. Reproduced with permission.[202] Copyright 2014, Elsevier Inc.

Metal grids, the primary component of busbar architecture, must provide low-resistance electrical pathways while remaining compatible with the TCO layer and scalable to large-area fabrication.[195] Although thermal evaporation is commonly used to fabricate metal grids in small-area tandem commonly used to fabricate metal grids in small-area tandem cells, its low throughput limits its suitability for commercial-scale production. In contrast, screen printing and roll-to-roll processing offer higher throughput and scalability but may suffer from increased contact resistance when interfaced with TCO layers. Kamino *et al.* reported that printed grids exhibited elevated series resistance, necessitating further refinement to maintain charge collection efficiency in scaled devices.[196]

Additionally, shingled cell interconnection has been adapted to perovskite/Si tandems, reducing optical shading and enabling higher packing density at the module level.[197]

Beyond printing, scalable low-temperature metallization routes have also been demonstrated, including electroplated Cu busbars on 22.5 cm^2 two-terminal perovskite/Si tandems using an ALD-Al_2O_3 mask with a screen-printed Ag seed.[203]

Moreover, the environmental stability of busbars remains a critical issue. Under thermal cycling and humid conditions, metallic contacts are prone to corrosion and the adhesion between electrodes and encapsulant can deteriorate. These effects make pathways that diminish the fill factor and module stability.[204] To address this, busbar design should be carefully integrated with encapsulation strategies to guarantee efficient charge collection and improved resistance against moisture and heat induced degradation.[205,206] Table 3 summarizes representative specifications for screen-printed front-contact designs. Key parameters include a busbar width of 500–800 μm, finger width of 30–50 μm, and aspect ratios between 0.2 and 0.8, with a total metal coverage maintained below 5%. Minimizing finger and contact resistivity while ensuring TCO compatibility is critical to maintaining high fill factors and low series resistance in large-area modules.

Silver paste-based grids are widely adopted due to their high conductivity and proven reliability in current collection. However, their high sintering temperatures (>800 °C) are incompatible with perovskite materials. As a cost-effective alternative, copper offers lower raw material costs and potential for scalable processing. Yet, its susceptibility to oxidation can degrade electrical properties, requiring protective coatings or encapsulation layers. Although such strategies improve stability, they increase process complexity and may limit manufacturability. In addition, copper's higher intrinsic resistivity relative to silver may reduce overall conductivity, though this limitation can be mitigated through grid optimization—such as increasing line thickness or reducing spacing. The fabrication process for Si solar cells employing copper-based busbars typically involves screen-printing silver paste on the front side to form fine

Table 3 Characteristics of a metal grid applied by screen printing

Parameters	Unit	Screen-printed front contacts
Busbar width (w_b)	μm	500–800
Finger width (w_f)	μm	30–50
Average finger height (h_f)	μm	10–15
Aspect ratio (height to width)	—	0.2–0.8
Finger spacing (S)	mm	3–3.5
Metal coverage (finger + busbar)	%	4–5
Finger resistivity (ρ_f)	Ω cm	2–3
Contact resistivity (ρ_c)	mΩ cm^2	≤1
TCO sheet resistance (R_{sh})	Ω sq^{-1}	∼50
Temperature of contact formation (T)	°C	Low (<150)

fingers and busbars, while a low-temperature Cu paste is applied to the rear side. The Cu rear contact is then co-fired and cured in a nitrogen atmosphere to complete the metallization. A comparison of Ag- and Cu-based tabbing structures reveals that the metal–semiconductor interface presents a critical region for carrier recombination. This area is particularly sensitive to interface passivation quality and doping gradients, which can exacerbate recombination losses. These considerations underscore the importance of careful junction engineering when integrating Cu metallization into perovskite/Si tandem cells (Fig. 17).[198–200] Recent tandem-oriented metallization studies further emphasize co-optimizing busbar geometry and low-thermal-budget processing to suppress series/contact-resistance growth during scale-up.[201]

Part III: fabrication, cost and industrial considerations

For the successful commercialization of perovskite/Si tandem solar cells, achieving low production costs is crucial. Production costs are influenced by material expenses and process time, known as takt time.[207] Moreover, perovskite/Si tandem modules need to scale up to at least 166 mm by 166 mm, considering the widespread use of industrial Si wafers exceeding M6 size. However, the best power conversion efficiency (PCE) achieved for large area modules is 17.9%, compared to 25.7% for small unit cells, resulting in a PCE gap of approximately 30% in the single-junction perovskite solar cell section.[2] Furthermore, the scarcity of reports on perovskite/Si modules larger than M6 size suggests that upscaling the top perovskite solar cell is challenging.[208] Therefore, overcoming these challenges with a scalable process and appropriate takt time is crucial for the successful commercialization of perovskite/Si tandem solar cells.

Takt-time

The majority of high-efficiency perovskite/Si tandem solar cells reported to date have employed a p–i–n structure for the top perovskite solar cell, with a configuration consisting of ITO/NiO_x/SAM/Perovskite/Interlayer/C_{60}/SnO_x/IZO/busbar/AR as shown in Fig. 19(a), albeit with some variations across studies.[122,174,209,210] To achieve this configuration, a cycle of processes, including sputter-coating, blade coating, annealing, blade coating-heating, thermal evaporation, ALD-sputter, screen printing, and thermal evaporation, is required as illustrated in Fig. 18(b). However, due to the alternative use of solution-based and vacuum-based approaches, this set of processes could increase the interval time for loading and unloading samples into and out of the vacuum chamber, resulting in significant delays and inefficiency. This issue is especially critical for large-scale manufacturing, where takt time plays a crucial role in the overall efficiency and profitability of the production process. Thus, it is expected that a consistent coating process, such as a fully blade/slot-die/inkjet/or fully vacuum based process would be ultimately required for the successful manufacturing process.

Continuous scalable solution processes

To achieve a consistent coating process suitable for large-scale mass production, the air-processability of the coating method, whether blade, slot-die, spray coating, or ink-jet printing, is crucial. Most studies PSCs have employed spin coating in inert gas-filled glove boxes due to the sensitivity of the perovskite and other layers to ambient environments such as moisture and oxygen. Thus, manufacturing top PSCs for the perovskite/Si tandem applications in ambient or dry-air conditions can cause variations in film characteristics and low reproducibility, posing a great challenge for commercialization.[211,212] Moreover, the commonly used antisolvent dripping process may not be suitable for industrial mass production due to hazardous vapors and cost. In addition, in order to achieve reproducible and high-throughput processing, precursors in solution stock must have "weeks-long shelf lives" that guarantee identical film properties.[213] These issues pose a significant challenge as the direct application of spin coating in glove boxes to upscaled coating processes in ambient air may not be straightforward.

All-vacuum process

As a successful precedent can be observed in the OLED industry, a full-vacuum based process can be a promising solution for the perovskite top cell. The widely used structure for a top PSC in Fig. 18(b), ITO/NiO_x/SAM/Perovskite/LiF/C_{60}/SnO_2/IZO/LiF/Ag, is vacuum processable in principle.[152,214,215] Since Liu *et al.* reported the vacuum processed perovskite for the solar cell in 2012, numerous groups have reported on vacuum processed PSCs, including all-vacuum processed PSCs.[216] The advantages of vacuum processing for manufacturing optoelectronic devices include scalability, uniformity of the films, controllability of thickness, and freedom from environmental interference, making it a suitable process for industrial application. An important advantage, particularly for the application in perovskite/Si tandem, is that the top PSC cell can be conformally deposited on the textured Si surface. This characteristic results in optimizing the optical path of the tandem cell without requiring additional polishing for flattening the Si surface.[46,217]

However, further improvements are required for vacuum-processed perovskite solar cells (PSCs), including those used for the top cell in the perovskite/Si tandem, from various aspects. Firstly, the power conversion efficiencies (PCEs) of vacuum-processed PSCs are generally lower than those of solution-

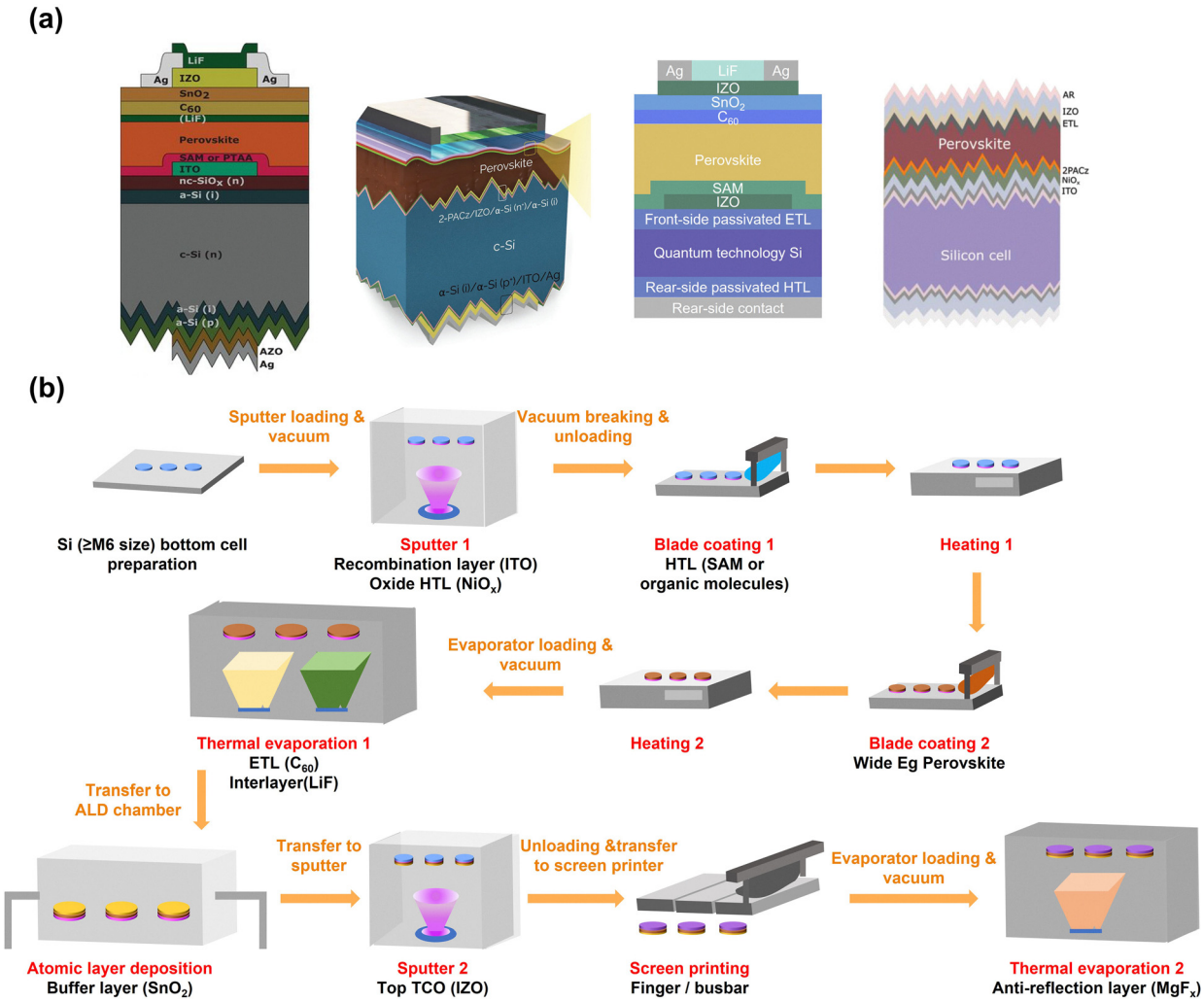

Fig. 19 (a) Schematic illustration of typically reported device structure for perovskite/Si tandem. Reproduced with permission.[122,174,209,210] Copyright 2020, American Association for the Advancement of Science, Copyright 2022, American Association for the Advancement of Science, Copyright 2022, American Chemical Society, Copyright 2022, Wiley-VCH GmbH respectively. (b) Schematic illustration of an example of a scalable fabrication process for a representative structure of a top perovskite solar cell in Si tandem configuration.

processed PSCs. Considering the breakthrough in PCE achieved through various additive engineering in solution processed PSCs, it could be reasonable to assume that similar efforts will be required to improve the PCE of vacuum processed PSCs. However, due to factors such as the high cost of equipment resulting in a high entry barrier for the vacuum process, there are relatively few papers and researchers in the field, which may have resulted in fundamental technological development may have been insufficient so far. In addition, compared to the solution process, it is challenging to incorporate numerous additives in the vacuum process since the number of precursors is limited by the number of sources (crucibles) in the chamber. Furthermore, it has not been validated whether perovskite precursors, especially organic halides, can be stably evaporated with the given conditions for mass production using linear-type sources that evaporate the sources for a long time at a fast rate. Therefore, numerous challenges and areas for further study exist in the development of vacuum-processed PSCs, particularly for the top cell of perovskite/Si tandems.

Cost

The market viability of PV technologies is heavily influenced by their LCOE, a key metric representing the average cost of electricity generation over a system's lifetime. LCOE is calculated using eqn (3) as the ratio of total lifetime costs to total electricity generated, incorporating the initial investment (I), operating and maintenance costs (OM), discount rate (r), electricity output (E), and annual degradation rate (d).[218]

$$\mathrm{LCOE} = \frac{\text{Total lifetime cost}}{\text{Total lifetime electricity production}} = \frac{I + \sum_{i=0}^{N} \frac{\mathrm{OM}}{(1+r)i}}{\sum_{i=0}^{N} \frac{E(1-d)^{i}}{(1+r)i}} \quad (3)$$

Perovskite/Si tandem solar cells generally exhibit higher PCE than single-junction cells, which enables greater energy yield

per unit area and helps reduce the LCOE despite their relatively more complex and costly manufacturing. While tandem devices currently report an LCOE of approximately \$0.32 and \$0.28 per kWh, respectively (Fig. 20(a)), these estimates assume utility-scale systems operating under standard irradiance conditions over a 25-year lifetime.[194,195] The superior energy output of tandem configurations offsets their slightly higher production costs, making them more cost-effective over the system's operational period. Importantly, McGovern *et al.* showed through techno-economic modeling that perovskite/Si tandem solar cells can achieve cost competitiveness with c-Si PV when an efficiency of $\geq$30%, annual degradation rate below 2% per year, and module manufacturing costs of $\sim$62.5 € per m^2 are simultaneously achieved.[219]

Efficiency improvement is one of the most direct strategies to reduce LCOE. For instance, Sofia *et al.* demonstrated that increasing the efficiency of the perovskite top cell from 18% to 24% lowered the LCOE from \$0.32 to \$0.22 per kWh by increasing total electricity output.[220] In addition to efficiency gains, reducing material and processing costs is essential. Expensive charge transport materials such as PCBM, spiro-OMeTAD, and PTAA significantly contribute to overall production costs (Fig. 19(b)).[218] Among them, PTAA, widely used as a hole transport layer, incurs particularly high material costs. To address this, researchers are developing cost-effective alternatives that retain comparable performance. Furthermore, scalable deposition directly shifts module MSP and thus slot-die coating offers very high material utilization ($\approx$99%),[221] and slot-die-processed perovskite/Si tandem solar cells reached 25.9% efficiency over 16 cm^2 area.[222] At the line level, a fully roll-to-roll printed perovskite projects $\approx$\$0.7 per W at 1 000 000 m^2 per year throughput.[223]

Encapsulation technologies also play a role in minimizing LCOE. Advances in hybrid and ionogel-based encapsulants enhance stability by reducing moisture ingress and degradation, thereby extending operational lifetime. For the design targets, robust PSC/PSM encapsulation typically pursues oxygen transmission rate (OTR) $\approx 10^{-4}$–10^{-6} cm^3 m^{-2} per day atm and water vapor transmission rate (WVTR) $\approx 10^{-3}$–10^{-6} cm^3 m^{-2} per day.[224] Ionogel encapsulation has passed International Electrotechnical Commission (IEC) 61 215 damp-heat/thermal-cycle tests and suppressed Pb leakage to undetectable levels after hail plus 24 h water soak;[225] on large-area devices, 110 cm^2 modules retained $\sim$84% of initial PCE after 1000 h at 85 °C (air), quantitatively lowering Annual Degradation Rate (ADR) inputs in LCOE.[226]

Concerns over intellectual property, supply chain, and toxicity regulations

PSCs are advancing rapidly toward industrial deployment, yet their commercialization depends as much on regulatory and economic considerations as on power-conversion efficiency. A central non-technical hurdle is intellectual property. Major research institutes and companies have assembled extensive

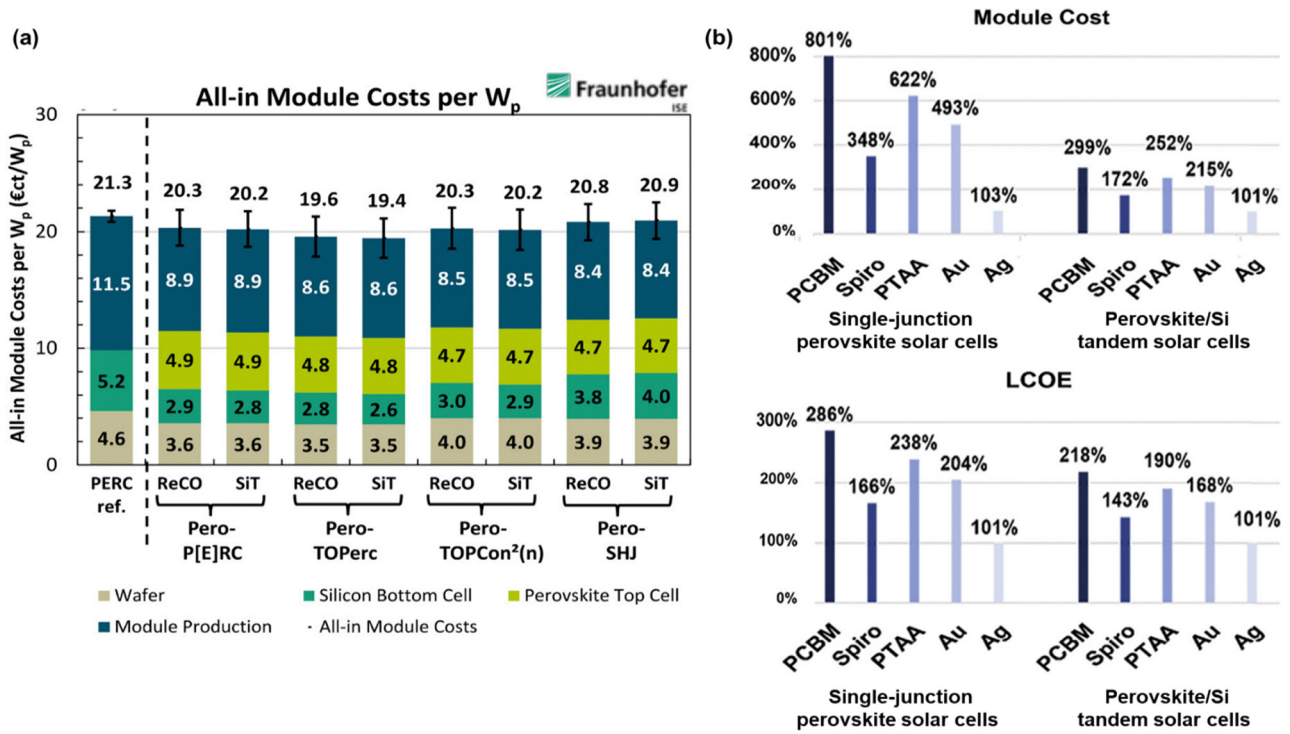

Fig. 20 (a) Module costs for all perovskite/Si tandem solar cells. ReCO: TCO-based RL, SiT: Si-based TJ. Reproduced with permission.[194] Copyright 2020, John Wiley & Sons Ltd, (b) perovskite single-junction and perovskite/Si solar cell module production cost and LCOE ratio by material. Reproduced with permission.[218] Copyright 2017, The Royal Society of Chemistry. Elsevier Inc.

patent portfolios that cover critical aspects of cell architecture, interfacial engineering, and tandem integration. Oxford PV, for example, has secured broad claims on perovskite–silicon tandem designs and has begun licensing agreements with large manufacturers, illustrating that freedom-to-operate analyses and potential cross-licensing will be essential for any entrant seeking to scale production. Competitive patent filings from firms such as Microquanta, LG, and Panasonic further reinforce the need for early legal strategies to avoid costly infringement disputes.

Commercial viability also hinges on supply chain resilience. Although perovskites can be processed at low temperatures, the materials ecosystem is far from trivial. Cesium, indium, high-purity lead iodide, and sophisticated encapsulation films are required at scale, and several of these precursors face potential scarcity or geographic concentration. A recent U.S. Department of Energy review highlights the vulnerability of global solar manufacturing to regional bottlenecks and price shocks, particularly because glass, substrates, and specialty chemicals remain dominated by a few suppliers. Terawatt-scale modeling likewise identifies cesium and indium as elements requiring careful resource planning for sustainable perovskite expansion.[227]

Toxicity associated with lead, the key light-absorbing cation in state-of-the-art perovskites, remains the most visible societal concern. Regulatory assessments show that uncontrolled lead release during module damage or end-of-life disposal can exceed drinking-water action levels, even though well-encapsulated devices can meet U.S. TCLP hazardous-waste limits.[228] Mitigation strategies include robust edge sealing, chemical sequestration of lead within the perovskite lattice, and closed-loop recycling processes capable of recovering both lead and rare transport materials.[229] These intertwined issues are now as decisive as cell efficiency in determining when and where perovskite modules will achieve true commercial impact. In parallel, emerging approaches such as chemisorption with functional groups (thiol, sulfonate, and phosphate) provide promising pathways to immobilize Pb^{2+} at the molecular level, complementing system-level recycling strategies. Together, these intertwined issues highlight that addressing non-technical barriers is as decisive as achieving record efficiencies, and they will strongly influence the timeline and geography of perovskite/Si tandem commercialization.[230]

Part IV: outlook and conclusions

Perovskite/Si tandem solar cells stand at the forefront of next-generation photovoltaics as they exceed the efficiency ceiling of single-junction devices. This review has addressed both recent advances and persistent bottlenecks across Si bottom cell configuration, wide-bandgap perovskites, ICLs, TCOs, encapsulation strategies, busbar design, scalable manufacturing processes, and levelized cost. Sustained progress in each of these areas will be crucial for translating lab-scale demonstrations into commercially viable modules.

In tandem integration, the selection of Si bottom cells strongly influences both device performance and manufacturability. PERC, while dominant in current production, imposes a practical limit on achievable tandem efficiency. TOPCon provides improved surface passivation and maintains compatibility with high-throughput industrial processing while parasitic absorption in poly-Si layers should be minimized. SHJ has achieved record efficiencies through effective interface passivation, but its reliance on a-Si:H-based passivation and doped contact layers leads to thermal instability, which poses a challenge to scale up. Developing passivation schemes with a low thermal budget can provide a viable solution to the scale-up challenge. For the perovskite top cell, efficiency has already reached competitive levels, but stability remains the primary hurdle. Long-term reliability is undermined by halide segregation, defect evolution, and ambient-induced degradation. Defect management in both the bulk and interfaces is therefore critical to addressing the stability challenge: in the bulk, achieving high crystallinity and implementing novel defect passivation strategies are essential to suppress defect formation while at the interfaces introducing passivation layers can enhance material stability and extend device lifetime. In the ICL design, efficient carrier recombination should be achieved while minimizing optical and electrical losses. RJs, including TCOs offer high transmittance, but their limited conductivity can lead to carrier accumulation, voltage loss, and lateral shunting. Introduction of transport layers that can meet optical index matching can limit lateral carrier conduction while preserving transparency. TJs, in contrast, present high vertical conductivity through quantum tunneling, but free-carrier absorption and defect-assisted recombination can cause optical loss. Such losses can be alleviated through precise doping control and effective interface passivation. For the top electrodes of perovskite/Si tandem solar cells, TCOs are the most widely used, but their deposition by sputtering can damage the underlying layers. The sputter-induced damage is usually mitigated by protective buffer layers and optimized sputtering conditions. A further challenge is to balance optical transparency with electrical conductivity, which is often managed by incorporating metal–mesh grids to reduce resistive losses. Moreover, tuning the TCO work function to achieve suitable energy-level alignment with transport layers is essential for effective charge extraction.

For external components, robust encapsulation is vital to ensure long-term durability. In busbar design, adopting Cu-based metallization improves current collection by lowering series resistance and resistive heating, while also supporting scalability for large-area modules through high conductivity and mechanical reliability under thermal cycling, which in turn enables cost reduction. As tandem modules move toward commercial deployment, scalable and low-cost fabrication strategies will be indispensable. Solution-based processes offer high throughput, whereas vacuum-based techniques provide superior uniformity and film integrity. Thus, hybrid manufacturing approaches may integrate these advantages to meet industrial requirements, but continued advances in process engineering will be necessary to achieve cost targets without compromising long-term device performance.

Globally, perovskite solar cell technology has already entered the commercialization stage, led most prominently by

China and followed by the United States, Europe, and other regions in Asia. Microquanta is currently operating a production line with an annual capacity of approximately 100 MW dedicated to building integrated photovoltaic (BIPV) applications. GCL has completed a 1 GW production line and is now expanding toward a 2 GW facility capable of fabricating tandem modules with an area of 2.76 m^2. Other Chinese companies such as Utmolight and Renshine Solar have each installed production lines of around 150 MW and have begun commercial deployment. In Japan, the government has pledged 1.5 billion USD to support mass production of perovskite solar cells in collaboration with Sekisui Chemical, targeting completion of a 150 MW line by 2027 and a 1 GW line by 2030. In Korea, Hanwha Q Cells has established a 40 MW line and announced plans for full-scale production in the second half of 2026. In the United States, companies including Cubic PV, Swift Solar, and First Solar have launched or announced pilot line projects as they enter the race for commercialization. Taken together, these developments indicate that perovskite solar cells are now firmly on a commercial trajectory, with the decisive phase of widespread market adoption expected to emerge well within the next three years, and potentially sooner. Alongside these advances, rigorous accelerated lifetime testing, including ISOS protocols, damp heat exposure, and thermal cycling, as well as outdoor field validation under fluctuating humidity, temperature, and illumination conditions, remains essential to evaluate long-term operational stability. These studies provide benchmarks for certification and bankability, ensuring reliable projections for industrial deployment.

Conflicts of interest

There are no conflicts to declare.

Data availability

No primary research results, software or code have been included and no new data were generated or analysed as part of this review.

Acknowledgements

This work was supported by the Digital Research Innovation Institution Program through the National Research Foundation of Korea (NRF) funded by the Korea government (MSIT) (RS-2023-00283597), and was supported as a project no. KS2522-30 and supported by the Korea Research Institute of Chemical Technology (KRICT).

Notes and references

1 D. M. Chapin, C. S. Fuller and G. L. Pearson, A New Silicon p–n Junction Photocell for Converting Solar Radiation into Electrical Power, *J. Appl. Phys.*, 1954, **25**, 676–677.

2 *Best Research-Cell Efficiency Chart*, **https://www.nrel.gov/pv/cell-efficiency.html**.

3 J. S. Kim, J.-M. Heo, G.-S. Park, S.-J. Woo, C. Cho, H. J. Yun, D.-H. Kim, J. Park, S.-C. Lee, S.-H. Park, E. Yoon, N. C. Greenham and T.-W. Lee, Ultra-bright, efficient and stable perovskite light-emitting diodes, *Nature*, 2022, **611**, 688–694.

4 Y. Lian, Y. Wang, Y. Yuan, Z. Ren, W. Tang, Z. Liu, S. Xing, K. Ji, B. Yuan, Y. Yang, Y. Gao, S. Zhang, K. Zhou, G. Zhang, S. D. Stranks, B. Zhao and D. Di, Downscaling micro- and nano-perovskite LEDs, *Nature*, 2025, **640**, 62–68.

5 B. Zhao, M. Vasilopoulou, A. Fakharuddin, F. Gao, Abd R. B. Mohd Yusoff, R. H. Friend and D. Di, Light management for perovskite light-emitting diodes, *Nat. Nanotechnol.*, 2023, **18**, 981–992.

6 C. Zou, Z. Ren, K. Hui, Z. Wang, Y. Fan, Y. Yang, B. Yuan, B. Zhao and D. Di, Electrically driven lasing from a dual-cavity perovskite device, *Nature*, 2025, **645**, 369–374.

7 L. Min, H. Sun, L. Guo, M. Wang, F. Cao, J. Zhong and L. Li, Frequency-selective perovskite photodetector for anti-interference optical communications, *Nat. Commun.*, 2024, **15**, 2066.

8 A. Kojima, K. Teshima, Y. Shirai and T. Miyasaka, Organometal Halide Perovskites as Visible-Light Sensitizers for Photovoltaic Cells, *J. Am. Chem. Soc.*, 2009, **131**, 6050–6051.

9 A. Richter, M. Hermle and S. W. Glunz, Reassessment of the Limiting Efficiency for Crystalline Silicon Solar Cells, *IEEE J. Photovolt.*, 2013, **3**, 1184–1191.

10 S. Schafer and R. Brendel, Accurate Calculation of the Absorptance Enhances Efficiency Limit of Crystalline Silicon Solar Cells With Lambertian Light Trapping, *IEEE J. Photovolt.*, 2018, **8**, 1156–1158.

11 N.-G. Park and H. Segawa, Research Direction toward Theoretical Efficiency in Perovskite Solar Cells, *ACS Photonics*, 2018, **5**, 2970–2977.

12 P. Loper, B. Niesen, S.-J. Moon, S. Martin De Nicolas, J. Holovsky, Z. Remes, M. Ledinsky, F.-J. Haug, J.-H. Yum, S. De Wolf and C. Ballif, Organic–Inorganic Halide Perovskites: Perspectives for Silicon-Based Tandem Solar Cells, *IEEE J. Photovolt.*, 2014, **4**, 1545–1551.

13 I. Almansouri, A. Ho-Baillie, S. P. Bremner and M. A. Green, Supercharging Silicon Solar Cell Performance by Means of Multijunction Concept, *IEEE J. Photovolt.*, 2015, **5**, 968–976.

14 F. Jiang, T. Liu, B. Luo, J. Tong, F. Qin, S. Xiong, Z. Li and Y. Zhou, A two-terminal perovskite/perovskite tandem solar cell, *J. Mater. Chem. A*, 2016, **4**, 1208–1213.

15 J. Burschka, N. Pellet, S.-J. Moon, R. Humphry-Baker, P. Gao, M. K. Nazeeruddin and M. Grätzel, Sequential deposition as a route to high-performance perovskite-sensitized solar cells, *Nature*, 2013, **499**, 316–319.

16 W. Liao, D. Zhao, Y. Yu, N. Shrestha, K. Ghimire, C. R. Grice, C. Wang, Y. Xiao, A. J. Cimaroli, R. J. Ellingson, N. J. Podraza, K. Zhu, R.-G. Xiong and Y. Yan, Fabrication of Efficient Low-Bandgap Perovskite Solar Cells by Combining Formamidinium Tin Iodide with

Methylammonium Lead Iodide, *J. Am. Chem. Soc.*, 2016, **138**, 12360–12363.
17 S. Mondal, M. Chaudhury, P. Chakrabarti and S. Maity, Band Gap-Tailored Two-Terminal Lead-Free Germanium- and Tin-Based Single-Halide Perovskite Materials for Efficient Tandem Solar Cells, *Energy Fuels*, 2023, **37**, 12301–12318.
18 S. Baruah, J. Borah and S. Maity, Device engineering of a new lead free all inorganic CsSnI3/CsSnCl3 based graded perovskite absorber structure for high performance solar cell, *IEEE J. Quantum Electron.*, 2025, 1.
19 S. Baruah, J. Borah and S. Maity, Device optimization of all inorganic $CsPbBr_3$/LNMO based multi-layered perovskite light harvesters for broader capturing of solar spectrum, *Sol. Energy*, 2024, **280**, 112858.
20 S. Mondal, S. De and S. Maity, in 2025 IEEE 53rd Photovoltaic Specialists Conference (PVSC), 2025, pp. 0603–0605.
21 S. De, R. Bhar, A. Pangas, S. Mondal, B. K. Dubey and S. Maity, Resource efficient metal extraction and silicon wafer recovery from end-of-life monocrystalline solar cells: A chemical and environmental perspective, *Waste Manag.*, 2025, **203**, 114867.
22 K. ElKhamisy, H. Abdelhamid, E.-S. M. El-Rabaie and N. Abdel-Salam, A Comprehensive Survey of Silicon Thin-film Solar Cell: Challenges and Novel Trends, *Plasmonics*, 2024, **19**, 1–20.
23 A. Richter, R. Müller, J. Benick, F. Feldmann, B. Steinhauser, C. Reichel, A. Fell, M. Bivour, M. Hermle and S. W. Glunz, Design rules for high-efficiency both-sides-contacted silicon solar cells with balanced charge carrier transport and recombination losses, *Nat. Energy*, 2021, **6**, 429–438.
24 C. Sen, X. Wu, H. Wang, M. U. Khan, L. Mao, F. Jiang, T. Xu, G. Zhang, C. Chan and B. Hoex, Accelerated damp-heat testing at the cell-level of bifacial silicon HJT, PERC and TOPCon solar cells using sodium chloride, *Sol. Energy Mater. Sol. Cells*, 2023, **262**, 112554.
25 M. H. Norouzi, P. Saint-Cast, U. Jaeger, B. Steinhauser, J. Benick, A. Buechler, B. Bitnar, P. Palinginis, H. Neuhaus, A. Wolf and M. Hofmann, Development and Characterization of AlO_x/SiN_x:B Layer Systems for Surface Passivation and Local Laser Doping, *IEEE J. Photovolt.*, 2017, **7**, 1244–1253.
26 G. Kökbudak, E. Orhan, F. Es, E. Semiz and R. Turan, in 2018 International Conference on Photovoltaic Science and Technologies (PVCon), 2018, pp. 1–5.
27 J. Schmidt, A. Merkle, R. Brendel, B. Hoex, M. C. M. van de Sanden and W. M. M. Kessels, Surface Passivation of High-efficiency Silicon Solar Cells by Atomic-layer-deposited Al_2O_3, *Prog. Photovolt. Res. Appl.*, 2008, **16**, 461–466.
28 B. Hoex, J. Schmidt, R. Bock, P. P. Altermatt, M. C. M. van de Sanden and W. M. M. Kessels, Excellent passivation of highly doped p-type Si surfaces by the negative-charge-dielectric Al_2O_3, *Appl. Phys. Lett*, 2007, **91**, 112107.
29 A. Belghachi, in 2013 International Renewable and Sustainable Energy Conference (IRSEC), 2013, pp. 161–166.
30 S. Wakamiya, N. Matsuo, T. Kobayashi and A. Heya, in 2014 IEEE International Meeting for Future of Electron Devices, Kansai (IMFEDK), 2014, pp. 1–2.
31 S. W. Glunz and F. Feldmann, SiO_2 surface passivation layers – a key technology for silicon solar cells, *Sol. Energy Mater. Sol. Cells*, 2018, **185**, 260–269.
32 F. Feldmann, M. Bivour, C. Reichel, M. Hermle and S. W. Glunz, Passivated rear contacts for high-efficiency n-type Si solar cells providing high interface passivation quality and excellent transport characteristics, *Sol. Energy Mater. Sol. Cells*, 2014, **120**, 270–274.
33 A. Moldovan, F. Feldmann, K. Kaufmann, S. Richter, M. Werner, C. Hagendorf, M. Zimmer, J. Rentsch and M. Hermle, in 2015 IEEE 42nd Photovoltaic Specialist Conference (PVSC), 2015, pp. 1–6.
34 Z. Zhang, Y. Zeng, C.-S. Jiang, Y. Huang, M. Liao, H. Tong, M. Al-Jassim, P. Gao, C. Shou, X. Zhou, B. Yan and J. Ye, Carrier transport through the ultrathin silicon-oxide layer in tunnel oxide passivated contact (TOPCon) c-Si solar cells, *Sol. Energy Mater. Sol. Cells*, 2018, **187**, 113–122.
35 S. W. Glunz, B. Steinhauser, J.-I. Polzin, C. Luderer, B. Grübel, T. Niewelt, A. M. O. M. Okasha, M. Bories, H. Nagel, K. Krieg, F. Feldmann, A. Richter, M. Bivour and M. Hermle, Silicon-based passivating contacts: The TOPCon route, *Prog. Photovolt. Res. Appl.*, 2023, **31**, 341–359.
36 V. Kanneboina, Detailed review on c-Si/a-Si:H heterojunction solar cells in perspective of experimental and simulation, *Microelectron. Eng.*, 2022, **265**, 111884.
37 L. A. Kasprzak, R. B. Laibowitz and M. Ohring, Dependence of the Si–SiO_2 barrier height on SiO_2 thickness in MOS tunnel structures, *J. Appl. Phys*, 1977, **48**, 4281–4286.
38 F. Feldmann, M. B. C. Reichel, M. Hermle and S. W. Glunz, A Passivated Rear Contact for High-efficiency n-type Silicon Solar Cells Enabling High Vocs and FF $>$ 82%.
39 V. Steckenreiter, D. C. Walter and J. Schmidt, Kinetics of the permanent deactivation of the boron-oxygen complex in crystalline silicon as a function of illumination intensity, *AIP Adv.*, 2017, **7**, 035305.
40 D. K. Ghosh, S. Bose, G. Das, S. Acharyya, A. Nandi, S. Mukhopadhyay and A. Sengupta, Fundamentals, present status and future perspective of TOPCon solar cells: A comprehensive review, *Surf. Interfaces*, 2022, **30**, 101917.
41 S. Albrecht, M. Saliba, J. P. C. Baena, F. Lang, L. Kegelmann, M. Mews, L. Steier, A. Abate, J. Rappich, L. Korte, R. Schlatmann, M. Khaja Nazeeruddin, A. Hagfeldt, M. Grätzel and B. Rech, Monolithic perovskite/silicon-heterojunction tandem solar cells processed at low temperature, *Energy Environ. Sci.*, 2016, **9**, 81–88.
42 P. Procel, H. Xu, A. Saez, C. Ruiz-Tobon, L. Mazzarella, Y. Zhao, C. Han, G. Yang, M. Zeman and O. Isabella, The role of heterointerfaces and subgap energy states on transport mechanisms in silicon heterojunction solar cells, *Prog. Photovolt. Res. Appl.*, 2020, **28**, 935–945.
43 Q. Wang, W. Wu, N. Yuan, Y. Li, Y. Zhang and J. Ding, Influence of SiO_x film thickness on electrical performance

and efficiency of TOPCon solar cells, *Sol. Energy Mater. Sol. Cells*, 2020, **208**, 110423.

44 F. Sahli, J. Werner, B. A. Kamino, M. Bräuninger, R. Monnard, B. Paviet-Salomon, L. Barraud, L. Ding, J. J. Diaz Leon, D. Sacchetto, G. Cattaneo, M. Despeisse, M. Boccard, S. Nicolay, Q. Jeangros, B. Niesen and C. Ballif, Fully textured monolithic perovskite/silicon tandem solar cells with 25.2% power conversion efficiency, *Nat. Mater.*, 2018, **17**, 820–826.

45 L. Mao, T. Yang, H. Zhang, J. Shi, Y. Hu, P. Zeng, F. Li, J. Gong, X. Fang, Y. Sun, X. Liu, J. Du, A. Han, L. Zhang, W. Liu, F. Meng, X. Cui, Z. Liu and M. Liu, Fully Textured, Production-Line Compatible Monolithic Perovskite/Silicon Tandem Solar Cells Approaching 29% Efficiency, *Adv. Mater.*, 2022, **34**, 2206193.

46 F. Sahli, J. Werner, B. A. Kamino, M. Bräuninger, R. Monnard, B. Paviet-Salomon, L. Barraud, L. Ding, J. J. Diaz Leon, D. Sacchetto, G. Cattaneo, M. Despeisse, M. Boccard, S. Nicolay, Q. Jeangros, B. Niesen and C. Ballif, Fully textured monolithic perovskite/silicon tandem solar cells with 25.2% power conversion efficiency, *Nat. Mater.*, 2018, **17**, 820–826.

47 P. Papet, O. Nichiporuk, A. Kaminski, Y. Rozier, J. Kraiem, J.-F. Lelievre, A. Chaumartin, A. Fave and M. Lemiti, Pyramidal texturing of silicon solar cell with TMAH chemical anisotropic etching, *Sol. Energy Mater. Sol. Cells*, 2006, **90**, 2319–2328.

48 W. Liang, T. Kho, J. Tong, P. Narangari, S. Armand, M. Ernst, D. Walter, S. Surve, M. Stocks, A. Blakers and K. C. Fong, Highly reproducible c-Si texturing by metal-free TMAH etchant and monoTEX agent, *Sol. Energy Mater. Sol. Cells*, 2021, **222**, 110909.

49 H. Kanda, N. Shibayama, A. Uzum, T. Umeyama, H. Imahori, K. Ibi and S. Ito, Effect of Silicon Surface for Perovskite/Silicon Tandem Solar Cells: Flat or Textured ?, *ACS Appl. Mater. Interfaces*, 2018, **10**, 35016–35024.

50 B. Chen, Z. J. Yu, S. Manzoor, S. Wang, W. Weigand, Z. Yu, G. Yang, Z. Ni, X. Dai, Z. C. Holman and J. Huang, Blade-Coated Perovskites on Textured Silicon for 26%-Efficient Monolithic Perovskite/Silicon Tandem Solar Cells, *Joule*, 2020, **4**, 850–864.

51 Y. Hou, E. Aydin, M. De Bastiani, C. Xiao, F. H. Isikgor, D.-J. Xue, B. Chen, H. Chen, B. Bahrami, A. H. Chowdhury, A. Johnston, S.-W. Baek, Z. Huang, M. Wei, Y. Dong, J. Troughton, R. Jalmood, A. J. Mirabelli, T. G. Allen, E. Van Kerschaver, M. I. Saidaminov, D. Baran, Q. Qiao, K. Zhu, S. De Wolf and E. H. Sargent, Efficient tandem solar cells with solution-processed perovskite on textured crystalline silicon, *Science*, 2020, **367**, 1135–1140.

52 G. Nogay, F. Sahli, J. Werner, R. Monnard, M. Boccard, M. Despeisse, F.-J. Haug, Q. Jeangros, A. Ingenito and C. Ballif, 25.1%-Efficient Monolithic Perovskite/Silicon Tandem Solar Cell Based on a p-type Monocrystalline Textured Silicon Wafer and High-Temperature Passivating Contacts, *ACS Energy Lett.*, 2019, **4**, 844–845.

53 Y. Wu, D. Yan, J. Peng, T. Duong, Y. Wan, S. P. Phang, H. Shen, N. Wu, C. Barugkin, X. Fu, S. Surve, D. Grant, D. Walter, T. P. White, K. R. Catchpole and K. J. Weber, Monolithic perovskite/silicon-homojunction tandem solar cell with over 22% efficiency, *Energy Environ. Sci.*, 2017, **10**, 2472–2479.

54 S. Sadhukhan, S. Acharyya, T. Panda, N. C. Mandal, G. Das, S. Maity, P. Chaudhuri, S. Chakraborty and H. Saha, TOPerc Solar Cell: An Integral Approach of Tunnel Oxide Passivated Contact (TOPCon) and Passivated Emitter and Rear Contact (PERC) Architectures for Achieving Efficiency Beyond 25%, *Energy Technol.*, 2023, **11**, 2300200.

55 M. A. Green, The Passivated Emitter and Rear Cell (PERC): From conception to mass production, *Sol. Energy Mater. Sol. Cells*, 2015, **143**, 190–197.

56 Z. Ding, Z. Liu, M. Xing, X. Xue, W. Yang, W. Liu, M. Liao, Z. Yang, Y. Zeng and J. Ye, Highly Transparent Oxygen-Doped Poly-Si with *In situ* N_2O Oxidant for Poly-Si Passivating Contacts in Perovskite/Silicon Tandem Solar Cells, *Sol. RRL*, 2024, **8**, 2400134.

57 F. Feldmann, M. Nicolai, R. Müller, C. Reichel and M. Hermle, Optical and electrical characterization of poly-Si/SiO_x contacts and their implications on solar cell design, *Energy Procedia*, 2017, **124**, 31–37.

58 C. L. Anderson, H. L. Guthrey, A. S. Kale, W. Nemeth, M. Page, D. L. Young, P. Stradins and S. Agarwal, Understanding SiO_x Layer Breakup in poly-Si/SiO_x Passivating Contacts for Si Solar Cells Using Precisely Engineered Surface Textures, *ACS Appl. Energy Mater.*, 2022, **5**, 3043–3051.

59 S. Jiang, Z. Ding, X. Li, L. Zhang, Z. Ying, X. Yang, Z. Yang, W. Yang, Y. Zeng and J. Ye, Advancing Monolithic Perovskite/TOPCon Tandem Solar Cells by Customizing Industrial-Level Micro-Nano Structures, *Adv. Funct. Mater.*, 2024, **34**, 2401900.

60 H. Wu, F. Ye, M. Yang, F. Luo, X. Tang, Q. Tang, H. Qiu, Z. Huang, G. Wang, Z. Sun, H. Lin, J. Wei, Y. Li, X. Tian, J. Zhang, L. Xie, X. Deng, T. Yuan, M. Yu, Y. Liu, P. Li, H. Chen, S. Zhou, Q. Xu, P. Li, J. Duan, J. Chen, C. Li, S. Yin, B. Liu, C. Sun, Q. Su, Y. Wang, H. Deng, T. Xie, P. Gao, Q. Kang, Y. Zhang, H. Yan, N. Yuan, F. Peng, Y. Yuan, X. Ru, B. He, L. Chen, J. Wang, J. Lu, M. Qu, C. Xue, J. Ding, L. Fang, Z. Li and X. Xu, Silicon heterojunction back-contact solar cells by laser patterning, *Nature*, 2024, **635**, 604–609.

61 M. A. Green, E. D. Dunlop, M. Yoshita, N. Kopidakis, K. Bothe, G. Siefer and X. Hao, Solar cell efficiency tables (version 62), *Prog. Photovolt. Res. Appl.*, 2023, **31**, 651–663.

62 J. C. Bruyère, A. Deneuville, A. Mini, J. Fontenille and R. Danielou, Influence of hydrogen on optical properties of a-Si:: H, *J. Appl. Phys.*, 1980, **51**, 2199–2205.

63 M. Faycal Atitar, A. A. Ismail, S. A. Al-Sayari, D. Bahnemann, D. Afanasev and A. V. Emeline, Mesoporous TiO_2 nanocrystals as efficient photocatalysts: Impact of calcination temperature and phase transformation on photocatalytic performance, *Chem. Eng. J.*, 2015, **264**, 417–424.

64 V. H. Nguyen, H. Tran Thi My, H. T. T. Ta, K. A. Vuong, H. H. Nguyen, T. T. Nguyen, N. L. Nguyen and H. Van Bui,

Unraveling the limiting factors to electron mobility in degenerately doped SnO_2 thin films, *Adv. Nat. Sci. Nanosci. Nanotechnol.*, 2023, **14**, 045008.

65 J. Park, J. Kim, H.-S. Yun, M. J. Paik, E. Noh, H. J. Mun, M. G. Kim, T. J. Shin and S. I. Seok, Controlled growth of perovskite layers with volatile alkylammonium chlorides, *Nature*, 2023, **616**, 724–730.

66 Y. Guo, X. Yin, J. Liu and W. Que, Focusing on mixed-halide Br-rich perovskite solar cells: An inevitable open-circuit voltage deficit derived from photoinduced halide segregation ?, *Matter*, 2022, **5**, 2015–2030.

67 T. Huang, S. Tan, S. Nuryyeva, I. Yavuz, F. Babbe, Y. Zhao, M. Abdelsamie, M. H. Weber, R. Wang, K. N. Houk, C. M. Sutter-Fella and Y. Yang, Performance-limiting formation dynamics in mixed-halide perovskites, *Sci. Adv.*, 2021, **7**, eabj1799.

68 E. T. Hoke, D. J. Slotcavage, E. R. Dohner, A. R. Bowring, H. I. Karunadasa and M. D. McGehee, Reversible photo-induced trap formation in mixed-halide hybrid perovskites for photovoltaics, *Chem. Sci.*, 2015, **6**, 613–617.

69 R. D. J. Oliver, P. Caprioglio, F. Peña-Camargo, L. R. V. Buizza, F. Zu, A. J. Ramadan, S. G. Motti, S. Mahesh, M. M. McCarthy, J. H. Warby, Y.-H. Lin, N. Koch, S. Albrecht, L. M. Herz, M. B. Johnston, D. Neher, M. Stolterfoht and H. J. Snaith, Understanding and suppressing non-radiative losses in methylammonium-free wide-bandgap perovskite solar cells, *Energy Environ. Sci.*, 2022, **15**, 714–726.

70 F. Peña-Camargo, P. Caprioglio, F. Zu, E. Gutierrez-Partida, C. M. Wolff, K. Brinkmann, S. Albrecht, T. Riedl, N. Koch, D. Neher and M. Stolterfoht, Halide Segregation versus Interfacial Recombination in Bromide-Rich Wide-Gap Perovskite Solar Cells, *ACS Energy Lett.*, 2020, **5**, 2728–2736.

71 S. Mahesh, J. M. Ball, R. D. J. Oliver, D. P. McMeekin, P. K. Nayak, M. B. Johnston and H. J. Snaith, Revealing the origin of voltage loss in mixed-halide perovskite solar cells, *Energy Environ. Sci.*, 2020, **13**, 258–267.

72 S. Mahesh, J. M. Ball, R. D. J. Oliver, D. P. McMeekin, P. K. Nayak, M. B. Johnston and H. J. Snaith, Revealing the origin of voltage loss in mixed-halide perovskite solar cells, *Energy Environ. Sci.*, 2020, **13**, 258–267.

73 G. Yang, Z. Ni, Z. J. Yu, B. W. Larson, Z. Yu, B. Chen, A. Alasfour, X. Xiao, J. M. Luther, Z. C. Holman and J. Huang, Defect engineering in wide-bandgap perovskites for efficient perovskite–silicon tandem solar cells, *Nat. Photonics*, 2022, **16**, 588–594.

74 Y. Lin, B. Chen, F. Zhao, X. Zheng, Y. Deng, Y. Shao, Y. Fang, Y. Bai, C. Wang and J. Huang, Matching Charge Extraction Contact for Wide-Bandgap Perovskite Solar Cells, *Adv. Mater.*, 2017, **29**, 1700607.

75 J. Warby, F. Zu, S. Zeiske, E. Gutierrez-Partida, L. Frohloff, S. Kahmann, K. Frohna, E. Mosconi, E. Radicchi, F. Lang, S. Shah, F. Peña-Camargo, H. Hempel, T. Unold, N. Koch, A. Armin, F. De Angelis, S. D. Stranks, D. Neher and M. Stolterfoht, Understanding Performance Limiting Interfacial Recombination in pin Perovskite Solar Cells, *Adv. Energy Mater.*, 2022, **12**, 2103567.

76 G. Li, Z. Su, L. Canil, D. Hughes, M. H. Aldamasy, J. Dagar, S. Trofimov, L. Wang, W. Zuo, J. J. Jerónimo-Rendon, M. M. Byranvand, C. Wang, R. Zhu, Z. Zhang, F. Yang, G. Nasti, B. Naydenov, W. C. Tsoi, Z. Li, X. Gao, Z. Wang, Y. Jia, E. Unger, M. Saliba, M. Li and A. Abate, Highly efficient p–i–n perovskite solar cells that endure temperature variations, *Science*, 2023, **379**, 399–403.

77 M. Abdi-Jalebi, Z. Andaji-Garmaroudi, S. Cacovich, C. Stavrakas, B. Philippe, J. M. Richter, M. Alsari, E. P. Booker, E. M. Hutter, A. J. Pearson, S. Lilliu, T. J. Savenije, H. Rensmo, G. Divitini, C. Ducati, R. H. Friend and S. D. Stranks, Maximizing and stabilizing luminescence from halide perovskites with potassium passivation, *Nature*, 2018, **555**, 497–501.

78 J. Cao, S. X. Tao, P. A. Bobbert, C.-P. Wong and N. Zhao, Interstitial Occupancy by Extrinsic Alkali Cations in Perovskites and Its Impact on Ion Migration, *Adv. Mater.*, 2018, **30**, 1707350.

79 M. Saliba, T. Matsui, J.-Y. Seo, K. Domanski, J.-P. Correa-Baena, M. K. Nazeeruddin, S. M. Zakeeruddin, W. Tress, A. Abate, A. Hagfeldt and M. Grätzel, Cesium-containing triple cation perovskite solar cells: improved stability, reproducibility and high efficiency, *Energy Environ. Sci.*, 2016, **9**, 1989–1997.

80 Y. Yu, C. Wang, C. R. Grice, N. Shrestha, D. Zhao, W. Liao, L. Guan, R. A. Awni, W. Meng, A. J. Cimaroli, K. Zhu, R. J. Ellingson and Y. Yan, Synergistic Effects of Lead Thiocyanate Additive and Solvent Annealing on the Performance of Wide-Bandgap Perovskite Solar Cells, *ACS Energy Lett.*, 2017, **2**, 1177–1182.

81 F. H. Isikgor, F. Furlan, J. Liu, E. Ugur, M. K. Eswaran, A. S. Subbiah, E. Yengel, M. D. Bastiani, G. T. Harrison, S. Zhumagali, C. T. Howells, E. Aydin, M. Wang, N. Gasparini, T. G. Allen, A. ur Rehman, E. V. Kerschaver, D. Baran, I. McCulloch, T. D. Anthopoulos, U. Schwingenschlögl, F. Laquai and S. D. Wolf, Concurrent cationic and anionic perovskite defect passivation enables 27.4% perovskite/silicon tandems with suppression of halide segregation, *Joule*, 2021, **5**, 1566–1586.

82 G. Yang, Z. Ren, K. Liu, M. Qin, W. Deng, H. Zhang, H. Wang, J. Liang, F. Ye, Q. Liang, H. Yin, Y. Chen, Y. Zhuang, S. Li, B. Gao, J. Wang, T. Shi, X. Wang, X. Lu, H. Wu, J. Hou, D. Lei, S. K. So, Y. Yang, G. Fang and G. Li, Stable and low-photovoltage-loss perovskite solar cells by multifunctional passivation, *Nat. Photonics*, 2021, **15**, 681–689.

83 Z. Zeng, J. Zhang, X. Gan, H. Sun, M. Shang, D. Hou, C. Lu, R. Chen, Y. Zhu and L. Han, *In Situ* Grain Boundary Functionalization for Stable and Efficient Inorganic $CsPbI_2$ Br Perovskite Solar Cells, *Adv. Energy Mater.*, 2018, **8**, 1801050.

84 D. Kim, H. J. Jung, I. J. Park, B. W. Larson, S. P. Dunfield, C. Xiao, J. Kim, J. Tong, P. Boonmongkolras, S. G. Ji, F. Zhang, S. R. Pae, M. Kim, S. B. Kang, V. Dravid, J. J. Berry, J. Y. Kim, K. Zhu, D. H. Kim and B. Shin, Efficient, stable silicon tandem cells enabled by anion-

engineered wide-bandgap perovskites, *Science*, 2020, **368**, 155–160.

85 D. H. Kim, C. P. Muzzillo, J. Tong, A. F. Palmstrom, B. W. Larson, C. Choi, S. P. Harvey, S. Glynn, J. B. Whitaker, F. Zhang, Z. Li, H. Lu, M. F. A. M. van Hest, J. J. Berry, L. M. Mansfield, Y. Huang, Y. Yan and K. Zhu, Bimolecular Additives Improve Wide-Band-Gap Perovskites for Efficient Tandem Solar Cells with CIGS, *Joule*, 2019, **3**, 1734–1745.

86 H. Kim, J. S. Kim, J.-M. Heo, M. Pei, I.-H. Park, Z. Liu, H. J. Yun, M.-H. Park, S.-H. Jeong, Y.-H. Kim, J.-W. Park, E. Oveisi, S. Nagane, A. Sadhanala, L. Zhang, J. J. Kweon, S. K. Lee, H. Yang, H. M. Jang, R. H. Friend, K. P. Loh, M. K. Nazeeruddin, N.-G. Park and T.-W. Lee, Proton-transfer-induced 3D/2D hybrid perovskites suppress ion migration and reduce luminance overshoot, *Nat. Commun.*, 2020, **11**, 3378.

87 H. Kim, M. Pei, Y. Lee, A. A. Sutanto, S. Paek, V. I. E. Queloz, A. J. Huckaba, K. T. Cho, H. J. Yun, H. Yang and M. K. Nazeeruddin, Self-Crystallized Multifunctional 2D Perovskite for Efficient and Stable Perovskite Solar Cells, *Adv. Funct. Mater.*, 2020, **30**, 1910620.

88 Q. Jiang, J. Tong, R. A. Scheidt, X. Wang, A. E. Louks, Y. Xian, R. Tirawat, A. F. Palmstrom, M. P. Hautzinger, S. P. Harvey, S. Johnston, L. T. Schelhas, B. W. Larson, E. L. Warren, M. C. Beard, J. J. Berry, Y. Yan and K. Zhu, Compositional texture engineering for highly stable wide-bandgap perovskite solar cells, *Science*, 2022, **378**, 1295–1300.

89 E. M. Hutter, L. A. Muscarella, F. Wittmann, J. Versluis, L. McGovern, H. J. Bakker, Y.-W. Woo, Y.-K. Jung, A. Walsh and B. Ehrler, Thermodynamic Stabilization of Mixed-Halide Perovskites against Phase Segregation, *Cell Rep. Phys. Sci.*, 2020, **1**, 100120.

90 D. P. McMeekin, G. Sadoughi, W. Rehman, G. E. Eperon, M. Saliba, M. T. Hörantner, A. Haghighirad, N. Sakai, L. Korte, B. Rech, M. B. Johnston, L. M. Herz and H. J. Snaith, A mixed-cation lead mixed-halide perovskite absorber for tandem solar cells, *Science*, 2016, **351**, 151–155.

91 M. Monteiro Lunardi, A. Wing Yi Ho-Baillie, J. P. Alvarez-Gaitan, S. Moore and R. Corkish, A life cycle assessment of perovskite/silicon tandem solar cells: Perovskite/silicon tandem solar cell LCA, *Prog. Photovolt. Res. Appl.*, 2017, **25**, 679–695.

92 F. Kersten, P. Engelhart, H.-C. Ploigt, A. Stekolnikov, T. Lindner, F. Stenzel, M. Bartzsch, A. Szpeth, K. Petter, J. Heitmann and J. W. Müller, Degradation of multicrystalline silicon solar cells and modules after illumination at elevated temperature, *Sol. Energy Mater. Sol. Cells*, 2015, **142**, 83–86.

93 Y. Zhao, P. Miao, J. Elia, H. Hu, X. Wang, T. Heumueller, Y. Hou, G. J. Matt, A. Osvet, Y.-T. Chen, M. Tarragó, D. de Ligny, T. Przybilla, P. Denninger, J. Will, J. Zhang, X. Tang, N. Li, C. He, A. Pan, A. J. Meixner, E. Spiecker, D. Zhang and C. J. Brabec, Strain-activated light-induced halide segregation in mixed-halide perovskite solids, *Nat. Commun.*, 2020, **11**, 6328.

94 E. J. Juarez-Perez, L. K. Ono, I. Uriarte, E. J. Cocinero and Y. Qi, Degradation Mechanism and Relative Stability of Methylammonium Halide Based Perovskites Analyzed on the Basis of Acid–Base Theory, *ACS Appl. Mater. Interfaces*, 2019, **11**, 12586–12593.

95 B. Kammlander, S. Svanström, D. Kühn, F. O. L. Johansson, S. Sinha, H. Rensmo, A. G. Fernández and U. B. Cappel, Thermal degradation of lead halide perovskite surfaces, *Chem. Commun.*, 2022, **58**, 13523–13526.

96 A. Rajagopal, R. J. Stoddard, S. B. Jo, H. W. Hillhouse and A. K.-Y. Jen, Overcoming the Photovoltage Plateau in Large Bandgap Perovskite Photovoltaics, *Nano Lett.*, 2018, **18**, 3985–3993.

97 A. F. Palmstrom, G. E. Eperon, T. Leijtens, R. Prasanna, S. N. Habisreutinger, W. Nemeth, E. A. Gaulding, S. P. Dunfield, M. Reese, S. Nanayakkara, T. Moot, J. Werner, J. Liu, B. To, S. T. Christensen, M. D. McGehee, M. F. A. M. van Hest, J. M. Luther, J. J. Berry and D. T. Moore, Enabling Flexible All-Perovskite Tandem Solar Cells, *Joule*, 2019, **3**, 2193–2204.

98 J. Xu, C. C. Boyd, Z. J. Yu, A. F. Palmstrom, D. J. Witter, B. W. Larson, R. M. France, J. Werner, S. P. Harvey, E. J. Wolf, W. Weigand, S. Manzoor, M. F. A. M. Van Hest, J. J. Berry, J. M. Luther, Z. C. Holman and M. D. McGehee, Triple-halide wide–band gap perovskites with suppressed phase segregation for efficient tandems, *Science*, 2020, **367**, 1097–1104.

99 G. E. Eperon, G. M. Paternò, R. J. Sutton, A. Zampetti, A. A. Haghighirad, F. Cacialli and H. J. Snaith, Inorganic caesium lead iodide perovskite solar cells, *J. Mater. Chem. A*, 2015, **3**, 19688–19695.

100 Y. Wang, M. I. Dar, L. K. Ono, T. Zhang, M. Kan, Y. Li, L. Zhang, X. Wang, Y. Yang, X. Gao, Y. Qi, M. Grätzel and Y. Zhao, Thermodynamically stabilized β-$CsPbI_3$–based perovskite solar cells with efficiencies >18%, *Science*, 2019, **365**, 591–595.

101 B. Yu, J. Shi, S. Tan, Y. Cui, W. Zhao, H. Wu, Y. Luo, D. Li and Q. Meng, Efficient (>20%) and Stable All-Inorganic Cesium Lead Triiodide Solar Cell Enabled by Thiocyanate Molten Salts, *Angew. Chem., Int. Ed.*, 2021, **60**, 13436–13443.

102 S. Tan, B. Yu, Y. Cui, F. Meng, C. Huang, Y. Li, Z. Chen, H. Wu, J. Shi, Y. Luo, D. Li and Q. Meng, Temperature-Reliable Low-Dimensional Perovskites Passivated Black-Phase CsPbI3 toward Stable and Efficient Photovoltaics, *Angew. Chem., Int. Ed.*, 2022, **61**, e202201300.

103 S. M. Yoon, H. Min, J. B. Kim, G. Kim, K. S. Lee and S. I. Seok, Surface Engineering of Ambient-Air-Processed Cesium Lead Triiodide Layers for Efficient Solar Cells, *Joule*, 2021, **5**, 183–196.

104 S. Ishibashi, Y. Higuchi, Y. Ota and K. Nakamura, Low resistivity indium–tin oxide transparent conductive films. II. Effect of sputtering voltage on electrical property of films, *J. Vac. Sci. Technol., A*, 1990, **8**, 1403–1406.

105 C. Guillén and J. Herrero, Comparison study of ITO thin films deposited by sputtering at room temperature onto

polymer and glass substrates, *Thin Solid Films*, 2005, **480–481**, 129–132.

106 K. A. Bush, S. Manzoor, K. Frohna, Z. J. Yu, J. A. Raiford, A. F. Palmstrom, H.-P. Wang, R. Prasanna, S. F. Bent, Z. C. Holman and M. D. McGehee, Minimizing Current and Voltage Losses to Reach 25% Efficient Monolithic Two-Terminal Perovskite–Silicon Tandem Solar Cells, *ACS Energy Lett.*, 2018, **3**, 2173–2180.

107 Ö. Ş. Kabaklı, J. Kox, L. Tutsch, M. Heydarian, A. J. Bett, S. Lange, O. Fischer, C. Hagendorf, M. Bivour, M. Hermle, P. S. C. Schulze and J. C. Goldschmidt, Minimizing electro-optical losses of ITO layers for monolithic perovskite silicon tandem solar cells, *Sol. Energy Mater. Sol. Cells*, 2023, **254**, 112246.

108 L. Mazzarella, Y. Lin, S. Kirner, A. B. Morales-Vilches, L. Korte, S. Albrecht, E. Crossland, B. Stannowski, C. Case, H. J. Snaith and R. Schlatmann, Infrared Light Management Using a Nanocrystalline Silicon Oxide Interlayer in Monolithic Perovskite/Silicon Heterojunction Tandem Solar Cells with Efficiency above 25%, *Adv. Energy Mater.*, 2019, **9**, 1803241.

109 C. Blaga, G. Christmann, M. Boccard, C. Ballif, S. Nicolay and B. A. Kamino, Palliating the efficiency loss due to shunting in perovskite/silicon tandem solar cells through modifying the resistive properties of the recombination junction, *Sustainable Energy Fuels*, 2021, **5**, 2036–2045.

110 G. Yang, Z. J. Yu, M. Wang, Z. Shi, Z. Ni, H. Jiao, C. Fei, A. Wood, A. Alasfour, B. Chen, Z. C. Holman and J. Huang, Shunt mitigation toward efficient large-area perovskite-silicon tandem solar cells, *Cell Rep. Phys. Sci.*, 2023, **4**, 101628.

111 D. H. Wang, A. K. K. Kyaw, V. Gupta, G. C. Bazan and A. J. Heeger, Enhanced Efficiency Parameters of Solution-Processable Small-Molecule Solar Cells Depending on ITO Sheet Resistance, *Adv. Energy Mater.*, 2013, **3**, 1161–1165.

112 E. Aydin, E. Ugur, B. K. Yildirim, T. G. Allen, P. Dally, A. Razzaq, F. Cao, L. Xu, B. Vishal, A. Yazmaciyan, A. A. Said, S. Zhumagali, R. Azmi, M. Babics, A. Fell, C. Xiao and S. De Wolf, Enhanced optoelectronic coupling for perovskite/silicon tandem solar cells, *Nature*, 2023, **623**, 732–738.

113 Y.-Y. Xu, Y. Jiang, H.-Q. Du, X. Gao, Z.-Y. Qiang, C.-X. Wang, Z.-W. Tao, L.-H. Yang, R. Zhi, G.-J. Liang, H.-Y. Cai, M. U. Rothmann, Y.-B. Cheng and W. Li, Octahedral Tilt Enables Efficient and Stable Fully Vapor-Deposited Perovskite/Silicon Tandem Cells, *Adv. Funct. Mater.*, 2024, **34**, 2312037.

114 J. Werner, C.-H. Weng, A. Walter, L. Fesquet, J. P. Seif, S. De Wolf, B. Niesen and C. Ballif, Efficient Monolithic Perovskite/Silicon Tandem Solar Cell with Cell Area >1 cm^2, *J. Phys. Chem. Lett.*, 2016, **7**, 161–166.

115 J. Werner, A. Walter, E. Rucavado, S.-J. Moon, D. Sacchetto, M. Rienaecker, R. Peibst, R. Brendel, X. Niquille, S. De Wolf, P. Löper, M. Morales-Masis, S. Nicolay, B. Niesen and C. Ballif, Zinc tin oxide as high-temperature stable recombination layer for mesoscopic perovskite/silicon monolithic tandem solar cells, *Appl. Phys. Lett*, 2016, **109**, 233902.

116 K. A. Bush, A. F. Palmstrom, Z. J. Yu, M. Boccard, R. Cheacharoen, J. P. Mailoa, D. P. McMeekin, R. L. Z. Hoye, C. D. Bailie, T. Leijtens, I. M. Peters, M. C. Minichetti, N. Rolston, R. Prasanna, S. Sofia, D. Harwood, W. Ma, F. Moghadam, H. J. Snaith, T. Buonassisi, Z. C. Holman, S. F. Bent and M. D. McGehee, 23.6%-efficient monolithic perovskite/silicon tandem solar cells with improved stability, *Nat. Energy*, 2017, **2**, 17009.

117 R. L. Z. Hoye, K. A. Bush, F. Oviedo, S. E. Sofia, M. Thway, X. Li, Z. Liu, J. Jean, J. P. Mailoa, A. Osherov, F. Lin, A. F. Palmstrom, V. Bulović, M. D. McGehee, I. M. Peters and T. Buonassisi, Developing a Robust Recombination Contact to Realize Monolithic Perovskite Tandems With Industrially Common p-Type Silicon Solar Cells, *IEEE J. Photovolt.*, 2018, **8**, 1023–1028.

118 B. Chen, Z. Yu, K. Liu, X. Zheng, Y. Liu, J. Shi, D. Spronk, P. N. Rudd, Z. Holman and J. Huang, Grain Engineering for Perovskite/Silicon Monolithic Tandem Solar Cells with Efficiency of 25.4%, *Joule*, 2019, **3**, 177–190.

119 C. U. Kim, J. C. Yu, E. D. Jung, I. Y. Choi, W. Park, H. Lee, I. Kim, D.-K. Lee, K. K. Hong, M. H. Song and K. J. Choi, Optimization of device design for low cost and high efficiency planar monolithic perovskite/silicon tandem solar cells, *Nano Energy*, 2019, **60**, 213–221.

120 A. J. Bett, P. S. C. Schulze, K. M. Winkler, Ö. S. Kabakli, I. Ketterer, L. E. Mundt, S. K. Reichmuth, G. Siefer, L. Cojocaru, L. Tutsch, M. Bivour, M. Hermle, S. W. Glunz and J. C. Goldschmidt, Two-terminal Perovskite silicon tandem solar cells with a high-Bandgap Perovskite absorber enabling voltages over 1.8 V, *Prog. Photovolt. Res. Appl.*, 2020, **28**, 99–110.

121 C. O. Ramírez Quiroz, G. D. Spyropoulos, M. Salvador, L. M. Roch, M. Berlinghof, J. Darío Perea, K. Forberich, L. Dion-Bertrand, N. J. Schrenker, A. Classen, N. Gasparini, G. Chistiakova, M. Mews, L. Korte, B. Rech, N. Li, F. Hauke, E. Spiecker, T. Ameri, S. Albrecht, G. Abellán, S. León, T. Unruh, A. Hirsch, A. Aspuru-Guzik and C. J. Brabec, Interface Molecular Engineering for Laminated Monolithic Perovskite/Silicon Tandem Solar Cells with 80.4% Fill Factor, *Adv. Funct. Mater.*, 2019, **29**, 1901476.

122 A. Al-Ashouri, E. Köhnen, B. Li, A. Magomedov, H. Hempel, P. Caprioglio, J. A. Márquez, A. B. Morales Vilches, E. Kasparavicius, J. A. Smith, N. Phung, D. Menzel, M. Grischek, L. Kegelmann, D. Skroblin, C. Gollwitzer, T. Malinauskas, M. Jošt, G. Matič, B. Rech, R. Schlatmann, M. Topič, L. Korte, A. Abate, B. Stannowski, D. Neher, M. Stolterfoht, T. Unold, V. Getautis and S. Albrecht, Monolithic perovskite/silicon tandem solar cell with $>29\%$ efficiency by enhanced hole extraction, *Science*, 2020, **370**, 1300–1309.

123 P. S. C. Schulze, A. J. Bett, M. Bivour, P. Caprioglio, F. M. Gerspacher, Ö. Ş. Kabaklı, A. Richter, M. Stolterfoht, Q. Zhang, D. Neher, M. Hermle, H. Hillebrecht, S. W. Glunz

and J. C. Goldschmidt, 25.1% High-Efficiency Monolithic Perovskite Silicon Tandem Solar Cell with a High Bandgap Perovskite Absorber, *Sol. RRL*, 2020, **4**, 2000152.

124 L. Xu, J. Liu, F. Toniolo, M. De Bastiani, M. Babics, W. Yan, F. Xu, J. Kang, T. Allen, A. Razzaq, E. Aydin and S. De Wolf, Monolithic Perovskite/Silicon Tandem Photovoltaics with Minimized Cell-to-Module Losses by Refractive-Index Engineering, *ACS Energy Lett.*, 2022, **7**, 2370–2372.

125 J. Zheng, H. Wei, Z. Ying, X. Yang, J. Sheng, Z. Yang, Y. Zeng and J. Ye, Balancing Charge-Carrier Transport and Recombination for Perovskite/TOPCon Tandem Solar Cells with Double-Textured Structures, *Adv. Energy Mater.*, 2023, **13**, 2203006.

126 R. Mishima, M. Hino, M. Kanematsu, K. Kishimoto, H. Ishibashi, K. Konishi, S. Okamoto, T. Irie, T. Fujimoto, W. Yoshida, H. Uzu, D. Adachi and K. Yamamoto, 28.3% efficient perovskite-silicon tandem solar cells with mixed self-assembled monolayers, *Appl. Phys. Express*, 2022, **15**, 076503.

127 M. Babics, M. De Bastiani, A. H. Balawi, E. Ugur, E. Aydin, A. S. Subbiah, J. Liu, L. Xu, R. Azmi, T. G. Allen, A. U. Rehman, T. Altmann, M. F. Salvador and S. De Wolf, Unleashing the Full Power of Perovskite/Silicon Tandem Modules with Solar Trackers, *ACS Energy Lett.*, 2022, **7**, 1604–1610.

128 Y. Wu, P. Zheng, J. Peng, M. Xu, Y. Chen, S. Surve, T. Lu, A. D. Bui, N. Li, W. Liang, L. Duan, B. Li, H. Shen, T. Duong, J. Yang, X. Zhang, Y. Liu, H. Jin, Q. Chen, T. White, K. Catchpole, H. Zhou and K. Weber, 27.6% Perovskite/c-Si Tandem Solar Cells Using Industrial Fabricated TOPCon Device, *Adv. Energy Mater.*, 2022, **12**, 2200821.

129 X. Luo, H. Luo, H. Li, R. Xia, X. Zheng, Z. Huang, Z. Liu, H. Gao, X. Zhang, S. Li, Z. Feng, Y. Chen and H. Tan, Efficient Perovskite/Silicon Tandem Solar Cells on Industrially Compatible Textured Silicon, *Adv. Mater.*, 2023, **35**, 2207883.

130 Z. Ying, Z. Yang, J. Zheng, H. Wei, L. Chen, C. Xiao, J. Sun, C. Shou, G. Qin, J. Sheng, Y. Zeng, B. Yan, X. Yang and J. Ye, Monolithic perovskite/black-silicon tandems based on tunnel oxide passivated contacts, *Joule*, 2022, **6**, 2644–2661.

131 R. Pandey, S. Bhattarai, K. Sharma, J. Madan, A. K. Al-Mousoi, M. K. A. Mohammed and M. K. Hossain, Halide Composition Engineered a Non-Toxic Perovskite–Silicon Tandem Solar Cell with 30.7% Conversion Efficiency, *ACS Appl. Electron. Mater.*, 2023, **5**, 5303–5315.

132 N. Phung, D. Zhang, C. van Helvoirt, M. Verhage, M. Verheijen, V. Zardetto, F. Bens, C. H. L. Weijtens, L. J. (Bart) Geerligs, W. M. M. Kessels, B. Macco and M. Creatore, Atomic layer deposition of NiO applied in a monolithic perovskite/PERC tandem cell, *Sol. Energy Mater. Sol. Cells*, 2023, **261**, 112498.

133 S. Mariotti, E. Köhnen, F. Scheler, K. Sveinbjörnsson, L. Zimmermann, M. Piot, F. Yang, B. Li, J. Warby, A. Musiienko, D. Menzel, F. Lang, S. Keßler, I. Levine, D. Mantione, A. Al-Ashouri, M. S. Härtel, K. Xu, A. Cruz, J. Kurpiers, P. Wagner, H. Köbler, J. Li, A. Magomedov, D. Mecerreyes, E. Unger, A. Abate, M. Stolterfoht, B. Stannowski, R. Schlatmann, L. Korte and S. Albrecht, Interface engineering for high-performance, triple-halide perovskite–silicon tandem solar cells, *Science*, 2023, **381**, 63–69.

134 X. Wang, Z. Ying, J. Zheng, X. Li, Z. Zhang, C. Xiao, Y. Chen, M. Wu, Z. Yang, J. Sun, J.-R. Xu, J. Sheng, Y. Zeng, X. Yang, G. Xing and J. Ye, Long-chain anionic surfactants enabling stable perovskite/silicon tandems with greatly suppressed stress corrosion, *Nat. Commun.*, 2023, **14**, 2166.

135 T. Han, W. Zhu, T. Wang, M. Yang, Y. Zhou, H. Xi, P. Zhong, D. Chen, J. Zhang, C. Zhang and Y. Hao, MXene-Interconnected Two-Terminal, Mechanically-Stacked Perovskite/Silicon Tandem Solar Cell with High Efficiency, *Adv. Funct. Mater.*, 2024, **34**, 2311679.

136 X. Li, W. Zhang, X. Guo, C. Lu, J. Wei and J. Fang, Constructing heterojunctions by surface sulfidation for efficient inverted perovskite solar cells, *Science*, 2022, **375**, 434–437.

137 Y. Sun, L. Mao, T. Yang, H. Zhang, J. Shi, Q. Tan, F. Li, P. Zeng, J. Gong, Z. Liu and M. Liu, Ionic Liquid Modified Polymer Intermediate Layer for Improved Charge Extraction toward Efficient and Stable Perovskite/Silicon Tandem Solar Cells, *Small*, 2024, **20**, 2308553.

138 Z. Liu, H. Li, Z. Chu, R. Xia, J. Wen, Y. Mo, H. Zhu, H. Luo, X. Zheng, Z. Huang, X. Luo, B. Wang, X. Zhang, G. Yang, Z. Feng, Y. Chen, W. Kong, J. Gao and H. Tan, Reducing Perovskite/C60 Interface Losses *via* Sequential Interface Engineering for Efficient Perovskite/Silicon Tandem Solar Cell, *Adv. Mater.*, 2024, **36**, 2308370.

139 L. Qiao, T. Ye, T. Wang, W. Kong, R. Sun, L. Zhang, P. Wang, Z. Ge, Y. Peng, X. Zhang, M. Xu, X. Yan, J. Yang, X. Zhang, F. Zeng, L. Han and X. Yang, Freezing Halide Segregation Under Intense Light for Photostable Perovskite/Silicon Tandem Solar Cells, *Adv. Energy Mater.*, 2024, **14**, 2302983.

140 X. Ji, Y. Ding, L. Bi, X. Yang, J. Wang, X. Wang, Y. Liu, Y. Yan, X. Zhu, J. Huang, L. Yang, Q. Fu, A. K.-Y. Jen and L. Lu, Multifunctional Buffer Layer Engineering for Efficient and Stable Wide-Bandgap Perovskite and Perovskite/Silicon Tandem Solar Cells, *Angew. Chem., Int. Ed.*, 2024, **63**, e202407766.

141 C. Wang, S. Wang, W. Shi, Z. Su, K. Gao, F. Cao, D. Xu, X. Lou, X. Wang, K. Li, W. Li, X. Chen, H. Li, W. Li, A. Tong, Y. Xiao, J. Liu, X. Zhang, J. Yang and X. Yang, Solvent-Assisted Surface Modification Using Metallocene-Based Molecules for High-Efficiency Perovskite/Silicon Tandem Solar Cells, *Adv. Energy Mater.*, 2024, **14**, 2401039.

142 D. Turkay, K. Artuk, X.-Y. Chin, D. A. Jacobs, S.-J. Moon, A. Walter, M. Mensi, G. Andreatta, N. Blondiaux, H. Lai, F. Fu, M. Boccard, Q. Jeangros, C. M. Wolff and C. Ballif, Synergetic substrate and additive engineering for over 30%-efficient perovskite-Si tandem solar cells, *Joule*, 2024, **8**, 1735–1753.

143 E. Ugur, A. A. Said, P. Dally, S. Zhang, C. E. Petoukhoff, D. Rosas-Villalva, S. Zhumagali, B. K. Yildirim, A. Razzaq, S. Sarwade, A. Yazmaciyan, D. Baran, F. Laquai, C. Deger, I. Yavuz, T. G. Allen, E. Aydin and S. De Wolf, Enhanced cation interaction in perovskites for efficient tandem solar cells with silicon, *Science*, 2024, **385**, 533–538.

144 Y. Chen, N. Yang, G. Zheng, F. Pei, W. Zhou, Y. Zhang, L. Li, Z. Huang, G. Liu, R. Yin, H. Zhou, C. Zhu, T. Song, C. Hu, D. Zheng, Y. Bai, Y. Duan, Y. Ye, Y. Wu and Q. Chen, Nuclei engineering for even halide distribution in stable perovskite/silicon tandem solar cells, *Science*, 2024, **385**, 554–560.

145 J. Liu, Y. He, L. Ding, H. Zhang, Q. Li, L. Jia, J. Yu, T. W. Lau, M. Li, Y. Qin, X. Gu, F. Zhang, Q. Li, Y. Yang, S. Zhao, X. Wu, J. Liu, T. Liu, Y. Gao, Y. Wang, X. Dong, H. Chen, P. Li, T. Zhou, M. Yang, X. Ru, F. Peng, S. Yin, M. Qu, D. Zhao, Z. Zhao, M. Li, P. Guo, H. Yan, C. Xiao, P. Xiao, J. Yin, X. Zhang, Z. Li, B. He and X. Xu, Perovskite/silicon tandem solar cells with bilayer interface passivation, *Nature*, 2024, 1–8.

146 Z. Zhang, Y. Feng, J. Ding, Q. Ma, H. Zhang, J. Zhang, M. Li, T. Geng, W. Gao, Y. Wang, B. Zhang, T. Pauporté, J.-X. Tang, H. Chen, J. Chen and C. Chen, Rationally designed universal passivator for high-performance single-junction and tandem perovskite solar cells, *Nat. Commun.*, 2025, **16**, 753.

147 C. Guo, H.-Q. Du, Y.-C. Wang, X. Gao, Y.-Q. Lan, Y.-S. Xiao, W. Jiang, Y.-C. Zhou, Q.-B. Yuan, Z.-Y. Qiang, J.-H. Zheng, L.-H. Yang, C.-X. Wang, N. Yang, R. Lin, G.-J. Liang, M. U. Rothmann, X. Ouyang, Y.-B. Cheng and W. Li, Bifacially Reinforced Self-Assembled Monolayer Interfaces for Minimized Recombination Loss and Enhanced Stability in Perovskite/Silicon Tandem Solar Cells, *Adv. Mater.*, 2025, **37**, 2504520.

148 Z. Wang, Z. Han, X. Chu, H. Zhou, S. Yu, Q. Zhang, Z. Xiong, Z. Qu, H. Tian, W. Wang, F. Wan, Y. Yuan, Y. Lin, Y. Yang, X. Zhang, Q. Jiang and J. You, Regulation of Wide Bandgap Perovskite by Rubidium Thiocyanate for Efficient Silicon/Perovskite Tandem Solar Cells, *Adv. Mater.*, 2024, **36**, 2407681.

149 C. Li, Y. Chen, Y. Li, Z. Zhang, J. Yang, Y. Wang, L. Gong, Z. Yuan, L. Liang, S. Liu, Y. Zhu, C. Lian, M. Haider, T. Guo, X. Xu, D. Li, E. Bi and P. Gao, Achieving 32% Efficiency in Perovskite/Silicon Tandem Solar Cells with Bidentate-Anchored Superwetting Self-Assembled Molecular Layers, *Angew. Chem., Int. Ed.*, 2025, **64**, e202502730.

150 A. S. Subbiah, S. Mannar, V. Hnapovskyi, A. R. Pininti, B. Vishal, L. V. T. Merino, O. Matiash, O. Karalis, H. Hempel, A. Prasetio, B. Yildirim, P. Dally, D. R. Villalva, M. Babics, L. Xu, A. Razzaq, R. Azmi, F. Xu, H. L. Bristow, E. Ugur, A. U. Rehman, H. Pasanen, E. Aydin, T. Allen, D. Baran, T. Unold, F. Laquai and S. D. Wolf, Efficient blade-coated perovskite/silicon tandems *via* interface engineering, *Joule*, 2025, **9**, 101767.

151 C. Li, Y. Li, Y. Chen, H. Zhang, S.-T. Zhang, Z. Zhang, F. Lin, L. Liang, L. Gong, H. Hao, J. Wang, S. Bao, Y. Yang, M. K. Nazeeruddin, D. Li and P. Gao, Enhancing Efficiency of Industrially-Compatible Monolithic Perovskite/Silicon Tandem Solar Cells with Dually-Mixed Self-Assembled Monolayers, *Adv. Funct. Mater.*, 2024, **34**, 2407805.

152 A. Farag, T. Feeney, I. M. Hossain, F. Schackmar, P. Fassl, K. Küster, R. Bäuerle, M. A. Ruiz-Preciado, M. Hentschel, D. B. Ritzer, A. Diercks, Y. Li, B. A. Nejand, F. Laufer, R. Singh, U. Starke and U. W. Paetzold, Evaporated Self-Assembled Monolayer Hole Transport Layers: Lossless Interfaces in p–i–n Perovskite Solar Cells, *Adv. Energy Mater.*, 2023, **13**, 2203982.

153 Y. Luo, Y. Tian, K. Zhao, W. Mao, C. Liu, J. Shen, Z. Cheng, C. Değer, X. Miao, Z. Zhang, X. Sun, L. Yao, X. Zhang, P. Shi, D. Jin, J. Deng, M. Tian, I. Yavuz, N. Dong, R. Liu, R. Wang, D. Yang and J. Xue, Inductive effects in molecular contacts enable wide-bandgap perovskite cells for efficient perovskite/TOPCon tandems, *Nat. Commun.*, 2025, **16**, 4516.

154 L. Jia, S. Xia, J. Li, Y. Qin, B. Pei, L. Ding, J. Yin, T. Du, Z. Fang, Y. Yin, J. Liu, Y. Yang, F. Zhang, X. Wu, Q. Li, S. Zhao, H. Zhang, Q. Li, Q. Jia, C. Liu, X. Gu, B. Liu, X. Dong, J. Liu, T. Liu, Y. Gao, M. Yang, S. Yin, X. Ru, H. Chen, B. Yang, Z. Zheng, W. Zhou, M. Dou, S. Wang, S. Gao, L. Chen, M. Qu, J. Lu, L. Fang, Y. Wang, H. Deng, J. Yu, X. Zhang, M. Li, X. Lang, C. Xiao, Q. Hu, C. Xue, L. Ning, Y. He, Z. Li, X. Xu and B. He, Efficient perovskite/silicon tandem with asymmetric self-assembly molecule, *Nature*, 2025, **644**, 912–919.

155 J. Zhang, N. Kong, S. Uzun, A. Levitt, S. Seyedin, P. A. Lynch, S. Qin, M. Han, W. Yang, J. Liu, X. Wang, Y. Gogotsi and J. M. Razal, Scalable Manufacturing of Free-Standing, Strong Ti_3C_2T MXene Films with Outstanding Conductivity, *Adv. Mater.*, 2020, **32**, 2001093.

156 L. Yan, Y. Li, B. Shi, Y. Li, Q. Xu, B. Zhang, Y. Chen, W. Han, N. Ren, Q. Huang, Y. Zhao and X. Zhang, Reducing electrical losses of textured monolithic perovskite/silicon tandem solar cells by tailoring nanocrystalline silicon tunneling recombination junction, *Sol. Energy Mater. Sol. Cells*, 2022, **245**, 111868.

157 J. P. Mailoa, C. D. Bailie, E. C. Johlin, E. T. Hoke, A. J. Akey, W. H. Nguyen, M. D. McGehee and T. Buonassisi, A 2-terminal perovskite/silicon multijunction solar cell enabled by a silicon tunnel junction, *Appl. Phys. Lett*, 2015, **106**, 121105.

158 H. Shen, S. T. Omelchenko, D. A. Jacobs, S. Yalamanchili, Y. Wan, D. Yan, P. Phang, T. Duong, Y. Wu, Y. Yin, C. Samundsett, J. Peng, N. Wu, T. P. White, G. G. Andersson, N. S. Lewis and K. R. Catchpole, *In situ* recombination junction between p-Si and TiO_2 enables high-efficiency monolithic perovskite/Si tandem cells, *Sci. Adv.*, 2018, **4**, eaau9711.

159 K. Daoudi, B. Canut, M. G. Blanchin, C. S. Sandu, V. S. Teodorescu and J. A. Roger, Tin-doped indium oxide thin films deposited by sol–gel dip-coating technique, *Mater. Sci. Eng. C*, 2002, **21**, 313–317.

160 T. Maruyama and K. Fukui, Indium tin oxide thin films prepared by chemical vapour deposition, *Thin Solid Films*, 1991, **203**, 297–302.

161 H. R. Fallah, M. Ghasemi, A. Hassanzadeh and H. Steki, The effect of annealing on structural, electrical and optical properties of nanostructured ITO films prepared by e-beam evaporation, *Mater. Res. Bull.*, 2007, **42**, 487–496.

162 N. Manavizadeh, F. A. Boroumand, E. Asl-Soleimani, F. Raissi, S. Bagherzadeh, A. Khodayari and M. A. Rasouli, Influence of substrates on the structural and morphological properties of RF sputtered ITO thin films for photovoltaic application, *Thin Solid Films*, 2009, **517**, 2324–2327.

163 Y. Hoshi and R. Ohki, Low energy rf sputtering system for the deposition of ITO thin ®LMS, *Electrochimica Acta*, 1999, **44**(21–22), 3927–3932.

164 M. Stowell, J. Müller, M. Ruske, M. Lutz and T. Linz, RF-superimposed DC and pulsed DC sputtering for deposition of transparent conductive oxides, *Thin Solid Films*, 2007, **515**, 7654–7657.

165 E. Aydin, C. Altinkaya, Y. Smirnov, M. A. Yaqin, K. P. S. Zanoni, A. Paliwal, Y. Firdaus, T. G. Allen, T. D. Anthopoulos, H. J. Bolink, M. Morales-Masis and S. De Wolf, Sputtered transparent electrodes for optoelectronic devices: Induced damage and mitigation strategies, *Matter*, 2021, **4**, 3549–3584.

166 H. Kanda, A. Uzum, A. K. Baranwal, T. A. N. Peiris, T. Umeyama, H. Imahori, H. Segawa, T. Miyasaka and S. Ito, Analysis of Sputtering Damage on I–V Curves for Perovskite Solar Cells and Simulation with Reversed Diode Model, *J. Phys. Chem. C*, 2016, **120**, 28441–28447.

167 K. Liu, B. Chen, Z. J. Yu, Y. Wu, Z. Huang, X. Jia, C. Li, D. Spronk, Z. Wang, Z. Wang, S. Qu, Z. C. Holman and J. Huang, Reducing sputter induced stress and damage for efficient perovskite/silicon tandem solar cells, *J. Mater. Chem. A*, 2022, **10**, 1343–1349.

168 D. Hamaguchi, S. Kobayashi, T. Uchida, Y. Sawada, H. Lei and Y. Hoshi, Improvement in luminance efficiency of organic light emitting diodes by suppression of secondary electron bombardment of substrate during sputter deposition of top electrode films, *Jpn. J. Appl. Phys.*, 2016, **55**, 106501.

169 E. Yang, X. Yang, D. Hao, H. Deng, J. Yu, Y. Tian and L. Jiang, High-performance meso–macroporous SiO_2 anti-reflective coatings with enhanced optical and mechanical stability for solar energy applications, *J. Mater. Chem. C*, 2025, **13**, 9736–9746.

170 T. Wahl, J. Hanisch, S. Meier, M. Schultes and E. Ahlswede, Sputtered indium zinc oxide rear electrodes for inverted semitransparent perovskite solar cells without using a protective buffer layer, *Org. Electron.*, 2018, **54**, 48–53.

171 S. Yoon, H. U. Ha, H. Seok, H. Kim and D. Kang, Highly Efficient and Reliable Semitransparent Perovskite Solar Cells *via* Top Electrode Engineering, *Adv. Funct. Mater.*, 2022, **32**, 2111760.

172 X. Dai, S. Chen, Y. Deng, A. Wood, G. Yang, C. Fei and J. Huang, Pathways to High Efficiency Perovskite Monolithic Solar Modules, *PRX Energy*, 2022, **1**, 013004.

173 H. B. Lee, W.-Y. Jin, M. M. Ovhal, N. Kumar and J.-W. Kang, Flexible transparent conducting electrodes based on metal meshes for organic optoelectronic device applications: a review, *J. Mater. Chem. C*, 2019, **7**, 1087–1110.

174 J. Liu, M. De Bastiani, E. Aydin, G. T. Harrison, Y. Gao, R. R. Pradhan, M. K. Eswaran, M. Mandal, W. Yan, A. Seitkhan, M. Babics, A. S. Subbiah, E. Ugur, F. Xu, L. Xu, M. Wang, A. ur Rehman, A. Razzaq, J. Kang, R. Azmi, A. A. Said, F. H. Isikgor, T. G. Allen, D. Andrienko, U. Schwingenschlögl, F. Laquai and S. De Wolf, Efficient and stable perovskite-silicon tandem solar cells through contact displacement by MgF_x, *Science*, 2022, **377**, 302–306.

175 S. Li, Z. Shi, Z. Tang and X. Li, Comparison of ITO, In_2O_3:Zn and In_2O_3:H transparent conductive oxides as front electrodes for silicon heterojunction solar cell applications, *Vacuum*, 2017, **145**, 262–267.

176 T. H. Park, W. Ren, H. J. Lee, N. Kim, K. R. Son, A. Rani and T. G. Kim, Efficient TADF-based blue OLEDs with 100% stretchability using titanium particle-embedded indium zinc oxide mesh electrodes, *NPG Asia Mater.*, 2022, **14**, 66.

177 J. Jeong, S. J. Park, S. Park, D. Lim, J. Jang, H.-J. Jung, J. Y. Kim and H.-K. Kim, Soft sputtering of NIR-transparent InGaTiO top electrodes on semi-transparent perovskite solar cells for perovskite-Si tandem solar cells, *Nano Energy*, 2025, **143**, 111327.

178 K. M. McLoughlin, A. J. Oskouei, M. K. Sing, A. Bandegi, S. Mitchell, J. Kennedy, T. G. Gray and I. Manas-Zloczower, Thermomechanical Properties of Cross-Linked EVA: A Holistic Approach, *ACS Appl. Polym. Mater.*, 2023, **5**, 1430–1439.

179 Z. Fu, M. Xu, Y. Sheng, Z. Yan, J. Meng, C. Tong, D. Li, Z. Wan, Y. Ming, A. Mei, Y. Hu, Y. Rong and H. Han, Encapsulation of Printable Mesoscopic Perovskite Solar Cells Enables High Temperature and Long-Term Outdoor Stability, *Adv. Funct. Mater.*, 2019, **29**, 1809129.

180 E. Klampaftis and B. S. Richards, Improvement in multicrystalline silicon solar cell efficiency *via* addition of luminescent material to EVA encapsulation layer, *Prog. Photovoltaics*, 2024, 345–351.

181 R. Cheacharoen, C. C. Boyd, G. F. Burkhard, T. Leijtens, J. A. Raiford, K. A. Bush, S. F. Bent and M. D. McGehee, Encapsulating perovskite solar cells to withstand damp heat and thermal cycling, *Sustainable Energy Fuels*, 2018, **2**, 2398–2406.

182 R. Cheacharoen, N. Rolston, D. Harwood, K. A. Bush, R. H. Dauskardt and M. D. McGehee, Design and understanding of encapsulated perovskite solar cells to withstand temperature cycling, *Energy Environ. Sci.*, 2018, **11**, 144–150.

183 B. Guo, R. Lai, S. Jiang, L. Zhou, Z. Ren, Y. Lian, P. Li, X. Cao, S. Xing, Y. Wang, W. Li, C. Zou, M. Chen, Z. Hong, C. Li, B. Zhao and D. Di, Ultrastable near-infrared perovskite light-emitting diodes, *Nat. Photonics*, 2022, **16**, 637–643.

184 G. A. Soares, I. S. Bicalho, S. Castro-Hermosa, L. de, Q. Corrêa, B. H. S. Miranda, A. dos, S. Marques, S. L. Fernandes, T. Cunha, V. V. de Freitas, R. de, Q. Vilaça,

L. Wouk and D. Bagnis, A comparative study of acrylic and epoxy-based adhesives for perovskite solar cells encapsulation, *Sol. Energy*, 2024, **273**, 112496.

185 M. De Bastiani, M. Babics, E. Aydin, A. S. Subbiah, L. Xu and S. De Wolf, All Set for Efficient and Reliable Perovskite/Silicon Tandem Photovoltaic Modules?, *Sol. RRL*, 2022, **6**, 2100493.

186 Y. Wang, I. Ahmad, T. Leung, J. Lin, W. Chen, F. Liu, A. M. C. Ng, Y. Zhang and A. B. Djurišić, Encapsulation and Stability Testing of Perovskite Solar Cells for Real Life Applications, *ACS Mater. Au*, 2022, **2**, 215–236.

187 Q. Emery, M. Remec, G. Paramasivam, S. Janke, J. Dagar, C. Ulbrich, R. Schlatmann, B. Stannowski, E. Unger and M. Khenkin, Encapsulation and Outdoor Testing of Perovskite Solar Cells: Comparing Industrially Relevant Process with a Simplified Lab Procedure, *ACS Appl. Mater. Interfaces*, 2022, **14**, 5159–5167.

188 Q. Emery, L. Dagault, M. Khenkin, N. Kyranaki, W. M. B. De Araújo, U. Erdil, M. Demuylder, S. Cros, R. Schlatmann, B. Stannowski and C. Ulbrich, Tips and Tricks for a Good Encapsulation for Perovskite-Based Solar Cells, *Prog. Photovolt. Res. Appl.*, 2025, **33**, 551–559.

189 P. Mariani, M. Á. Molina-García, J. Barichello, M. I. Zappia, E. Magliano, L. A. Castriotta, L. Gabatel, S. B. Thorat, A. E. Del Rio Castillo, F. Drago, E. Leonardi, S. Pescetelli, L. Vesce, F. Di Giacomo, F. Matteocci, A. Agresti, N. De Giorgi, S. Bellani, A. Di Carlo and F. Bonaccorso, Low-temperature strain-free encapsulation for perovskite solar cells and modules passing multifaceted accelerated ageing tests, *Nat. Commun.*, 2024, **15**, 4552.

190 M. D. Kempe, Modeling of rates of moisture ingress into photovoltaic modules, *Sol. Energy Mater. Sol. Cells*, 2006, **90**, 2720–2738.

191 Y. Peng, Y. Weng, G. Chen, D. Hong, W. Wang, C. Chen, X. Zhou, Y. Zhang, C. Wu, T. Guo and Q. Yan, Improved mechanical properties of Al_2O_3/acrylic laminates for flexible thin film encapsulation by introducing wavy interfaces, *Org. Electron.*, 2023, **117**, 106791.

192 L. Fumagalli, M. Binda, I. S. Lopez, D. Natali, M. Sampietro, S. Ferrari, L. Lamagna and M. Fanciulli, Multi layer structure for encapsulation of organic transistors, *Org. Electron.*, 2009, **10**, 692–695.

193 X. Xiao, M. Wang, S. Chen, Y. Zhang, H. Gu, Y. Deng, G. Yang, C. Fei, B. Chen, Y. Lin, M. D. Dickey and J. Huang, Lead-adsorbing ionogel-based encapsulation for impact-resistant, stable, and lead-safe perovskite modules, *Sci. Adv.*, 2021, **7**, eabi8249.

194 D. A. Jacobs, M. Langenhorst, F. Sahli, B. S. Richards, T. P. White, C. Ballif, K. R. Catchpole and U. W. Paetzold, Light Management: A Key Concept in High-Efficiency Perovskite/Silicon Tandem Photovoltaics, *J. Phys. Chem. Lett.*, 2019, **10**, 3159–3170.

195 E. Aydin, T. G. Allen, M. De Bastiani, L. Xu, J. Ávila, M. Salvador, E. Van Kerschaver and S. De Wolf, Interplay between temperature and bandgap energies on the outdoor performance of perovskite/silicon tandem solar cells, *Nat. Energy*, 2020, **5**, 851–859.

196 B. A. Kamino, B. Paviet-Salomon, S.-J. Moon, N. Badel, J. Levrat, G. Christmann, A. Walter, A. Faes, L. Ding, J. J. Diaz Leon, A. Paracchino, M. Despeisse, C. Ballif and S. Nicolay, Low-Temperature Screen-Printed Metallization for the Scale-Up of Two-Terminal Perovskite–Silicon Tandems, *ACS Appl. Energy Mater.*, 2019, **2**, 3815–3821.

197 V. Nikitina, C. Reichel, D. Erath, S. Kirner, A. Richter, T. Rößler, A. De Rose, A. Kraft and H. Neuhaus, Shingling meets perovskite-silicon heterojunction tandem solar cells, *Sol. Energy Mater. Sol. Cells*, 2023, **263**, 112590.

198 M. Despeisse, C. Ballif, A. Faes and A. Lachowicz, Metallization and interconnection for silicon heterojunction solar cells and modules, *Photovolt. Int.*, 2015, 30.

199 C. Clement, H. Bell, F. Vogg, L. Rebenklau, P. Gierth and U. Partsch, Inert Drying System for Copper Paste Application in PV, *Energy Procedia*, 2013, **38**, 423–429.

200 D. Wood, I. Kuzma-Filipek, R. Russell, F. Duerinckx, N. Powell, A. Zambova, B. Chislea, P. Chevalier, C. Boulord, A. Beucher, N. Zeghers, W. Deng, Z. Feng, P. Verlinden, J. Szlufcik and G. Beaucarne, Passivated Busbars from Screen-printed Low-temperature Copper Paste, *Energy Procedia*, 2014, **55**, 724–732.

201 A. De Rose, D. Erath, V. Nikitina, J. Schube, D. Güldali, Ä. Minat, T. Rößler, A. Richter, S. Kirner, A. Kraft and A. Lorenz, Low-temperature metallization & interconnection for silicon heterojunction and perovskite silicon tandem solar cells, *Sol. Energy Mater. Sol. Cells*, 2023, **261**, 112515.

202 S. Svanström, T. J. Jacobsson, G. Boschloo, E. M. J. Johansson, H. Rensmo and U. B. Cappel, Degradation Mechanism of Silver Metal Deposited on Lead Halide Perovskites, *ACS Appl. Mater. Interfaces*, 2020, **12**, 7212–7221.

203 T. Hatt, P. S. C. Schulze, O. Er-Raji, A. Richter, R. Efinger, O. Schultz-Wittmann, M. Heydarian, L. Tutsch, J. C. Goldschmidt, M. Glatthaar, S. W. Glunz and J. Bartsch, Plated copper electrodes for two-terminal perovskite/silicon tandem solar cells, *Sol. Energy Mater. Sol. Cells*, 2022, **246**, 111912.

204 A. M. Jeffries, T. Nietzold, L. T. Schelhas and M. I. Bertoni, Corrosion of novel reactive silver ink and commercial silver-based metallizations in diluted acetic acid, *Sol. Energy Mater. Sol. Cells*, 2021, **223**, 110900.

205 F. Toniolo, H. Bristow, M. Babics, L. M. D. Loiola, J. Liu, A. A. Said, L. Xu, E. Aydin, T. G. Allen, M. Meneghetti, S. P. Nunes, M. De Bastiani and S. De Wolf, Efficient and reliable encapsulation for perovskite/silicon tandem solar modules, *Nanoscale*, 2023, **15**, 16984–16991.

206 E. A. Gaulding, A. E. Louks, M. Yang, R. Tirawat, M. J. Wilson, L. K. Shaw, T. J. Silverman, J. M. Luther, A. F. Palmstrom, J. J. Berry and M. O. Reese, Package Development for Reliability Testing of Perovskites, *ACS Energy Lett.*, 2022, **7**, 2641–2645.

207 Z. Song, C. L. McElvany, A. B. Phillips, I. Celik, P. W. Krantz, S. C. Watthage, G. K. Liyanage, D. Apul and M. J. Heben, A technoeconomic analysis of perovskite solar module manufacturing with low-cost materials and techniques, *Energy Environ. Sci.*, 2017, **10**, 1297–1305.

208 F. Fu, J. Li, T. C. Yang, H. Liang, A. Faes, Q. Jeangros, C. Ballif and Y. Hou, Monolithic Perovskite-Silicon Tandem Solar Cells: From the Lab to Fab ?, *Adv. Mater.*, 2022, **34**, 2106540.

209 K. Sveinbjörnsson, B. Li, S. Mariotti, E. Jarzembowski, L. Kegelmann, A. Wirtz, F. Frühauf, A. Weihrauch, R. Niemann, L. Korte, F. Fertig, J. W. Müller and S. Albrecht, Monolithic Perovskite/Silicon Tandem Solar Cell with 28.7% Efficiency Using Industrial Silicon Bottom Cells, *ACS Energy Lett.*, 2022, **7**, 2654–2656.

210 L. Mao, T. Yang, H. Zhang, J. Shi, Y. Hu, P. Zeng, F. Li, J. Gong, X. Fang, Y. Sun, X. Liu, J. Du, A. Han, L. Zhang, W. Liu, F. Meng, X. Cui, Z. Liu and M. Liu, Fully Textured, Production-Line Compatible Monolithic Perovskite/Silicon Tandem Solar Cells Approaching 29% Efficiency, *Adv. Mater.*, 2022, **34**, 2206193.

211 C. Manspeaker, G. Merrion, K. Krouse and A. Zakhidov, Ambient Processing Conditions and Their Effects on Perovskite Device Performance, *Cryst. Res. Technol.*, 2022, **57**, 2100116.

212 L. Contreras-Bernal, C. Aranda, M. Valles-Pelarda, T. T. Ngo, S. Ramos-Terrón, J. J. Gallardo, J. Navas, A. Guerrero, I. Mora-Seró, J. Idígoras and J. A. Anta, Homeopathic Perovskite Solar Cells: Effect of Humidity during Fabrication on the Performance and Stability of the Device, *J. Phys. Chem. C*, 2018, **122**, 5341–5348.

213 T. D. Siegler, A. Dawson, P. Lobaccaro, D. Ung, M. E. Beck, G. Nilsen and L. L. Tinker, The Path to Perovskite Commercialization: A Perspective from the United States Solar Energy Technologies Office, *ACS Energy Lett.*, 2022, **7**, 1728–1734.

214 L. Gil-Escrig, I. Susic, İ. Doğan, V. Zardetto, M. Najafi, D. Zhang, S. Veenstra, S. Sedani, B. Arikan, S. Yerci, H. J. Bolink and M. Sessolo, Efficient and Thermally Stable Wide Bandgap Perovskite Solar Cells by Dual-Source Vacuum Deposition, *Adv. Funct. Mater.*, 2023, 2214357.

215 H.-L. Chen, Y.-M. Lu and W.-S. Hwang, Characterization of sputtered NiO thin films, *Surf. Coat. Technol.*, 2005, **198**, 138–142.

216 M. Liu, M. B. Johnston and H. J. Snaith, Efficient planar heterojunction perovskite solar cells by vapour deposition, *Nature*, 2013, **501**, 395–398.

217 L. Gil-Escrig, M. Roß, J. Sutter, A. Al-Ashouri, C. Becker and S. Albrecht, Fully Vacuum-Processed Perovskite Solar Cells on Pyramidal Microtextures, *Sol. RRL*, 2021, **5**, 2000553.

218 S. E. Sofia, H. Wang, A. Bruno, J. L. Cruz-Campa, T. Buonassisi and I. M. Peters, Roadmap for cost-effective, commercially-viable perovskite silicon tandems for the current and future PV market, *Sustainable Energy Fuels*, 2020, **4**, 852–862.

219 L. McGovern, E. C. Garnett, S. Veenstra and B. Van Der Zwaan, A techno-economic perspective on rigid and flexible perovskite solar modules, *Sustainable Energy Fuels*, 2023, **7**, 5259–5270.

220 H. Li and W. Zhang, Perovskite Tandem Solar Cells: From Fundamentals to Commercial Deployment, *Chem. Rev.*, 2020, **120**, 9835–9950.

221 K. K. Shin Thant, C. Seriwattanachai, T. Jittham, N. Thamangraksat, P. Sakata and P. Kanjanaboos, Comprehensive Review on Slot-Die-Based Perovskite Photovoltaics: Mechanisms, Materials, Methods, and Marketability, *Adv. Energy Mater.*, 2025, **15**, 2570025.

222 X. Zheng, W. Kong, J. Wen, J. Hong, H. Luo, R. Xia, Z. Huang, X. Luo, Z. Liu, H. Li, H. Sun, Y. Wang, C. Liu, P. Wu, H. Gao, M. Li, A. D. Bui, Y. Mo, X. Zhang, G. Yang, Y. Chen, Z. Feng, H. T. Nguyen, R. Lin, L. Li, J. Gao and H. Tan, Solvent engineering for scalable fabrication of perovskite/silicon tandem solar cells in air, *Nat. Commun.*, 2024, **15**, 4907.

223 H. C. Weerasinghe, N. Macadam, J.-E. Kim, L. J. Sutherland, D. Angmo, L. W. T. Ng, A. D. Scully, F. Glenn, R. Chantler, N. L. Chang, M. Dehghanimadvar, L. Shi, A. W. Y. Ho-Baillie, R. Egan, A. S. R. Chesman, M. Gao, J. J. Jasieniak, T. Hasan and D. Vak, The first demonstration of entirely roll-to-roll fabricated perovskite solar cell modules under ambient room conditions, *Nat. Commun.*, 2024, **15**, 1656.

224 Y. Wang, I. Ahmad, T. Leung, J. Lin, W. Chen, F. Liu, A. M. C. Ng, Y. Zhang and A. B. Djurišić, Encapsulation and Stability Testing of Perovskite Solar Cells for Real Life Applications, *ACS Mater. Au*, 2022, **2**, 215–236.

225 X. Xiao, M. Wang, S. Chen, Y. Zhang, H. Gu, Y. Deng, G. Yang, C. Fei, B. Chen, Y. Lin, M. D. Dickey and J. Huang, Lead-adsorbing ionogel-based encapsulation for impact-resistant, stable, and lead-safe perovskite modules, *Sci. Adv.*, 2021, **7**, eabi8249.

226 F. Jafarzadeh, L. A. Castriotta, E. Calabrò, P. Spinelli, A. Generosi, B. Paci, D. Becerril Rodriguez, M. Luce, A. Cricenti, F. Di Giacomo, F. Matteocci, F. Brunetti and A. Di Carlo, Stable and sustainable perovskite solar modules by optimizing blade coating nickel oxide deposition over 15 × 15 cm^2 area, *Commun. Mater.*, 2024, **5**, 186.

227 L. Wagner, J. Suo, B. Yang, D. Bogachuk, E. Gervais, R. Pietzcker, A. Gassmann and J. C. Goldschmidt, The resource demands of multi-terawatt-scale perovskite tandem photovoltaics, *Joule*, 2024, **8**, 1142–1160.

228 N. Moody, S. Sesena, D. W. deQuilettes, B. D. Dou, R. Swartwout, J. T. Buchman, A. Johnson, U. Eze, R. Brenes, M. Johnston, C. L. Haynes, V. Bulović and M. G. Bawendi, Assessing the Regulatory Requirements of Lead-Based Perovskite Photovoltaics, *Joule*, 2020, **4**, 970–974.

229 C. E. Torrence, C. S. Libby, W. Nie and J. S. Stein, Environmental and health risks of perovskite solar modules: Case for better test standards and risk mitigation solutions, *iScience*, 2023, **26**, 105807.

230 P. Wu, J. H. Heo and F. Zhang, Lead chemisorption: Paving the last step for industrial perovskite solar cells, *Nano Res. Energy*, 2024, **3**, e9120093.